Study of the Crystallization Kinetics of Amorphous Magnetic Materials

A dissertation presented
by

Md. Masud Rana

to
The Department of Theoretical Physics
in partial fulfillment of the requirements
for the degree of
Doctor of Philosophy
in the subject of

Theoretical Physics

University of Dhaka
Shahbagh, Dhaka-1000
Bangladesh
July, 2018

Approval Sheet

This is to certify that a doctoral thesis entitled "Study of the Crystallization Kinetics of Amorphous Magnetic Materials" has been written by Md. Masud Rana who carried out the basic research under our supervision and guidance. He has successfully completed his research work and can now submit his thesis to the concerned authority for evaluation for his Ph.D. degree.

Dr. Golam Mohammed Bhuiyan

Professor
Department of Theoretical Physics
University of Dhaka
Dhaka-1000, Bangladesh

Dr. A. K. M. Abdul Hakim

Individual Consultant, Department of Glass and Ceramic Engineering
Visiting Professor, Department of Materials & Metallurgical Engineering
Bangladesh University of Engineering and Technology (BUET)
Dhaka-1000, Bangladesh
Former Chief Engineer and Director
Bangladesh Atomic Energy Commission, Dhaka

Dr. M. Arshad Momen

Professor
Department of Theoretical Physics
University of Dhaka
Dhaka-1000, Bangladesh

Dated, Dhaka
July, 2018

ISBN: 978-984-34-1536-3

Thesis supervisors **Author**

Dr. Golam Mohammed Bhuiyan Md. Masud Rana
Dr. A. K. M. Abdul Hakim
Dr. M. Arshad Momen

Study of the Crystallization Kinetics of Amorphous Magnetic Materials

Abstract

Amorphous state of materials is a metastable state, which transforms into more stable crystalline phase while subjected to appropriate thermal treatment. Nanocrystallization of amorphous metallic magnetic ribbons by annealing above their crystallization temperature renewed enormous scientific and technological interest as a materials of state-of-the-art applications. In this research work we have focused on the study of understanding the crystallization behavior and magnetic properties of such nanocrystalline alloys with respect to annealing parameters, grain size and the crystalline volume fraction.

Two series of amorphous ribbons of alloy compositions, (I) $Fe_{73.5-x}Cr_xNb_3Cu_1Si_{13.5}B_9$ (x = 1, 5, 10, 12.5 and 17.5) and (II) $Fe_{76.5-x}Nb_xCu_1Si_{13.5}B_9$ (x = 1, 2, 3, 4, 5, 6 and 7) are cast by melt spinning technique and annealed at different temperatures based on thermal analysis data to prepare samples of varying nanocrystalline states. The magnetic, electrical and structural properties are investigated by VSM, Impedance Analyzer, XRD, FESEM and Mössbauer Spectrometer. The crystallization behaviors of as cast amorphous samples are studied by DSC technique. The volume fractions of amorphous and crystalline phases have been confirmed by the Mössbauer Spectrometry. Result obtained from detailed study show that crystallization kinetics of both the series of prepared samples are dependent on contents of refractory metals Cr and Nb substitution. The role of both Cr and Nb is to inhibit the process of crystallization and hinder grain growth and shift the crystallization temperature towards the higher temperature imparting enhancement of thermal stability of the amorphous alloys against crystallization. This unique behavior facilitates controlled nanocrystallization of the amorphous samples by annealing that finally give novel magnetic properties. Experimentally it is verified that Nb is more powerful in controlling the crystallization kinetics then Cr. It has been observed that amorphous alloys with Cr = 1, 5 and Nb = 3, 4 are suitable alloy compositions for better soft magnetic properties while annealed at $T_a = 550^{o}$C and seems to be agree well with Herzer's Random Anisotropy Model (RAM).

Contents

Chapter 3: Preparation Methodology 34

Chapter 4: Experimental Techniques 54

List of Figures

List of Tables

List of Symbols

Activation energy	E
Annealing temperature	T_a
Angular frequency	ω
Anisotropy field	H_{k}
Anisotropy of the hard phase	K_{k}
Anisotropy of the soft phase	K_{m}
Average anisotropy	$<K>$
Boltzmann constant	k_B
Coercivity	H_C
Conductance	G
Critical exponent	b
Critical thickness of the hard phase	b_{ck}
Critical thickness of the soft phase	b_{cm}
Cross-sectional area of toroids	S
Curie temperature	T_{C}
Curie temperature of residual amorphous matrix	T_C^{am}
Crystallization temperature	T_{cry}
Diffraction angle	θ
Effective Stress	σ
Energy per unit area of a 180° Bloch wall	γ
Enthalpy of crystallization	$\Delta\mathrm{H}$
Equilibrium thickness of the Bloch wall	δ_{o}
Exchange-bias field	H_{ex}
Exchange correlation length	L_{e}
Exchange energy density	E_{A}
Exchange stiffness constant	A
Frequency	f
Full width at half maxima	FWHM
Giant magneto-impedance ratio	GMIR
Grain size	D_g
Heating rate	β
Imaginary part of initial permeability	μ''

Impedance	Z
Inductance	L
Initial permeability	μ_i
Inter planner spacing	d
Loss factor	$\tan\delta$
Magnetization	M
Magneto-impedance	MI
Magneto-impedance ratio	MIR
Maximum energy product	$(BH)_\mathrm{max}$
Melting temperature	T_m
Nucleation field	H_n
Number of turns	N
Packing fraction	p
Peak temperature	T_p
Quality factor	Q
Reactance	X
Real part of initial permeability	μ'
Recoil permeability	μ_r
Resistance	R
Resistivity	ρ
Remanent magnetization	Mr
Saturation magnetization	M_s
Saturation magnetostriction	λ_s
Saturation polarizatin	J_s
Skin depth	δ
Static magnetic field	H_dc
Susceptance	B
Thickness of the bloch wall	δ
Thickness of the hard phase	b_k
Thickness of the soft phase	b_m
Total flux	Φ
Magnetic permeability of free space	μ_o
Volume fraction of the soft phase	v_m
Volume fraction of the hard phase	v_k
Wavelength	λ

Acknowledgments

I would like to express my deepest gratitude to my supervisor Professor Dr. Golam Mohammed Bhuiyan and Co-Supervisors Dr. A. K. M. Abdul Hakim and Professor Dr. M. Arshad Momen, for their patience supervision and guidance. Their encouragement, assistance and guidance helped me such a great extent which make me possible to complete this research work successfully. I have no words in my dictionary to express the support of Prof. Bhuiyan and Dr. Hakim. I always found Prof. Bhuiyan available for me to address my any sort of problems either academic or personal. On the other hand Dr. Hakim gives unparalleled efforts towards the success of my research work. Without their support it was almost impossible for me to complete my degree.

I am grateful to Dr. Eng. Sheikh Manjura Hoque, CSO & Head, Materials Science Division and project director Capacity Build-up of Nano and Nano-Bio Technological Laboratory at Materials Science Division Atomic Energy Center, Dhaka (AECD) for allowing performing Mössbauer spectroscopy experiment and analyzing data. I acknowledge her continuous support to carry out my research in her lab.

My noteworthy gratefulness to my friend Dr. A .Z. Ziauddin Ahmed, splendid scholar, Adjunct Faculty, Department of Theoretical Physics, University of Dhaka for his didactic support and patience reading of the whole dissertation. His valuable discussion and critical analysis help me to improve my manuscript substantially.

I would like to express my sincere gratitude to Dr. Md. Abdul Gafur, PSO & Project Director, Development of Materials for Tools and Bio-Metallic Implant, BCSIR, Dhaka, for DSC measurement, Mr. Mehedi Hasan Rizvi, Assistant Prof., Department of Glass and Ceramic Engineering, BUET, for FESEM measurement, Mr. Sarowar Hossain, Ph. D. student, S. N. Bose National Centre for Basic Sciences, Kolkata, India, for magnetization measurement, and Md. Rabiul Hassan, Lecturer, NUBT, Khulna for his support to analyze the experimental data from the view of scientific basis.

My heartiest thanks to Dr. D. K. Saha and Dr. Shirin Akter, Ex-Director, AECD for their administrative supports to perform experiments in Materials Science Division's laboratories enable me to complete my work duly. Importantly, I would like to mention that the XRD experiment performed in laboratory of Materials Science Division, AECD, Dhaka. I also grateful to Dr. Mohammed Nazrul Islam Khan, PSO and, Samia Islam Liba, SSO, Materials Science Division, Atomic Energy Centre, Dhaka for offering me all possible support in AECD Lab.

I acknowledge Prof. Per Nordblad, Engineering Physics Department, Angstrom Laboratory and director, International Science Program (ISP), Uppsala University, Sweden, Prof. Nguyen Huy Dan, Institute of Material Sciencs (IMS), Vietnam Academy of Science and Technology (VAST) for his enormous assistance and kind support and valuable suggestions during the period of preparing my samples and also for obtaining experimental works in their laboratory.

I am lucky enough that I got the opportunity to collaborate with some senior Physicists home and abroad over the time of my Ph D study. For this connection I would like to thank Prof. Dr. R. I. M. Aminur Rashid, Ex-Vice Chancellor, Bangladesh Open University, Prof. Dr. Masbah Uddin Ahmed Ex-Vice Chancellor, Jagannath University Dhaka, Bangladesh and Head, Quality Assurance Unit, UGC, Prof. Dr. Azizur Rahman and Prof Dr. Obaidul Islam, Department of Physics, University of Dhaka, Prof. N. H. Nigh Department of Physics, Vietnam National University (VNU), Vietnam, and who encourage me to finish my research work duly.

I am grateful to my beloved teachers Prof. Rashidul Hasan, Prof. Fazle Elahi, and Prof. Kaisar Mobin for their blessings and encouragement towards the accomplishment of my research work.

I would like to offer my especial thanks to Prof. Abdus Salam Howlader, Principal, Mohammadpur Kendriya College, Dhaka, for giving me the permission and granting me leave with financial support to explore my PhD research at University of Dhaka as I am a faculty member of his College. Surely, this reflects his broad vision to enhance the quality of higher education in his institution.

My special thanks to my colleagues those who encouraged me to finish my research work timely.

I would also like to express my gratitude to Prof. Dr. S. S. Sikder, Prof. Dr. Shamsul Alam, Prof. Dr Md. Nazrul Islam, Prof. Dr. A. K. M. Fazlul Haque, Prof. Dr. Md. Sultan Mahmudand, Prof. Md. Kamrul Hossain, Associate Prof. Dr. Robiul Islam and Associate Prof. Dr. Saroaut Noor for their moral support and inspiration in my thesis works.

I would like to thank Associate Prof. Dr. Md. Riazuddin Molla, Dr. Hari Narayan Das, Mr. Dulal Hossain and Mr. Mohammad Alamgir Hossain, for their kind support and acute interest in my research.

I would like to thank Mrs. Anjuman Ara Begum, Mrs. Alhamara Parvin, Mrs. Nazmunnahar, Mr. Kamrul Hassan, Md. Anisur Rahaman and Mrs. Zarna Begum for their worm cooperation when I worked in the laboratory of Materials Science Division, AECD.

I would like to thank Mr. Mohammad Mohsin Ali, Mr. Safayatul Amin, Mr. Abdus Satter and Mr. Md. Sapon Mia for their help when I worked in the Theoretical Physics Department, University of Dhaka.

I am also thankful to Mr. Duong Dinh Thang, Mr. Do Tran Huu, Miss Nguyen Thi Mai and Mrs Nguyen Hai Yen for their Cordial co- operation and their smiling face to solve any of my problems for preparing ribbon sample at IMS, VAST, Vietnam.

I must express my gratitude to my beloved Father Md. Momin Uddin Mondol and Mother Mrs. Shamsun Nahar for their deep love and intense support to me and my research work. My sincere thanks also goes to my Father in Law Mohammad Abul Hossain and Mother in law Mrs. Azizun Nahar to inspire me in all respect. I would like to mention the name of my wife Mrs. Rounak Jahan Happy most importantly, whose constant and volatile inspiration and sacrifice enable me to complete this work duly. I possess an everlasting soft corner for my loving daughters, Taifa Momo Tanmana, Afsarah Momo Ahona and my only son Abrar Muiz Saad who has been deprived from my affection during the entire period of PhD research work.

I acknowledge the financial support of International Science Program (ISP), Uppsala University, Sweden for their magnificent sandwich PhD program under which present thesis work is accomplished and University Grant Commission (UGC), Dhaka, Bangladesh. I have prepared most of my samples from IMS, VAST, Hanoi, Vietnam under the financial support of ISP, Uppsala University, Sweden. I also acknowledge the S. N. Bose National Centre for Basic Sciences, Kolkata, India; Materials Science Division, Atomic Energy Centre Dhaka (AECD); PP&PDC Lab, BCSIR; Department of Glass and Ceramic Engineering, BUET, for allowing us to use their facility to characterize our samples.

Md. Masud Rana
July 2018

Dedicated
to
My Parents

Chapter -1

Introduction

1.1 General Introduction

Fe–Si–B alloys have been used for many years from the time when they display good soft magnetic properties. Exhaustive studies of the crystallization process, thermal properties and magnetic properties of these unique materials have been reported [1–6]. Most reports are paying attention on alloys with 5–10 at% Si and 73.5–76.5 at% Fe since this composition range used to display supreme technological implications. Soft magnetic material based on the Fine Materials (FINEMET) composition was the discovered in 1988. Thereafter enormous interest has been grown to study the Fe–Si–B alloy with more than 10 at% of Si content, along with the addition of other alloying elements [7–11]. In the Fe–Si–B amorphous alloy the composition determines the microstructure development during crystallization, the phase formation as well as the fixation of the thermal and magnetic properties. In the present work, an amorphous alloy was selected based on the composition of the FINEMET alloys with the addition of Cr and Nb as these elements influence the nucleation and growth processes. The compositions studied in the work are (I) $Fe_{73.5-x}Cr_xNb_3Cu_1Si_{13.5}B_9$ and (II) $Fe_{76.5-x}Nb_xCu_1Si_{13.5}B_9$. The current study focuses on the understanding of the crystallization processes of a number of FINEMET alloys which do contain Cu and varying Nb content and including Cr substituted for Fe. The thermal properties, phase transformation, microstructural evolution during crystallization and magnetic properties of the alloys have been examined.

The nanocrystalline structure of Fe(Si) based on FINEMET type soft magnetic alloys is created via the primary crystallization of *bcc*-Fe(Si) solid solution from the amorphous precursors according to the fundamental scheme characteristic to the hypo-eutectic glasses [8] $am_1 \rightarrow Fe(Si)_1 am_2$ (am_1 and am_2 are the initial amorphous precursor and the remainder amorphous phase, respectively). This reaction takes place within a few seconds as thermal effect. The outstanding soft magnetic properties do develop only progressively, in anticipation of the final volume fraction, concentration and distribution of the components between the nanograins and the intergranular amorphous shell isothermally heat treatment done around 500°C to 650°C. The addition of nucleating element Cu guarantees the development of uniform grain size and a sufficient partition between the two steps of crystallization. The nucleation procedure begins well under the temperature of the nanocrystalline grain formation [9]. The structural features and the soft magnetic properties of these alloys have been methodically explored in the "nanocrystalline state" [10, 11]. On the other hand, comparatively few data are obtainable from the early stage of nanocrystalline grain configuration, particularly as far as the low-temperature properties like saturation magnetization, M_s, or coercive force are concerned [12]. In this research the field dependence of M_s after structural relaxation, nucleation, and the premature period of crystallization will be contrasted with those in the fully nanocrystalline state.

The crystallization kinetics is very important for the growth of amorphous alloys and nanocrystalline materials, the characteristics of which are robustly affected by the crystallization development. So the crystallization kinetics of amorphous alloys have been studied comprehensively. Recently, a number of attempts have been made to look into the influence of substituting a variety of alloying elements in the $Fe_{73.5-x}Cr_xNb_3Cu_1Si_{13.5}B_9$ and $Fe_{76.5-x}Nb_xCu_1Si_{13.5}B_9$ composition (P for B [13], Ag for Cu [14], Au for Cu [15], Co for Fe [16], Cr for Fe [17,18]) on the crystallization process and magnetic properties. Generally, the crystallization kinetics of amorphous alloys have been studied by means of isothermal crystallization kinetics that can be investigated using the Johnson–Mehl–Avrami technique [19]. The study of the crystallization kinetics provides the activation energy, E, of crystallization and parameters like the Avrami exponent (n) accountable for the method of crystallization. Differential thermal analysis (DTA) has been employed for such a study under both non-isothermal and isothermal conditions. The data obtained from non-isothermal crystallization have been examined using well-established theoretical models, namely the Kissinger, Ozawa [20] and Augis–Bennett [21] models. These investigations help us to realize how metallic glasses crystallize.

The present research has been conducted to study the amorphous crystalline condition by changing the content of Cr and Nb inside the FINEMET materials which have been annealed at different temperatures to understand the variation in crystallization state as a function of temperature. The present status of growth of new materials and their understanding on a smaller and smaller length scale is at the origin of development in many areas of materials science. As the size decreases in the nanometer range, the materials display strange and interesting physical, chemical, mechanical, magnetic and electrical properties when those are evaluated to conventional coarse-grained counterparts [22, 23]. This is mostly accurate in the growth of new magnetic materials for a variety of significant technological applications [24, 25]. Nanomaterials are experiencing a fast expansion in recent years due to their state-of-the-art application in broad areas of technology like electronic, electrical and similar applications, also in catalysis, ceramics, magnetic data storage, structural components etc. To get together the technological demands in these areas, the size of the materials should be reduced to the nanometer scale. For example, the miniaturizations of electronic devices like transistor, diodes, inductors and sensors give efficient device functionalities [26]. Nonosciences and Technology is now a quite diversified field which covers the area from microelectronics to molecular biology [27]. The nanotechnology has its root dated back to the 1959 talk of Richard Feynman where he stated, “The principles of Physics, as far as I can see, do not speak against the possibility of maneuvering things atom by atom. It is not an attempt to violate any laws; it is something in principle, that can be done; but in practice it has not been done because we are too big”. The recent advances in materials synthesis, description techniques and methods of advance measurement facilities on the nanometer scale have significantly assisted the development of nanotechnology. Now scientists can think about the synthesis of materials maneuvering atom by atom. Nanomaterials can be classified into nanocrystalline materials and nanoparticles. Nanostructured materials are distinguished from conventional polycrystalline materials by the size of the crystallites that compose them. Defined broadly the term nanostructured is used to explain materials characterized by structural features in the range of ≈ 1-100 nm corresponding typically to ≈ $50\text{-}5\times10^7$ atoms respectively. Nanoparticles are interesting from the basic point of view due to their extremely small size. The increasing surface to volume ratio with decreasing size results in an increased implication of the grain boundaries (*i.e.* surface energies) especially in the “real” nanometer range (≤ 10 nm). Magnetic nanoparticles demonstrate a diversity of strange magnetic behaviors when compared with the bulk materials typically due to the surface or interface effects including symmetry breaking, electronic environment or charge transport and magnetic interactions. Nanocomposite or nanocrystalline magnetic materials have been developed in the course of suitable heat treatment of the initial amorphous precursors of the Fe-Si-B and Co-Si-B based alloys for the ultra-soft magnetic properties with amazingly high permeability and Fe-Nb-B and Fe-Nb-Cr based alloys for the spin exchange hard magnets with high energy product. Soft magnetic materials are used as transformers and sensors while the hard nanocomposite magnetic materials have already been envisaged in motors, actuators or generators etc. [28]. There are various methods of preparing nanoparticles and nanostructured materials which includes (a) plasma processing [29, 30] (b) deposition method [31, 32] and (c) fast quenching and subsequently crystallized to nanometric grains implanted in a still amorphous matrix [33].

In the present work we have used the third variant for the processing of nanocrystalline magnetic materials. In this method an amorphous precursor in the form of ribbons typically 20-30μm thick (metallic glass) is first obtained from the melt of the parent slab with suitable composition using a melt-spinning machine by rapid solidification method. Since amorphous state is metastable, upon controlled crystallization exceeding the crystallization temperature develops nanocrystalline grains dispersed in a residual amorphous matrix. Magnetic nanocomposites composed of nano-sized magnetic crystals of 10-15 nm embedded in an amorphous matrix [34]. Amorphous materials are illustrated by a lack of long-range atomic order, similar to that of liquid state [35]. The requirement of crystallinity causes amorphous materials to have a very low anisotropy based on random anisotropy model [36]. The lower anisotropy of the soft magnetic materials permits that ferromagnetic exchange length to turn out to be larger. In magnetic materials the ferromagnetic exchange length articulates the feature distance over which a magnetic atom manipulates its environment and the exchange energy starts to control over the anisotropy energy. This characteristic distance is of the order of 100 nm. Therefore if the magnetic materials have microstructure with grain diameters smaller than the ferromagnetic exchange length, it becomes promising to "average'' the anisotropy of the grains to a very low bulk value by random walk deliberation. Such a material then realizes the high saturation magnetization of the crystalline state, low coercivity and high permeability due to randomized anisotropy. In the case of nanocrystalline soft magnetic materials with trade name FINEMET obtained from the controlled crystallization from the amorphous precursor. It has been found that a significant averaging of the magnetocrystalline anisotropy over many grains with structural characteristic of 10-20 nm coupled in between an exchange length is the root cause of magnetic softening [34]. The ferromagnetic exchange length of this nanometric grain is typically ≈ 35 nm, which demonstrates the underlying significance of the length scale of the magnetic system.

1.2 Nanocrystalline Soft Magnetic Alloys: an Overview

In the year of 1988 Yoshizawa and co-researchers [36] report for the first time on a novel composition of iron-based alloys showing greater soft magnetic performance. The properties were a distinctive combination of the low losses, high permeability and close to zero magnetostriction as attained by permalloys. The peculiarity about the new material was the ultrafine microstructure with grain size of 10-20 nm, for which this material was named nanocrystalline, and from which the soft magnetic properties lastly derived [37, 38].

The alloy compositions of the present work are $Fe_{73.5-x}Cr_xNb_3Cu_1Si_{13.5}B_9$ and $Fe_{76.5-x}Nb_xCu_1Si_{13.5}B_9$ can be measured as a typical Fe-Si-B metallic glass composition with additions of Cr and Nb. These types of materials are well-defined as FINEMET. It is seen [39] that when it is subjected to most favorable heat treatment around 550K for 30 min, it experiences an evolution into nanocrystalline state. This state has been identified as two-phase structure in which ultrafine grains (10-20 nm) of the Fe-Si phase are embedded in an amorphous matrix fundamentally consisting of Fe, Nb and B. The Fe-Si grains have been initiated dispersed into the amorphous matrix [40]. The amount and the composition of Fe-Si grains depend critically on the annealing situation of the alloys. The nonsolubility of Cu and Fe observed to increase the nucleation rate of the Fe-Si crystallites. Usually Cu causes the decreases in crystallization temperature and the small amount of Nb retards the growth of the size of the nuclei [41]. The nanosized Fe-Si grains have been found to be ferromagnetically exchange coupled together through the Fe-Nb-B amorphous matrix. Since these grains are smaller than the ferromagnetic exchange length (35 nm), magnetocrystalline anisotropy of the nanocrystalline phase averages out to zero. Thus, FINEMET alloy displays high values of saturation magnetization, permeability, and very low values of coercivity and extremely low high-frequency losses. The above combination of the properties have been established as key issues for magnetic softening and revealed from large number of studies and reported on the present alloys [37, 42-45]. There are numerous reports available [40, 46, 47] on the high temperature magnetic performance of this alloy in the as-quenched form but only a few literature is found on low-temperature magnetic performance. Holzer *et al.* [12]

have studied the low-temperature magnetic properties, particularly the coercivity and magnetostriction and they have also anticipated the spin-wave stiffness constant of the FINEMET alloys.

In earlier of 1990 Suzuki *et al.* [48] accounted the advance of the $Fe_{88}Zr_7B_4Cu_1$ alloy, which was named NANOPERM^{TM}. Zr and B act as glass forming agents in this alloy and the microstructure consists of α-Fe grains embedded in an amorphous matrix. By removing Si, higher saturation induction is gained the FINEMET, but the H_c have been found to be higher. The amorphous intergranular phase in cooperation with FINEMET and NANOPERM has Curie temperatures inferior than that of the nanocrystalline grains.

In the year of 1998 Willard *et al*. [49] reported another family of nanocrystalline alloys named as HITPERM, an alloy based on the composition $Fe_{44}Co_{44}Zr_7B_4Cu_{1.}$ The key distinction of this material is the replacement of Co for Fe. HITPERM forms α-Fe-Co grains enhances amorphous matrix and has a Curie temperature superior than the primary crystallization temperature of the alloy. This allows the α-FeCo grains to remain exchange coupled at elevated operating temperatures. For the presence of Co, HITPERM alloy has an M_s higher than FINEMET or NANOPERM as well as a higher H_C.

1.3 Basic Phenomenon for Magneto-Softening of FINEMET Materials

Magnetic softness of materials depends on several parameters, such as magneto-anisotropy, magnetoelastic energy etc. In order to understand the activities of the magnetic properties for very small grain sizes, the arbitrary anisotropy model has been applied by Herzer [37, 38] for the nano-crystalline materials having grain size lesser than the domain wall width which has originally been proposed by Alben *et al.* [50] for the amorphous ferromagnets. Consider an assembly of exchange-coupled nanocrystals with arbitrarily oriented magnetocrystalline anisotropies and size appreciably lesser than the exchange length.

The effective anisotropy disturbing the magnetization procedure results from averaging over $N = (L_{\mathrm{ex}}/D)^3$ grains within the volume $V = L_{\mathrm{ex}}^3$ of the exchange length. For a fixed number, N, of grains all the time there will be some easiest direction indomitable by statistical variations. The resulting anisotropy density $<K>$ is analyzed by the mean fluctuation amplitude of the anisotropy energy of the N grains, which is further discussed in details in Chapter 2. The exchange contact is suppressing the magnetocrystalline anisotropy far more efficiently in the shorter length scale of the nanocrystalline composite than in the long length scales of crystal lattice. This may be imagined by taking long length scales in the nanocrystalline material and counting the average magneto-crystalline anisotropy in that length. Thus, average anisotropy is used in exchange length calculation.

From the definition of the average anisotropy and exchange length it is found that grain size is smaller than the exchange length L_e. As the coercivity can be taken as proportional to the effectual anisotropy, this investigation guides to Herzer's forecast that the efficient anisotropy and consequently the coercivity be supposed to grow as the sixth power of the grain size, $H_c \sim H_k \sim D^6$. For such a reduction in the coercivity to be understood, Herzer noted that the crystalline grains have to be exchanged coupled. To recapitulate, in purely amorphous structure, the local anisotropy concludes the exchange length. However, in a composite structure, it is the average anisotropy and not the local anisotropy that determines the exchange length. This follows from the fact that the moment difference is mostly due to the moment on nanocrystals and not due to the inverting amorphous matrix. The result is due to the development in scale of the exchange interactions in the composite structure compared to the purely amorphous structure. In order to preserve randomness of anisotropy it is essential to attain sufficient number of nanocrystals so that the inter-particle distance is less than the exchange length. The theoretical approximation of Herzer shows that a relatively small enlargement in grain size, D may cause a drastic rise in anisotropy $<K>$ by orders of magnitude, in agreement with experimental observations [51]. Other important factors for the tremendous soft magnetic properties of nano crystalline samples are their low saturation magnetostriction $\lambda_{s,}$ in order to reduce the megnetoelastic anisotropy energy. The low magnetostriction of nano structured materials can be understood from the equilibrium of the magnetostriction between the α-Fe(Si) crystallites with negative and amorphous matrix with positive value and usually given by $\lambda_s^{\mathrm{nano}}=V_{\mathrm{Fe(Si)}}\,\lambda_s^{\mathrm{Fe(Si)}}+(1-V_{\mathrm{Fe(Si)}})\,\lambda_s^{\mathrm{amor}}$, where $V_{\mathrm{Fe(Si)}}$ stands for the volume fraction of Fe(Si) crystallites. The higher permeability of the nanocrystalline samples in the first approximation can be expressed in terms of average magnetocrystalline anisotropy constant $<K>$ and magneto-elastic energy according to equation [52], $\mu_i = M_s^2/\sqrt{2\mu_0\left(<K>+3\lambda_s/2\right)}$, where, M_s is the saturation magnetization, μ_0 is the permeability of free space, σ is the effective stress and λ_s is the saturation magnetrstriction.

The analysis of the experimental data of Yoshizawa *et al.* [33] and Herzer [36] show $\lambda_s^{\mathrm{amor}} = 20\times10^{-6}$ (for as cast), $\lambda_s^{\mathrm{Fe(Si)}} = -6\times10^{-6}$ for conventional polycrystalline α-Fe(Si) and $\lambda_s^{\mathrm{nano}}= 2\times10^{-6}$ for nanocrystalline samples at 550°C.

Thus λ_s for annealed sample is about one order of magnitude lower. Moreover σ, the effective stress is substantially reduced if not completely eliminated by heat treatment.

In the present work the effect of partial substitution of Fe by Cr and Nb has been investigated. Partial substitution of Fe by Cr and Nb enhances the thermal stability against crystallization and lowers the Curie temperature of the amorphous phase. The aim of the present work is to study the influence of Cr and Nb substitution for Fe with an extended concentration range having nominal composition of $Fe_{73.5x}Cr_xCu_1Nb_3Si_{13.5}B_9$ where x = 1, 5, 10, 12.5 and 17.5 and $Fe_{76.5-x}NbxCu_1Si_13_{.5}B_9$ where x = 1, 2, 3, 4, 5, 6 and 7 amorphous alloys on the crystallization behavior, structural and magnetic properties as affected by thermal treatment. We have also perform Mössbauer spectroscopy experiment to analyze our samples in particular relative amount of amorphous and crystalline phase along with hyperfine field distribution, peak width and magnetic state of the sample. In Section 1.4 we have presented an overview of previously work in this area. The objectives of the present work are summarized briefly in Section 1.5.

1.4 Review of the Previous Works

1) In 2006, R. Zhang and R. V. Ramanujan studied the effect of Copper alloying additions on the crystallization of an amorphous Fe–Si–B alloy. They were found that Cu alloying additions reduced the crystallization temperature as well as the activation energy of the crystallization. Although the phases formed in both alloys were Fe_3Si and Fe_3B phases the microstructures were dramatically different: a dendritic microstructure was observed in the case of the Fe–Si–B alloy, while spheriodal crystals around 100 nm in size were observed in the case of the Fe–Si–B–Cu alloy [53].

2) New occurrence about surface morphological study has been studied by O.Životský, L. Klimša, A. Hendrych, Y. Jirásková and J. Buršík. They observed that yield formation of small α-FeSi nanocrystals of approximately (5 - 10) nm in dimension embedded in an amorphous matrix. Just such a surface microstructure causes asymmetric hysteresis loops measured by MOKE at different places at the ribbon surface [54].

3) Investigation of the effect of substituting Mn for Fe on the crystallization kinetics of amorphous $Fe_{73.5-x}Mn_xCu_1Nb_3Si_{13.5}B_9$ (x = 1, 3, 5 and 7) alloys had taken by *N*. Bayri and his team. The samples were annealed at 550^{o}C and 600 ^{o}C for 1 h under an argon atmosphere. The X-ray diffraction analyses showed only a crystalline peak belonging to the a-Fe(Si) phase, with the grain size ranging from 12.2 nm for x = 0 to 16.7 nm for x = 7. The activation energies of the alloys were calculated using Kissinger, Ozawa and Augis–Bennett models based on differential thermal analysis data [55].

4) K. Biswas studied that the crystallization kinetics of amorphous $Fe_{67}Co_{9.5}Nd_3Dy_{0.5}B_{20}$ was evaluated by differential scanning calorimetry in the mode of isochronal heating and isothermal annealing. In the case of isochronal heating, the crystallization peak temperature *Tp* shows a strong dependence on the heating rate. The activation energy for the crystallization (535 kJ.mol^{-1}) was determined by the Kissinger method. The isothermal transformation kinetics was modeled by the Johnson–Mehl–Avrami (JMA) equation. The Avrami exponents are in the range of 4.30–4.75 suggesting that the isothermal crystallization is governed by three-dimensional growth with an increasing nucleation rate [56].

5) C. Miguel, A. Zhukov, J.J. del Val, J. Gonza le studied that uniaxial magnetic anisotropy has been induced in amorphous $Fe_{73.5}Cu_1Nb_3Si_{15.5}B_7$ (Fe-rich) and $(Co_{77}Si_{13.5}B_{9.5})90$- Fe_7Nb_3 (Co-rich) ferromagnetic alloys by annealing under stress and/or magnetic field. Such anisotropy plays a crucial role on the magnetization process and, consequently, determines the future applications of these materials. The mechanisms involved on the origin of such induced magnetic anisotropy showed significant differences between Fe-rich and Co-rich amorphous alloys. This work provides a comparative study of the coercive field and induced magnetic anisotropy in Fe-rich and Co-rich (FINEMET) amorphous alloys treated by stress and/or field [57].

6) M. A. Hakim studied that the amorphous ribbons of composition $Fe_{77}Cu_{0.6}Nb_{2.4}$ $Si_{11}B_9$ have been annealed at three annealing temperatures of 500°C, 520°C and 530°C for 1 hour, which produces homogeneous, ultra-fine grain structure of about 11 nm on an average. The amorphosity of the ribbons has been confirmed by X-ray diffraction. Activation energy of crystallization of α-Fe(Si) and iron boride phase has been obtained as 2.02 eV and 3.66 eV respectively [58]

7) Khalid Hossain and other in 2015 has studied that coercivity and remanence have been found to decrease significantly for optimized annealed condition compared to as-cast state. The core loss of the samples decreases with the annealing time which indicates the good magnetic property of soft magnetic materials [59].

1.5 Objectives of Present work

1. Sythesize amorphous materials by rapid quenching method.
2. Make nanocrystalline ribbons from amorphous precursor by thermal treatment.
3. Understand the crystallization kinetics behavior by differencial scanning calorimetry (DSC).
4. Study the structaral parameters and by X-ray diffraction method (XRD).
5. Understand particle size and surface morphology by Field Emmission Electron Microscope (FESEM).
6. Transmision Electron Microscopy (TEM) for understand particle size and surface morphology.
7. Know the frequency dependent permeability, relative quality factor and loss tangent by impedance analyzer.
8. Study the magnetization at different field and different annealing temperature, the effect of temperature on magnetization by Vibration Sample Magnetometer (VSM).
9. Analyze hyperfine interaction by Mössbauer spectroscopy and estimate volume fraction of amorphous and nanocrystalline phases.

Organization of the present dissertation is as follows: In Chapter 1 we have presented a comprehensive introduction. Where, we have discussed all the necessary background, aims and objectives and also spot the important findings of the present work. Chapter 2 covers all the theories involved in our work. Sample preparation techniques and experimental procedures are discussed in the Chapter 3. Chapter 4 is enriched with the description of the equipment, theories involved with the experimental setups etc. All of ours results and findings are analyzed in detail in Chapter 5. Finally we have concluded the dissertation in Chapter 6.

Chapter 2

Theoretical Aspect

2.1 Herzer Model in Multi-Phase Systems

The indiscriminate anisotropy reproduction model was proposed by Herzer [37]. This predict the rapid fall in the intrinsic coercivity with decreasing average grain size. Polycrystalline Fe-based soft magnetic materials with average grain size. We usually focus on the grain size dependence on soft magnetic properties in polycrystalline magnetic materials for grain size 4 nm to several 100 nm. As that work, a large number of alterations have been made to the model to enhance explain the physical situation observed in nanocrystalline and amorphous soft magnetic nanocomposite ribbons. A multi-phase model has been used to explain for the attendance of both the nanocrystalline phase and the intergranular amorphous phase. Further, an effort was made to consist of the effects of long-range uniaxial anisotropies that arise as a result of internal strain or induced magnetic anisotropies. The most modern aspects of the random anisotropy model have been applied to soft magnetic nanocomposites and the history of its developments can be found in recent reviews [60, 61]. From Reference [60], the expression for the average anisotropy constant $\langle K \rangle$ in a 3-D multiphase coupled system with randomly oriented anisotropies at a scale smaller than magnetic correlation length L_{EX}:

$$\langle K \rangle = \sqrt{K_U^2 + \sum_i x_i \, \beta_i^2 K_{1,i}{}^2 \cdot \left(\frac{D_i}{L_{EX}} \right)^3} \tag{2.1}$$

In equation (2.1), $K_{1,i}$, x_i and D_i are the local anisotropy constant, volume fraction, grain size respectively. β_i, is a parameter conventionally used to define anisotropy constants for different symmetries, K_u denotes a uniaxial anisotropy which is uniform on a scale much larger then L_{EX}. When the coupling mechanism is dominated by exchange interaction, the correlation length L_{EX} is related to total average anisotropy constant $<K>$ self constantly as:

$$L_{EX} = \varphi \sqrt{\frac{A_{EFF}}{\langle K \rangle}} \tag{2.2}$$

In equation (2.2), φ is a pre-factor in the order of unity. A_{EFF} is the effective exchange stiffness constant, and $<K>$ is given by equation (2.1). These two equations must be solved self-consistently as the reduction in $<K>$ effectively increases the relevant exchange length as well. The solutions for the two extremes where the uniaxial large-scale induced anisotropy is very small or very large with respect to the exchange-averaged magneto crystalline anisotropy are:

$$\langle K \rangle = \langle K_{1,i} \rangle = \left(\sum_i x_i \sqrt{\beta_i \mid K_{1.i} \mid} \; . \left(\frac{D_i}{L_{o.i}} \right)^3 \right)^2, \text{ when } K_U = 0$$

$$\langle K \rangle \approx K_U + \frac{1}{2} \sum_i x_i \sqrt{\beta_i \mid K_{1.i} \mid K_U} \; . \left(\frac{D_i}{L_{0.i}} \right)^3 \text{ , if } K_U >> \langle K_{1.i} \rangle \tag{2.3}$$

and if the uniform anisotropy dominating over random contribution, *i.e.* $K_U >> <K_1>$ then

$$L_{0.i} = \varphi_{0.i} \sqrt{\frac{A_{EFF}}{K_{1.i}}} \text{ , with } \varphi_{0.i} = \frac{\varphi}{\sqrt{\beta_i}} \tag{2.4}$$

In the absence of long range anisotropies , the average anisotropy <*K*> is scaling with D^6 down to grain size of about 5nm below which the random anisotropy of the residual amorphous phase become significant relative to $<K_1>$. The random anisotropy model was originally proposed by Herzer [62]. In the case of the high field induced anisotropy alloys of interest in this work, equation (2.3) is likely the valid one showing that <*K*> is expected to be approximately proportional to K_U. Coercivity, H_C is typically assumed to be proportional to <*K*> in the Herzer model and so the large K_U alloys are expected to result in large <*K*> and large H_C's making them unlikely to be of interest for high permeability applications as discussed in the introduction. However, for the transverse field annealed alloys where rotational processes are dominant and the materials are magnetized along the hard axis, $H_C \sim <K>$ may not be a valid assumption. Therefore, it may be possible to obtain good soft magnetic properties and very low permeabilies in transverse field annealed high K_U alloys. The link between <*K*> and H_C for transverse field annealed cores is an area that deserves further investigation. This will become clear in the discussion of measured values of K_U and H_C for transverse field annealed "nanocomposites" in the fourth coming section.

2.2 Monatomic Directional Ordering in Crystalline Alloys

Atoms such as C and N occupy the octahedral interstitial sites in *bcc* Fe as shown in Figure 2.1. There are three different types of octahedral sites in this structure as labeled by "x", "y", and "z" according to the orientation of the pair of nearest neighbor atoms of the *bcc* lattice. The orientation of each pair of neighboring lattice sites results in a local axis of symmetry for each type of interstitial site analogous to the bond direction between pairs of molecules in directional pair ordering.

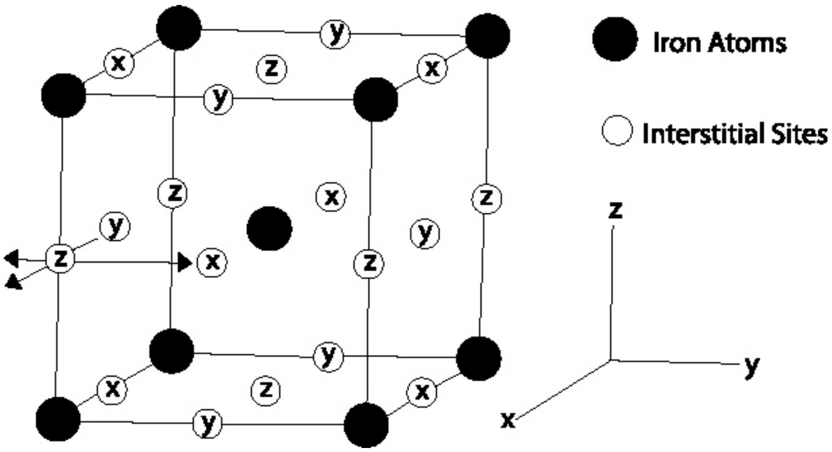

Figure 2.1: Octahedral interstitial sites in *bcc* Fe occupied by C and N atoms

(Reproduced from [63])

As a result, the dependence of the free energy on the orientation of the magnetization vector can be described in the same form as in equation (2.4). In this case, φ corresponds to the disorientation between the magnetization vector and the axis of symmetry of an occupied interstitial site. If a magnetic field is applied at temperatures sufficiently high for the interstitial atoms to jump between possible interstitial sites, there will be a tendency for interstitial atoms to preferentially occupy sites in which the axis of symmetry is more weakly or strongly disoriented with respect to the applied field depending on the sign of the relevant interaction parameter. If one calculates the estimated K_U in this model as discussed in [46] for a polycrystalline aggregate, the end result is presented in equation (2.5):

$$K_U \approx \frac{2X_B\omega^2\left[m\left(T_\mathrm{a}\right)\right]^2\left[m\left(T_\mathrm{Measurement}\right)\right]^2}{15k_BT_a} \tag{2.5}$$

In this case, X_B is the atomic fraction of the interstitial atoms and ω is the relevant interaction parameter for equation (2.5). Notice that K_U for this mechanism shows an identical dependence on T_a and $T_\mathrm{Measurement}$ as obtained for directional pair ordering theory but a different compositional dependence (K_U ~ X_B for monatomic as compared to K_U ~ $X_{A2}X_{B2}$ for directional pair ordering). Because of the identical temperature dependences of the monatomic directional ordering and directional pair ordering theories of field induced anisotropy, the combined effects of these two mechanisms can be expressed in the following form equation (2.5) if both are present simultaneously for a substitutional A-B binary alloy of composition X_B with interstitial incorporations of a ternary element C of composition X_C:

$$K_U \approx \frac{2X_B\omega^2\left[m\left(T_\mathrm{a}\right)\right]^2\left[m\left(T_\mathrm{Measurement}\right)\right]^2}{15k_BT_a} \tag{2.6}$$

The function $f(X_BX_C)$ is a linear combination of the compositional dependences due to both the directional pair ordering of A and B atoms and monatomic directional ordering of C atoms. For alloys in which the Curie temperature varies with composition, then the temperature dependent factors of equation (2.6) also depend upon composition as well. A modified form of equation (2.6) is employed in better understanding the effect of a variation in Curie temperature with composition on the measured compositional dependence of K_U for the Fe, Co-based “nanocomposites”.

2.3 Stability of Amorphous Nanocrystalline Materials

There are three kinds of stability of significance for amorphous magnetic alloys their resistance to the initiation of crystallization, structural relaxation effects and the relaxation or reorientation of directional order. Actually, controlled crystallization from the amorphous state seems to be the only method presently available to synthesize nanocrystalline alloys with attractive soft magnetic properties. The amorphous nanocrystalline ribbon is prepared by rapid solidification from the melt. This is the well established technique for large scale production of amorphous alloys. Amorphous alloys are in a metastable state and tend to transform into stable crystalline phases. At temperature below the crystallization temperature, structural relaxation effects take place and are caused by atomic rearrangements. The formation and resultant stability of amorphous alloys are important topic both for theoretical understanding and technical application. From the thermodynamic view point [64, 65], the ability of an alloy to be quenched into the glassy state is generally measured by the magnitude of ΔT_g :

$$\Delta T_g = T_m - T_g \tag{2.7}$$

where, T_m and T_g are the melting and glass transition temperatures respectively. In a similar manner the stability of the glass after formation is generally measured by the magnitude ΔTx :

$$\Delta T_x = T_x - T_g , \tag{2.8}$$

where, T_x is the temperature for the onset of crystallization. As the temperature decreases from T_m, the rate of crystallization will increase rapidly but then fall rapidly as the temperature decreases below T_g. Thus it one quenched a molten alloy rapidly enough to a temperature below T_g a quasi-equilibrium amorphous phase is obtained. There is no direct relation between the case of formation and the resultant stability of an amorphous alloy. The amorphous alloy composition most favorable for glass formation is near the eutectic, the deeper the eutectic the better is the glass formation ability [66]. At such a point the liquid is particularly stable against crystallization. There have been three approaches to relating the stability of the glass, *i.e*.

I. Bernal Model of randomly packed hard spheres [67], the metal atoms are assumed to from a random network of close packed hard spheres and the smaller metalloid atoms fill the holes inherent in such a structure. [68]

II. The effect of atomic size and inter atomic interactions, *i.e.* chemical bonding and suggested that it is chemical bonds which are the dominating factor in glass formation and stability [34].

III. The third approach is based on the role of the electron gas and showed that under certain circumstances a nearly free electron gas will produce a barrier against crystallization.

The crystallization is associated with nucleation and growth process. Since the formation of an amorphous alloy depends on the absence of long-range order, change of composition is expected to affect T_{g} and T_{x}. This is because the long range ordering of atoms depends on the free energy difference between the crystalline state and the amorphous state. The change of composition affects the growth kinetics in a complicated way, which can only be determined experimentally. The transition to the glassy state and the crystalline state is accompanied by an exothermic heat effect giving rise to a sharp peak in temperature dependence of the exothermic heat. Therefore, differential thermal analysis (DTA) is a widely used technique to study thermally induced transformations in amorphous alloys and to determine T_{g} and T_{x} . The magnitude of T_{g} and T_{x} are very different for amorphous materials and depend strongly on composition. The activation energy ranges typically between 2 and 6 eV. The difference of T_{g} on the heating rate $S = \frac{dT}{dt}$ can be used to determine the activation energy of crystallization [36]. Considering the fraction *x* of amorphous material transformed in to the crystalline state in time *t* and at temperature *T*, one obtains for the first order rate process.

$$\left(\frac{\delta x}{\delta t}\right)_T = K(1-x) \tag{2.9}$$

For thermally activated process, the rate constant *K* obeys an Arrhenius type of equations

$$K = K_o exp\left(\frac{-\Delta E}{RT}\right) \qquad (2.10)$$

where, K_o is a constant and ΔE is the activation energy. Combining equation (2.8) and equation (2.9) and using $dx = \left(\frac{\delta x}{\delta t}\right)_T dt + \left(\frac{\delta x}{\delta t}\right)_T dT$ with $\left(\frac{\delta x}{\delta t}\right)_T dT = 0$; one obtains

$$\left(\frac{\delta x}{\delta t}\right)_T = K_o(1-x)exp\left(\frac{-\Delta E}{RT}\right) \qquad (2.11)$$

At the peak of the exothermic heat, the change of the reaction rate $\frac{d^2x}{dt^2}$ is equal to zero, yielding with

$$T = T_x K_o(1-x)exp\left(\frac{-\Delta E}{RT_x}\right)\left(\frac{\Delta E}{RT_x}\right)s \qquad (2.12)$$

for the stability of amorphous alloy as given by equation [69] and is obtained from DTA . The values of ΔE also appear to correlate well with the number of atomic species in the alloy; the more complex the alloy the greater is ΔE. Similar correlation between thermal stability as measured by ΔT_x and ΔE appears too small. The incubation times are a common feature of phase transformations. They may be considered as the time required for a population of nuclei characteristic of the annealing temperature to be achieved. Arrhenius relation for the time for the onset of crystallization

$$T_x = T_o e^{\left(\frac{\Delta E_x}{RT}\right)} \qquad (2.13)$$

The incubation time therefore implies that no stable sized nuclei exist in the as-quenched ribbon. Equation (2.12) can be derived from transformation theory, where ΔE_x is the activation energy for viscous flow and other terms have been omitted because they have insignificant temperature dependence in this region of temperature. Correlations between thermal stability as measured by ΔT_x and ΔE_x were discussed experimentally and theoretically [70], but using the fine of transformation to the peak in the exothermic, rather than to the start of the exothermic, to obtain ΔE_x. The effect of this difference in measurement on ΔE_x appears to be small. Amorphous alloys are in a metastable state and tend to transform into stable crystalline phases. There are three kinds of stability of significance for amorphous magnetic ribbons:

i) Their resistance to the initiation of crystallization

ii) Structural relaxation effects and

iii) The relaxation or reorientation of directional order.

Amorphous alloys are in a metastable state and tend to transform into stable crystalline phases. The formation and resultant stability of amorphous alloys are important topic both for theoretical understanding and technical application.

2.4 Effect of Fine Particle Size

The understanding of the phenomenon of fine particle broadening is followed by the argument of Ślawska-Waniewska *et al*. [71]. We consider a finite crystal of thickness, $D_g = md$, where m is an integer, and *d* is the distance between crystalline planes, *i.e.*, there are *m* planes in D_g. Considering Figure 2.2, if the broadened Brag peak begins at an angle $2\theta_2$ and ends at $2\theta_1$, the breadth of the peak or full width at half maximum is given as:

$$\beta = \frac{1}{2}(2\theta_1 - 2\theta_2) = \theta_1 - \theta_2 \qquad (2.14)$$

Now consider the path differences for each of the two angles θ_1 and θ_2, for X-rays travelling the full thickness of the crystal. The width β is usually measured in radians, an intensity equal to half the maximum intensity. As a rough measure of β, we can take half the difference between the two extreme angles at which the intensity is zero, which amounts to assuming that the diffraction line triangular in shape.

We now write path difference equations for these two angles, related to the entire thickness of the crystal rather to the distance between adjacent planes.

$$2D_g \sin\theta_1 = (m+1)\lambda \tag{2.15}$$

$$2D_g \sin\theta_2 = (m-1)\lambda \tag{2.16}$$

By subtracting equation (2.15) and (2.16) we find,

$$D_g(\sin\theta_1 - \sin\theta_2) = \lambda$$

$$D_g.2\cos\left(\frac{\theta_1+\theta_2}{2}\right)\sin\left(\frac{\theta_1-\theta_2}{2}\right) = \lambda \tag{2.17}$$

But θ_1 and θ_2 both are nearly equal to θ, so that at $\theta_1+\theta_2 \approx 2\theta$ and $\sin\left(\frac{\theta_1-\theta_2}{2}\right) \approx \left(\frac{\theta_1-\theta_2}{2}\right)$

so that equation (2.17) can be written as:

$$2D_g \cos\theta.\left(\frac{\theta_1-\theta_2}{2}\right) = \lambda \tag{2.18}$$

By using equation (2.17) and equation (2.18) we obtain:

$$\beta.D_g \cos\theta = \lambda \tag{2.19}$$

$$D_g = \frac{\lambda}{\beta\cos\theta} \tag{2.20}$$

A more precise empirical action yields:

$$D_g = \frac{0.9\lambda}{\beta\cos\theta} \tag{2.21}$$

which is known as the Scherrer's formula. It is used to estimate the particle size of very small crystals from the measured width of their diffraction curves.

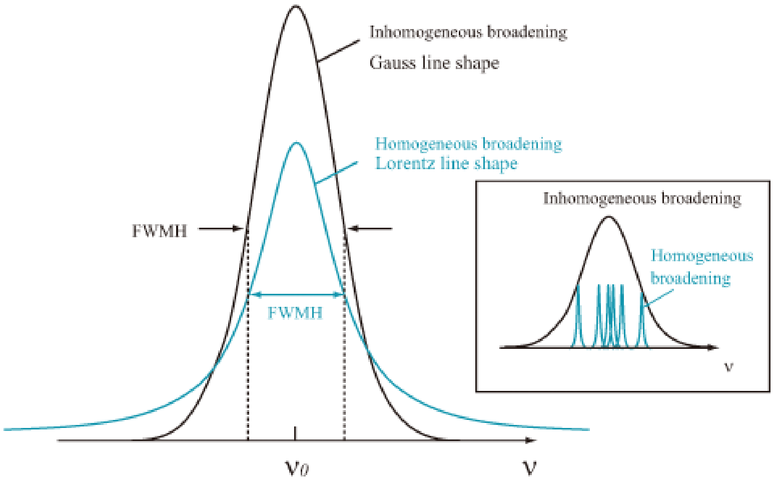

Figure 2.2: Schematic diagram of effect of fine particle size on diffraction curves.

2.5 Theory of X-ray Powder Method

A single crystal with a particular set of atomic planes oriented toward the X-ray beam will diffract X-ray at an angle θ determined by the Bragg equation.

$$2d \sin\theta = n\lambda \tag{2.22}$$

where λ is the wavelength of X-ray, d is distance between the planes. Most materials are not single crystals but are composed of billons of very small crystallite. This type of material is referred to as a powder or polycrystalline aggregate. In these materials, there are a great number of crystalline in all possible orientations. Thus, when a powder is placed in an X-ray beam all possible inter atomic planes will be seen by the beam but diffraction from each different type of plane will only occur at its characteristics diffraction angle θ. Thus, instead of a dot pattern, a powder pattern is a series of concentric rings. The powder diffraction patterns can be recorded on a strip of film surrounding the sample. The camera which carries out this diffraction pattern is called a Debye-Scherred camera. Today most patterns are obtained from powder diffractometer. Each peak in pattern shown in Figure 2.2 corresponds to diffraction from a particular set of interatomic planes, whose spacing d_{hkl} may be calculated from the Bragg equation. We use X-ray of known wave length and the value of θ can be measured directly on the diffraction pattern. Further, we can find the index (*hkl)* of each peak that means to define the interatomic plane corresponds to the peak. After index we can define the type of the structure of the crystallographic cell, calculate the crystallographic parameter. The calculation mentioned above depends on the symmetry of the crystal. For the cubic system, the index is following the XRD data consisting of θ_{hkl} and d_{hkl} values corresponding to the different crystallographic planes are used to determine the structural information of the samples. We determine the lattice spacing (interplanar distance), *d* using these reflections from Bragg's law (also see section 4.3.1) [72]. All values of sinθ involve in Bragg's law are calculated from the diffraction pattern and move the strip parallel to the abscissa until all the marks coincides with the value, $y = \sin\theta$ on the graphics. So we can define and the index *h*, *k*, *l* of every peak is found directly on the graphic.

2.6 Effect of Particle Size on Different Parameters

The smallness of the size of the crystallite will cause a broadening of the interference function which obviously means that the corresponding Laue-Bragg conditions will be modified as

$$a_1.s = h_i + u_i \tag{2.23}$$

where, h_i' s are integer and u_i' s are fraction less than unity . This signifies that the intensity will not be sharply concentrated at the corresponding Bragg angle θ. In terms of reciprocal lattice, there will be a speed of intensity around the reciprocal lattice point h_i corresponding to θ, and the spread which will be dependent on crystalline size is a measure of the smallness of the size provided there is no other defect in the sample under study. Let us now discuss one by one the effect and relationship of particle size with different line broadening parameters as defined earlier.

2.7 Permeability Measurement

2.7.1 Initial Permeability of Nanocrystalline Alloys

Low effective magnocrystalline anisotropy and low or vanishing magnetostriction are the key to superior soft magnetic properties. The nanocrystalline alloys offer the highest saturation induction, B_s and simultaneously, the highest level of permeability (μ_i). Typical commercial grades by now available under the trade name FINEMET [73] are offer a saturation induction of typically $B_s = 1.2 - 1.3\ T$ and initial permeability μ_i. Highest permeability is required for magnetic cores in ground fault interrupters or common mode chokes. The complex magnetic properties of initial permeability (μ_i) may be strongly affected by the presence of an electric current, particularly in ac condition. Moreover, the effects are rather different in as quenched amorphous nanocrystalline ribbons. The measurement of magnetic properties as a function of frequency and its analysis by means of the complex permeability formalism has recently led to the resolution of several aspects of magnetizations process [74-76]. The measurement of complex permeability gives as valuable information about the nature of the domain wall and their movements. Low losses, good high frequency behavior, favorable temperature dependence and high thermal stability of the soft magnetic properties are requirements fulfilled by the nanocrystalline alloy. In dynamic measurements the eddy current loss is very important, this occurs due to irreversible domain wall movements that are frequency dependent. The only draw-back of the nanocrystalline material seems to be the severe embrittlement upon crystallization which requires final shape annealing and restricts their application mainly to toroidally wound cores. The present goal of most of the recent nanocrystalline amorphous ribbons researches is to fulfill this requirement. Before going into the complexity of initial permeability measurement, we discuss in short the theories and mechanism involved in frequency spectrum of initial permeability and also affected by annealing.

2.7.2 Theories of Permeability

The primary requirement is the highest possible permeability, together with low losses in the frequency range of interest. The initial permeability μ_i is defined as the derivative of induction B with respect to the initial field H in the demagnetization state, *i.e.*

$$\mu_i = \frac{dB}{dH}, H \rightarrow 0,\ B \rightarrow 0 \tag{2.24}$$

At microwave frequency, and also in low an isotropic amorphous materials, dB and dH may be in different directions, the permeability this has a tensor character. In the case of amorphous materials containing a large number of randomly oriented magnetic atoms the permeability will be scalar. As we have,

$$B = \mu_o (H + M) \tag{2.25}$$

and susceptibility ,

$$\chi = \frac{dM}{dH} = \frac{d}{dH}\frac{1}{\mu_o}(B - H) = \frac{1}{\mu_o}(\mu - 1) \tag{2.26}$$

The magnetic energy density,

$$E = \frac{1}{\mu_0}\int H.dB \tag{2.27}$$

For time harmonic fields $H = H_0 \sin \omega t$, the dissipation can be described by a phase difference δ between *H* and *B*. In the case of permeability, it is defined as the proportionality constant between the magnetic field induction *B* and applied intensity *H*, *i.e.*

$$B = \mu H \tag{2.28}$$

This naive definition needs further sophistication. If a magnetic material is subjected to an ac magnetic field as we get,

$$B = B_0 e^{i\omega t} \tag{2.29}$$

Then it is observed that the magnetic flux density *B* experiences a delay. This is caused due to the presence of various losses and is thus expressed as,

$$B = B_0 e^{i(\omega t - \delta)} \tag{2.30}$$

where δ is the phase angle and marks the delay of *B* with respect to *H*, the permeability is then given by

$$\mu = \frac{B}{H} = \frac{B_0 e^{i(\omega t-\delta)}}{H_0 e^{i\omega t}} = \frac{B_0 e^{-i\delta}}{H_0} = \frac{B_0}{H_0}\cos\delta - i\frac{B_0}{H_0}\sin\delta \tag{2.31}$$

Therefore, $$\mu = \mu' - i\mu'' , \tag{2.32}$$

where

$$\mu' = \frac{B_0}{H_0}\cos\delta$$

$$\mu'' = \frac{B_0}{H_0}\sin\delta \tag{2.33}$$

The real part μ' of complex permeability μ as expressed in equation (2.33) represents the component of *B* which is in phase with *H*, so it corresponds to the normal permeability. If there are no losses, we should have $\mu = \mu'$. The imaginary part μ'' corresponds to that part of *B* which is delayed by a phase from *H*. The presence of such a component requires a supply of energy to maintain the alternating magnetization, regardless of the origin of delay. If is useful to introduce the loss factor or loss tangent (tanδ). The ratio of μ'' to μ', as is evident from equation gives,

$$\frac{\mu''}{\mu'} = \frac{\frac{B_0}{H_0}\sin\delta}{\frac{B_0}{H_0}\cos\delta} = \tan\delta \,. \tag{2.34}$$

This tanδ is called the loss factor . The *Q* – factor or quality factor is defined as the reciprocal of this loss factor *i.e.*

$$Q = \frac{1}{\tan\delta} \,. \tag{2.35}$$

And the relative quality factor $= \frac{\mu'}{\tan\delta}$. The behavior of μ' and μ'' versus frequency is called the permeability spectrum. The initial permeability of a ferromagnetic substance is the combined effect of the wall permeability and rotational permeability mechanisms.

2.7.3 High Frequency Behavior and Losses

The relative loss factor is given by the ratio of the absolute value of complex permeability, *μ* and its imaginary part, μ'', as, $\tan\delta = \frac{\mu''}{\mu'}$. The latter is directly related to the cycle losses at constant induction amplitude *B* by,

$$\frac{P}{f} = \frac{\pi B^2 \mu''}{\mu_0 \mu^2} \,. \tag{2.36}$$

The frequency dependence of permeability and the core losses of the nanocrystalline Fe-Cu-Nb-Si-B alloys are comparable to those of amorphous Co-based alloys and pass by the properties of conventional materials, even that of ferrites, over the whole frequency range up to several 100 KHz.

The favorable high frequency behavior is essentially related to (i) the thin ribbon gauge of $d \approx 20$ µm inherent to the production technique and (ii) to a relatively high electrical resistivity of typically $\rho \approx 115\mu\ \Omega$ - cm related to the high Si content in the bcc grains [77] and the intergranular amorphous phase. Both parameters are comparable to amorphous metals and yield low eddy current losses P_e, which in thin sheets at a frequency f and a induction level B are given per volume by [78]

$$P_e = \frac{3\sinh x - \sin x}{x\cosh x - \cos x}\frac{(\pi d f B)^2}{6\rho}$$

$$P_e \underset{x\langle\langle 1}{\approx} \frac{(\pi d f B)^2}{6\rho} \tag{2.37}$$

$$\text{with} \qquad x = 2\sqrt{\frac{f}{f_w}}$$

$$\text{where} \qquad f_w = \frac{4\rho}{\pi\mu_o\mu_i\ d^2} \tag{2.38}$$

is the limiting frequency above which the exciting magnetic field no longer fully penetrates the specimen and, accordingly, the permeability decreases as a function of the frequency.

2.8 Magnetization of the Amorphous Ribbons

The saturation magnetization of material at a temperature of 0K is one of its basic properties. Measurements are usually expressed as average moment per magnetic atom in units of Bohr magneton, μ_B or as specific saturation magnetization for the amorphous alloy, σ_s, in units of Am^2 / Kg. The moments of most amorphous alloys are lower than those of the crystalline transition metals, which they contain. However the direct effect of the structural disorder on the moments is very small. This points the importance of chemical instead of structural disorder. The reduction is least in B-based glass and highest in P-based glass. The observed moments on TM-M glasses can approximately fitted to a formula

$$\mu = \frac{\mu_{TM}C_{TM} - C_B - 2C_{si}3C_p}{C_{TM}} \tag{2.39}$$

where μ_{TM} is the magnetic moment of TM-M atoms, taken as 2.6, 1.6 and 0.6 respectively in Bohr magnetron for Fe, Co and Ni, C's are respective concentrations. This clearly demonstrates the charge transfer from metalloid to d-band of transition metal and seems to suggest that 1, 2 or 3 electrons are transferred from each of B, Si (C, Ge) or P atom. The relative number of electrons donated can be listed as $-P_{13}C_7 > -S_{15}B_{10} > -P_{16}B_6Al_3 > -P_{14}B_6 > -Si_9B_{13} > -B_{20}$ based on the relative magnitudes of M_s. Amorphous alloys are rather poor conductors but their 3*d*-electrons are just as "itinerant" as in the crystalline transition metal alloys. Only itinerant exchange between 3d moments is of importance in the metal-metalloid alloys. It itinerant exchange arises because single site exchange taken together with the inter site electron hopping terms produce a correlation between moments on different sites. This mechanism depends on the band structure and can lead to ferromagnetism, antiferromagnetism or complex spin arrangements. The theoretical treatment of spin ordering in amorphous solids is a much more difficult problem than the regular crystalline lattices and has not been satisfactorily solved. In first case, a unique constant exchange interaction between the magnetic atoms is assumed and the amorphous nature of the alloy is taken into account by calculating a random distribution of the local anisotropy field [75]. In the second approach to treating this problem a distribution of exchange integrals assumed in order to reflect the structural fluctuation in the amorphous alloy [76]. Both approaches predict that the *M vs T* curve will flat below that for the crystalline counterpart. The first model however predicts that amorphous alloys should exhibit a structure less Mössbauer spectrum, contrary to the observed spectra. Thus the second approach is preferred of the various theories the molecular approach (MFA) and mean field theories.

Chapter 3

Preparation Methodology

3. 1. Introduction

The metastable amorphous or glassy state of metals is characterized by the deficient of the ordered atomic arrangement of crystals resulting in the non-existence of defects such as grain boundaries or dislocations. Due to such structure, amorphous alloys show outstanding physico-chemical and mechanical properties. The start of metallic glasses has been one of the most exciting dealings in the annals of materials science and engineering [79].

In this Chapter, preliminary part incorporate the sections of historical expansion of bulk amorphous alloys, properties of bulk amorphous alloys and Zr-based bulk amorphous alloys, their manufacture processes and solidification techniques. The following sections will explain some approaches to establish theory of glass formation. These approaches are named as semi-empirical approaches, thermodynamic and kinetic approaches, atomistic approach, and pseudopotential theory. This chapter also provides the customs of calculations of some thermodynamic and structural formulas, required to decide the glass forming ability and used in calculations in following chapters.

Amorphous materials have been engaged for thousands of years, *e.g.* in the glass making industry. The research of metallic amorphous alloys was first accounted shortly subsequent to the Second World War (1946) when Brenner and Riddell developed on electrolytically placed amorphous Ni-P films. Since the initial synthesis of an amorphous phase in the Au-Si system by a fast solidification technique in 1960 [80], an enormous number of amorphous alloys have been formed for the last three decades. In the early 1960's, Duwez and his group (Klement, Willens and Duwez, 1960) began extensive research on metastable alloys prepared by quick solidification of liquid alloys [81]. First ferromagnetic amorphous alloys were accounted by Mader and Nowik (1965) and the smart soft magnetic properties were experiented soon after (Tsuei and Duwez, 1966). The technological prospective of these metastable materials then became appreciated in conjunction with more basic scientific interest in the alloys.

The investigation for other alloy compositions that could be produced as bulk amorphous alloys began and resulted a few years later in a series of new alloy compositions. From the time of 1988, it has been happened as expected in finding novel multi-component alloy schemes with much lower critical cooling rates in the Mg, Ln, Zr, Fe, Pd-Cu-, Pd-Fe-, Ti- and Ni-based alloy systems [81]. Bulk amorphous alloys and nanocrystalline materials have been synthesized in a number of ferrous and non-ferrous based alloy systems, which have gained some applications due to their unique physico-chemical and mechanical properties.

3.2 Background of Amorphous Alloys

3. 2.1 Bulk Metallic Amorphous Alloys

Bulk metallic amorphous alloys as well as bulk metallic glasses are currently a subject of numerous explorations because of their interest for both basic science and engineering applications [82]. They acquire a number of the individuality of usual oxide glasses in that they demonstrate random, non-crystalline arrangements of atoms, a glass change temperature, generally live up to the explanation of supercooled liquid. Bulk metallic amorphous alloys are mostly composed of metallic elements and the interatomic bonding between them is fundamentally metallic in nature. These features have allowed the manifestation of a variety of distinctiveness such as fine mechanical properties, functional physical properties and sole chemical properties, which have not been attained for typical crystalline alloys [79]. The dissimilarities between traditional metals, traditional (oxide) glasses, and metallic glasses are summarized in a simple and effective manner by the data in Table 3.1 [79].

Table 3.1: Relative comparison of the characteristics of traditional metals, traditional **g**lasses and metallic glasses.

Property	**Traditional metal**	**Traditional glass**	**Metallic glass**
Structure	Crystalline	Amorphous	Amorphous
Bonding	Metallic	Covalent	Metallic
Strength	Non-ideal	Almost ideal	Almost ideal
Workability	Good, ductile	Poor, brittle	Good, ductile
Hardness	Low to high	Very high	Very high
Corrosion resistance	Poor to good	Very good	Very good

in recent years, amorphous alloys are also paying attention for increasing concentration as a ancestor to create nanocrystalline alloys having an amorphous phase by partial crystallization for good mechanical properties, soft magnetism, hard magnetism, high magnetostriction in low applied fields, and high catalytic properties that have not been obtained for amorphous or crystalline single-phase alloys [83]. During the last 20 years, a large amount of attention has been dedicated to the expansion of bulk metallic glasses. The significant cooling rate for solidification of these alloys is less than 10^3°C-s^{-1}, and amorphous state yields with thicknesses of 1 mm and greater can be shaped by a usual casting process. Bulk metallic glass alloys have been prepared with Zr, Ti, Ni, Cu, and Mg based systems [84, 85], and more recently in Ca–Mg–Cu and Ca–Mg–Ag–Cu systems [86, 87]. Based on these investigation results, scientific and engineering importance of the amorphous and nanocrystalline alloys have increased significantly for the last three decades.

3. 2. 2 Fundamental Characteristics and Application Fields

Based on a large number of experimental data on the bulk amorphous alloys for the previous decades, it is confirmed that the bulk amorphous alloys exhibit various useful characteristics, and can be produced in the diameter range of 1 to 100 nm. These characteristics are much superior to those for the corresponding crystalline alloys and sufficient to be used as practical materials. The bulk amorphous alloys in Zr-Al-Ni-Cu, Zr-Ti-Al-Ni-Cu and Zr-Nb-Al-Ni-Cu systems have already been commercialized. The bulk amorphous alloys have useful important characteristics, therefore the application fields of the bulk amorphous alloys are seemed to be extended in the future. Table 3.2 summarizes the fundamental characteristics and application fields of bulk amorphous alloys [79].

Table 3.2: Fundamental characteristics and fields of applications of bulk metallic amorphous alloys [79].

Fundamental Characteristics	**Application Fields**
High strength	Machinery structural materials
High hardness	Optical precision materials
High impact fracture energy	Tool materials
High elastic energy	Electrode materials
High corrosion resistance	Corrosion resistant materials
High wear resistance	Hydrogen storage materials
High viscous flow ability	Ornament materials
Good soft magnetism	Writing appliance materials
High magnetostriction	Bonding materials
High frequency permeability	Sporting goods materials
High hydrogen storage	High magnetostrictive materials

3. 2. 3 Production Methods of Bulk Metallic Amorphous Alloys

Bulk metallic amorphous alloys can be produced by various methods. These methods can be summarized as follows:

1. **High-Pressure Die Casting Method:** By choosing the Mg-Ln-TM and Ln-Al-TM ternary alloys with the wide supercooled liquid region and the high glass forming ability, bulk amorphous alloys have been produced in a thickness range up to about 10 mm in cylindrical and sheet shapes by the high pressure die casting method [83].

2. **Copper Mold Casting Method:** Zr-based bulk amorphous alloys have been vitrified by ejection of the melt into copper molds [83].

3. **Arc Melting Method:** By choosing the quaternary or penternary alloys in Zr-Al-TM (TM = Co, Ni, Cu) system, bulk amorphous alloys can be produced by arc melting on a copper hearth. However, in this method, it is very difficult to suppress completely the precipitation of the Zr_2TM crystalline phase because of the ease of the heterogeneous nucleation by incomplete melting at the bottom side contacted with copper heart. It is to be mentioned that, an amorphous phase is formed in the inner region where the heat of flux reinforced from copper hearth disappears and the cooling capacity is reduced. That is, the low cooling rate obtained by arc melting is high enough to cause an amorphous phase in Zr-Al-Co-Ni-Cu system [83].

4. **Unidirectional Zone Melting Method:** A continuous bulk amorphous alloy is produced by this method using an arc-type heat source. This method is useful for the production of a continuous bulk amorphous alloy with a homogeneously mixed alloy composition, when an alloy with critical cooling rate, R_c much lower than about 10^4 $K.s^{-1}$ is used. The success of producing the bulk amorphous alloy by this method also implies the significant relaxation of the shape and dimension of amorphous alloys which have been limited to thin sheet, fine wire and small powder shapes [83]

5. **Suction Casting Method:** The suction casting method is used for the elimination of cavity and hole because of the solidification take place under a sucking.

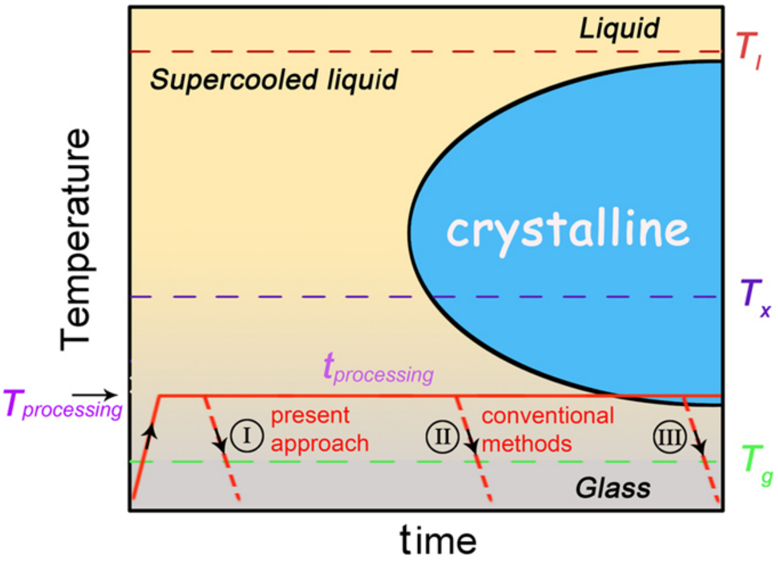

Figure 3.1: The aspect of the phase transition of bulk metallic amorphous alloys by continuous heating in association with that for conventional amorphous alloys which require high cooling rates above 10^4 K.s^{-1} for glass formation [83].

6. **Water Quenching Method:** The further multiplication of alloy components from ternary to quaternary and penternary systems causes a further decrease in R_c to 1 to 10 Ks^{-1} which are almost comparable to those for oxide glasses. The quaternary Pd-Cu-Ni-P and Zr-Al-Ni-Cu alloys have been amorphized into a bulk form with 72 mm (φ) × 75 mm and 16 mm (φ) × 150 mm, respectively, by quenching their molten alloys in a quartz tube into water [88].

3. 3 An Outline of Nanocrystalline Materials

Nnocrystalline amorphous ribbons can be considered as an off-shoot of amorphous materials. In fact nanocrystalline amorphous ribbons are composite material where nanocrystals are embedded in an amorphous matrix. Atomistic tailoring of nanocrystalline materials is one of the most active research areas in recent time. Main objective of such research is to design and fabricate new active and functional materials with precise predefined atomic arrangement and properties. There have been glimpses of exhibiting new properties like super plasticity, giant magnetoresistance (GMR), transparency in opaque ceramics, enhanced homogeneity, and abnormal soft ferromagnetic and giant magnetocaloric effects, possessed by those materials when reduced to nanometer dimensions. In addition to the understanding of the typical properties possessed by nanostructure materials, there are three other related areas which need serious attention:

1. Discovery and progress of appropriate preparation methods, especially those which are able to provide large industrial quantities of nanometer scale materials.

2. Improvement of processing methods for manufacturing these materials into useful size and shapes without losing their desirable nanometer size feature.

3. Detection of suitable characterization methods, where the nanometer size range of these materials falls just below or at the resolution limit of the conventional tools.

Nanocrystalline soft magnetic alloys have received significant attention due to their outstanding soft magnetic properties [88]. Small addition of Cu and Nb into Fe-Si-B amorphous materials changes considerably their crystallization behavior, which is executed under appropriately controlled conditions and the specific reason of these additions are:

1. The constituent Cu is used to support the formation of nuclei of ultrafine grains.
2. The constituent Nb is used to impede the growth of the crystallites.

In this material, the nanocrystalline state is composed of a fine structure of α-Fe(Si) and is habitually around 10 nm. For such an average grain size, the exchange interaction dominates the magnetic behavior of arbitrarily oriented crystallites guided by random anisotropy [89]. In the present research work twelve different nanocrystalline alloys are prepared by the substitution of Fe by Cr (x = 1, 5, 10, 12.5 and 17.5) and increasing Nb concentration (x = 1, 2, 3, 4, 5, 6 and 7) of the well accepted nanostructured $Fe_{73.5-x}Cr_xNb_3Cu_1Si_{13.5}B_9$ and $Fe_{76.5-x}Nb_xCu_1Si_{13.5}B_9$ FINEMET amorphous alloy systems.

3.4 Design of Nanocrystalline Alloy

Mater of alloy design include the issues of chemistry and processing designed to (i) optimize one of the important magnitude intrinsic and/or extrinsic magnetic properties as well as to (ii) optimize structural or microstructural features, which promote important magnetic properties. The first issue is concerned with the choice of chemistry so as to impact the intrinsic magnetization of the material. The second issue pertinent to further discussions here are alloy additions designed at aiding formation of an amorphous or bulk amorphous phase, as a means to an end or as a precursor for producing a nanocrystalline material [71].

Alloy design issues are in many ways influenced by the processing routes used to achieve desired microstructures. Figure 3.2 illustrates a flowchart for the considerations in designing and developing a nanocrystalline soft magnetic material from an amorphous precursor route as one example of the design process. Here, we consider first the effects of alloy composition on intrinsic magnetic properties. This is followed by consideration of alloying additions necessary to produce an appropriate amorphous precursor. Typical experimental steps used to identify the structure and properties of the resulting materials are also illustrated.

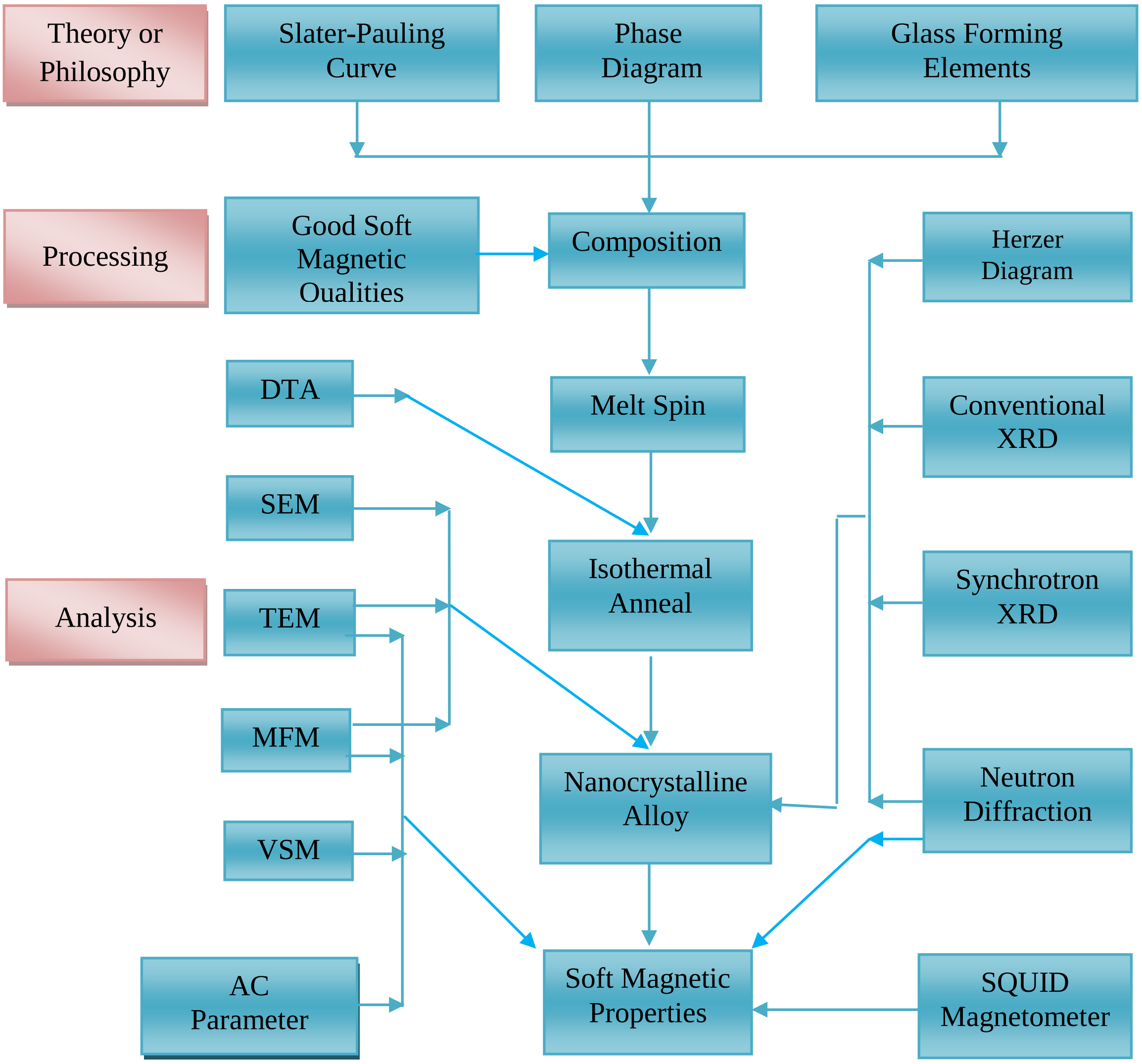

Figure 3.2: Flow chart for the consideration in designing and developing a nanocrystalline soft magnetic material from an amorphous precursor route [90].

3.5 State of Affairs for the Formation of Nanocrystalline State

The Nanocrystalline state is attained by annealing at temperatures between 500°C-650°C, which is suitable for crystallization of *bcc* Fe. The resulting microstructure is characterized by randomly oriented, ultrafine grains of bcc Fe-Si of about, 25 at % of silicon with typical grain size of 15-25 nm embedded in a residual amorphous matrix, having a distance of about 1-2 nm between the crystallites. These features are basis for the outstanding soft magnetic properties included by the high values of the initial permeability of about 10^5 Wb/(A-m)and corresponding low coercivities of less than 1 A/m. The nanocrystalline microstructure and the accompanying soft magnetic properties are rather sensitive to the precise annealing conditions within a broad range of annealing temperature $T_a \approx 500\text{-}650^0$C. They develop in a relatively small period of time (about 10-15 minutes). It does not improve much even after prolonged heat treatment for several hours [91].

A typical heat treatment around at $T_\mathrm{a} = 540^0$C in most cases yield a nanocrystalline microstructure in the quasi-equilibrium state. Only annealing at elevated temperatures above 600°C, leads to the precipitation of small fraction of boride compounds like Fe_2B or Fe_3B. The formation of the particular nanocrystalline structure is essentially related to the combined addition of Cu and Nb or Cu and Cr due to their low solubility in *bcc* Fe. Copper enhances the nucleation of the *bcc* grains while niobium impedes coarsening and at the same inhibits the formation of boride compounds. The microstructure evolution is schematically illustrated if Figure 3.3 and can be summarized as follows:

The phase separation tendency between Cu and Fe leads to the formation of Cu rich clusters, about 5 nm in size and probably still amorphous, in the initial stage of annealing before the onset of the primary crystallization of the *bcc* Fe-Si phase [91].

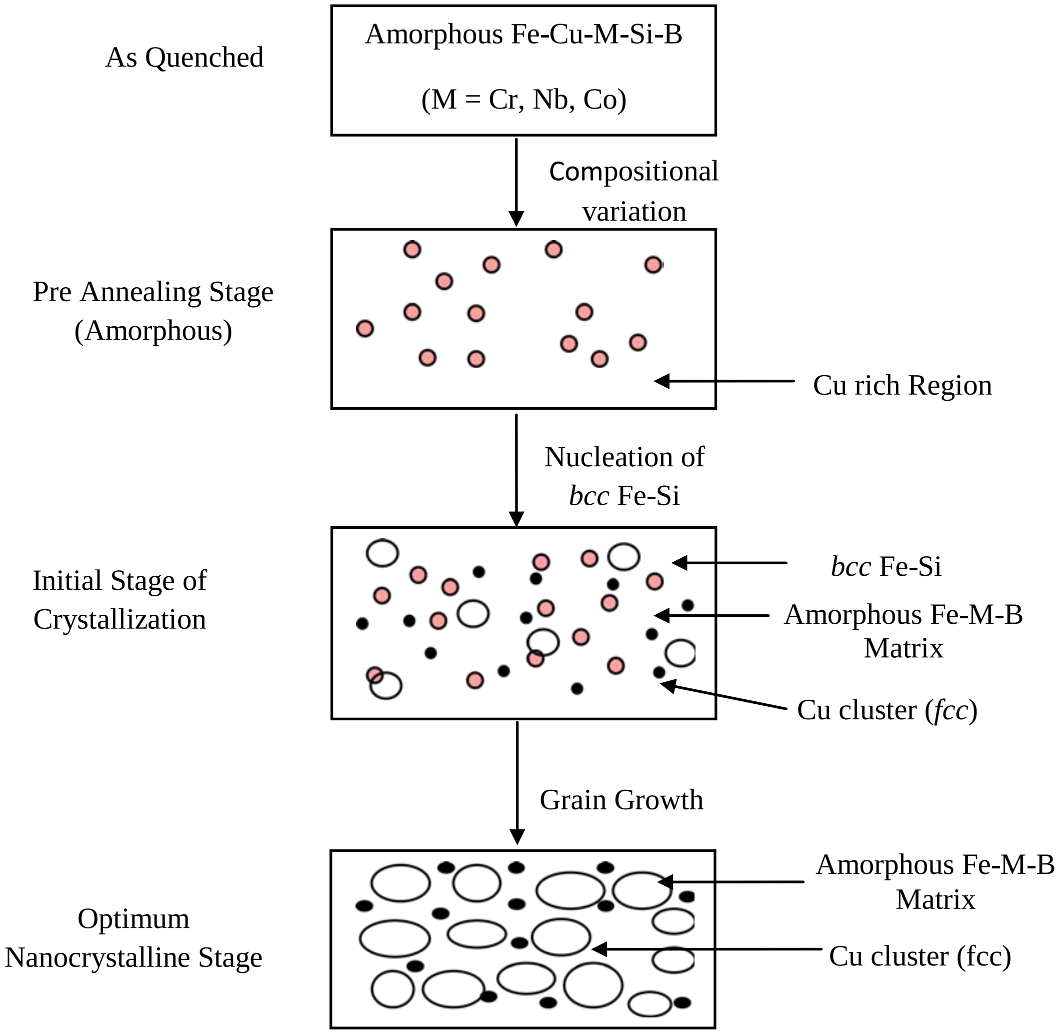

Figure 3.3: Schematic illustration of the formation of the nanocrystallization structure in Fe-Cu-Nb-Si-B alloys based on atom probe analysis results and transmission electron microscopy observation [73-92].

The presence of Nb, hereby seems to endorse the configuration of these Cu rich clusters on a much finer scale than in a Nb free alloy composition [73]. The cluster configuration causes a concentration variation of Fe, since Cu is not soluble in Fe. Thus, the regions in between the Cu-rich clusters provide a significantly increased density of nucleation sites for the crystallization of *bcc* Fe. The consequence is an extremely fine nucleation of *bcc* Fe-Si crystallites at a high rate which subsequently grow in a diffusion controlled process [92] as the annealing proceeds further. As the bcc Fe-Si phase forms, Nb and B are excluded from the crystallites because of their low solubility in bcc Fe and are enriched in the residual amorphous matrix. At the same time effectively all Si tends to be partitioned into the bcc Fe-Si phase [73, 92]. The enrichment in particular with B and Nb increasingly stabilizes the residual amorphous matrix and thus hinders coarsening of the *bcc* grains. The presence of Nb at the same time inhibits the formation of Fe boride compounds. The transformation finally causes in a metastable two-phase microstructure of *bcc* Fe-Si embedded in an amorphous Fe-Nb-B matrix.

3.6 Techniques Behind Synthesizing Nanocrystalline Alloys

The processing method is necessary to produce alloys in the amorphous state. Circumventing the crystallization process is also necessary for alloy formation in the amorphous state, either as an end product or a precursor to nanocrystallization. The following four synthesis routes are viable for producing alloys for larger scale applications, as opposed to thin film synthesis for microelectronic applications. These syntheses are:

(i) Powder synthesis technique:

Magnetic nanocrystals may be synthesized as free standing powders or nanoencapsulates which must then be compacted to form a bulk alloy with nanocrystalline grains. Examples of these techniques include carbon-arc synthesis, plasma torch synthesis and gas atomization techniques among others.

(ii) Rapid solidification processing:

Amorphous alloys can be produced by a variety of rapid solidification processing routes. These typically require cooling rates $>10^4$ K.sec^{-1} for typical alloys at eutectic composition. Examples of these techniques include splat quenching, melt spinning etc.

(iii) Solidification processing of bulk amorphous alloys:

Bulk amorphous alloys are formed by more conventional solidification routes with a slower rate.

(iv) Crystallization of amorphous precursor:

Bulk alloys nanocrystalline grain can also be produced by solid reaction (crystallization) of an amorphous precursor.

3.7 Conditions Necessary for Preparing Nanocrystalline Materials

The necessary conditions for preparing nanocrystalline materials are:

(i) The magnetic properties are highly dependent on grain size; if the grain size is larger; the magnetic anisotropy would be very high, which in turn will have diverse effect on the soft magnetic properties specially the permeability.

(ii) There should be nucleation centers initiated for the crystallization process to be distributed throughout the bulk of the amorphous matrix.

(iii) There must be a nucleation for stabilizing the crystallites.

(iv) Nanocrystalline materials obtained from crystallization must be controlled so that the crystallites do not grow too big. The grain growth should be controlled so that the grain diameter is within 15-20nm.

(v) The sizes of the grains can be limited to nanometer scale by doping group –II metals etc.

(vi) The stability must be lower and the crystallization temperature must be higher.

3.8 Process of Rapid Solidification

Amorphous metallic alloys are synthesized by rapid solidification processing techniques in alloy systems where the liquid phase remains stable to low temperature and there are competing crystalline phases below the liquidus, *i.e*. systems with deep eutectic. These are typically metastable phases. Amorphous alloys can be produced by a variety of rapid solidification processing routes including splat quenching, melt spinning, gas atomization and condensation from the gas phase. These typically require cooling rates of greater than 10^4 K.sec^{-1} for binary alloys at a eutectic composition. Most common rapid solidification processing is melt spinning system which yields amorphous metallic ribbons of typical thickness 20 μm and gas atomization techniques that yield several μm to submicron powders the smallest of which can be made amorphous. It is being has discussed the thermodynamic and kinetic considerations for the synthesis of amorphous metallic phases. Glass forming ability (GFA) involves suppressing crystallization by preventing nucleation and growth of the stable crystalline phase so as to maintain a metastable quenched liquid phase. The solidification of eutectic liquid involves partitioning of the constituents to for the stable crystalline phase. Glass forming ability can be correlated with the reduced glass-forming temperature, T_{rg}, which is defined as $T_{\mathrm{rg}} = (T_{\mathrm{L}}-T_{\mathrm{g}})/T_{\mathrm{L}}$, where T_{L} and T_{g} are the liquidus and glass transition temperature respectively.

Five criteria have been enumerated for promoting the partition less (*i.e.* with no composition change) freezing of a liquid to form a metallic glass. These are:

(i) **Quenching to below the T_0 curve:** The T_0 curve represents the temperature below which there is no thermodynamic driving force for partitioning and the liquid freezes into a solid of the same composition.

(ii) Morphological stability depends on the comparison of imposed heat flow and the velocity of the interface between the amorphous solid and liquid phase.

(iii) **Heat flow:** The super cooling of the liquid phase must exceed L/C, where L is the latent heat of solidification and C is the specific heat of the liquid, so as to prevent segregation.

(iv) **Kinetic criteria:** A criteria such as cooling rate, R_c, for quenching in the liquid phase is empirically known to depend intimately on the reduced glass forming temperature, T_{rg}.

(v) **Structural:** Different atomic size ratios typically with difference exceeding ≈13% are desired to retard the diffusion motion necessary for partitioning.

3.9 Rapid Quenching Method

As shown in a schematic diagram in Figure 3.4, the rapid quenching technique apparatus consists mainly of a copper roller, an induction heater and a nozzle. A variable speed motor drove the roller via a tooth belt. The angular velocity was 2000 rev/min. Use of log wheel rotation enabled us to vary the surface velocity in the range of 20 to 30 m.s^{-1}. The diameter of the copper roller was 10 cm. Roller is usually made up of copper due to its thermal conductivity and mechanical softness, which allow us for easy clearing and polishing.

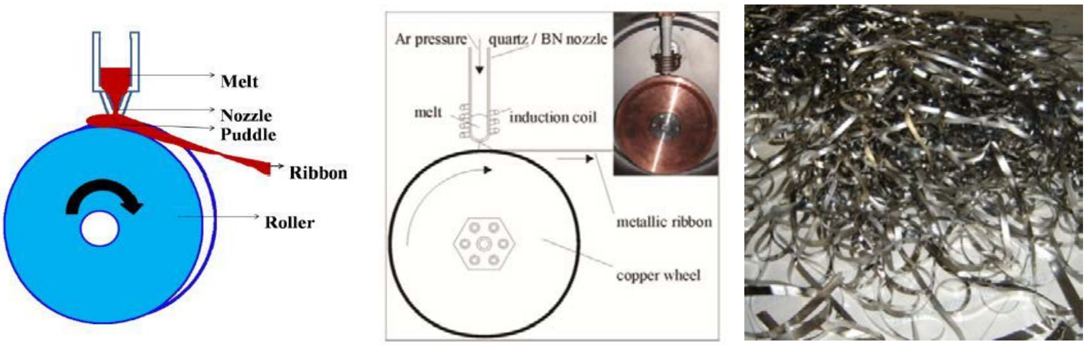

Figure 3.4: Thin layer of molten alloy intimate contact with the outer surface of metallic rotor is quenched in to amorphous ribbon.

In this process one has to consider that vibration of the roller should be well below the high frequency vibration of the melt puddle to avoid any influence of it on the geometry and uniformity of the ribbon. One has to be careful and see that the ribbon does not remain in contact with surface of the roller for a whole revolution and get heated, from the back. Thus a roller of bigger diameter is preferred. The induction heater coil is made of hollow copper tubing, which is cooled simultaneously by circulating water is to be adjusted to produce proper temperature gradient. This mechanism is used to avoid blocking the nozzle due to sudden cooling of the melt on its way out of the crucible. The quartz tube have outer diameter 20 mm which is narrowed down conically to 1mm hole up to the nozzle of whole hole size 0.1 to 0.2 mm. The nozzle geometry is selected to minimize the contraction in the cross-sectional area of the molten jet as it leaves the nozzle orifice. Quartz tube is suitable for repeated use in several successful runs and should be transparent to make the melting process visible. It should withstand at sudden changes in temperature.

3.10 Description of the Procedure Preparation of the Amorphous Ribbons

First we took 20gm of the alloys and melted in an induction furnace and then quenched in water to get master alloys. This results in a button shaped specimen weight of which is also about 20gm, Special care was taken to ensure the homogenous mixing of the alloy composition, by turning over and re melting each button few times. Prepared button shaped mother alloys was then introduced in the quartz tube. Prepared button shaped mother alloys was then introduce in the quartz tube. The quartz tube is connected from the top by rubber ‘O’ rings and metal rings to the cylinder containing argon through a valve and a pressure gauge. After proper cleaning of the roller surface and adjusting its speed to a desired value, as measured by the stroboscope the induction furnace is powered using high frequency generator. When the melting temperature is reached as observed through a protective spectacle, the injection pressure is applied by opening the pressure valve. To avoid the turbulence of the wind, arising from the high speed of the roller in disturbing the melt puddle, cotton pad and metallic shield are usually used just beneath the roller. To avoid oxidation of the ribbon during its formation an inert gas atmosphere was created around the roller by a slow stream of argon. The speed of the roller, the volumetric flow rate, the diameter, the substrate orifice distance, the injection angle etc are adjusted by trial and error method to get the best result *i.e.* The quality and geometry of the ribbons.

3.11 Important Factors to Control the Thickness of Ribbons

i. Rotating speed

(a) Angular velocity w = 2000 rev.min^{-1}

(b) Surface velocity v = 20 m.sec^{-1}

ii. Gap between nozzle and rotating copper drum h = 100 to 150 μm

iii. Oscillation of rotating copper drum both static and dynamic have maximum

displacement 1.5 to 5 μm.

iv. Pressure = 0.3 argon atmosphere.

v. Temperature of molten metals $T_m \cong 2900^0$C; otherwise quartz tube would be melted.

vi. A steady flow of the molten metal on the surface of the rotating drum needs to be ensured.

3.12 Confirmation of Amorphousity of Ribbons

The amorphousity of the twelve ribbons in as cast condition have been confirmed by X-ray diffraction using Cu-K_α radiation (λ = 1.3518 Å) using Phillips (PW 3040) X Pert PRO XRD system. From the Figure 3.5 (a) and (b) no sharp peak in x-ray diffraction pattern are observed which represent the crystalline phase within the scanning range. Only a broad hump with insignificant intensity is found in diffraction pattern at an angle 2θ corresponding to fundamental reflection from (110) plane, no way this can regarded as crystalline state. The hump for an amorphous phase generally covers around 2θ = 10 degree. By observing the average XRD pattern we may conclude that all of our samples ($Fe_{73.5-x}Cr_xNb_3Cu_1Si_{13.5}B_9$ and $Fe_{76.5-x}Nb_xCu_1Si_{13.5}B_9$) are purely amorphous in as cast condition.

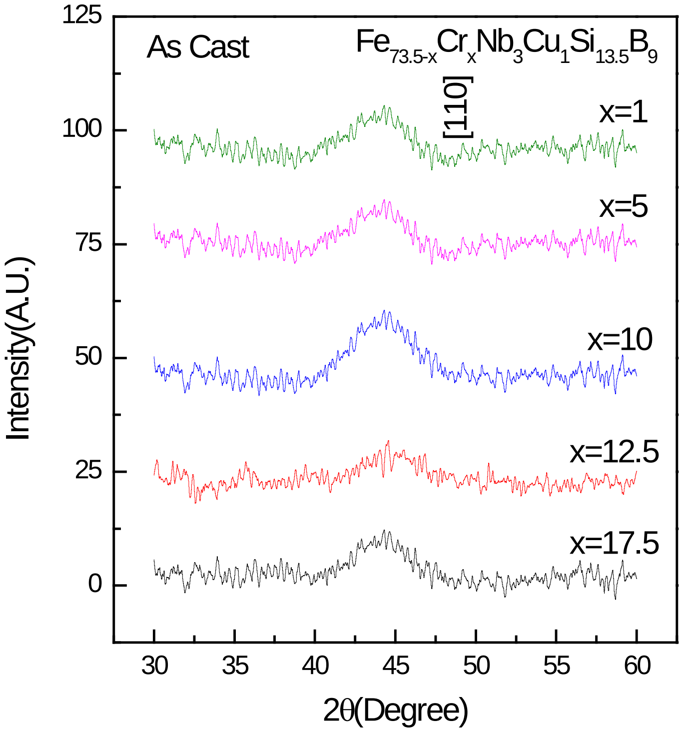

(a)

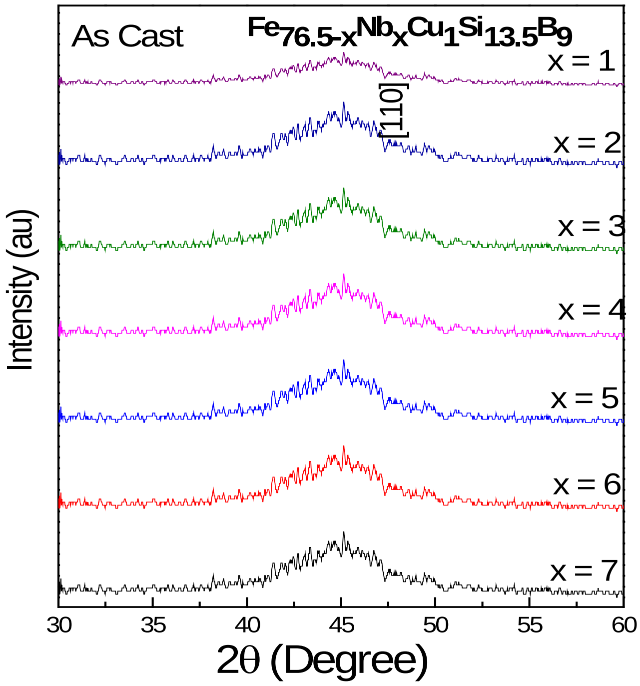

(b)

Figure 3.5: XRD pattern in as cast condition for the alloys (a) $Fe_{73.5-x}Cr_xNb_3Cu_1$-$Si_{13.5}B_9$ and (b) $Fe_{76.5-x}Nb_xCu_1Si_{13.5}B_9$.

Chapter 4

Experimental Techniques

4.1 Melt Spin System

Amorphous alloys in the form of ribbons have been prepared by single roller melt-spinning technique in air. Melt spin system showed in Figure 4.1(a) is a small laboratory system, especially designed for production of amorphous and micro crystalline ribbons. Melting of material is performed by a high frequency generator with water cooled induction coil. Molten material flows through a slot on a fast rotating copper wheel. The melt is quenched with a cooling rate of about 10^5 K.sec^{-1}, which solidifies in an amorphous structure.

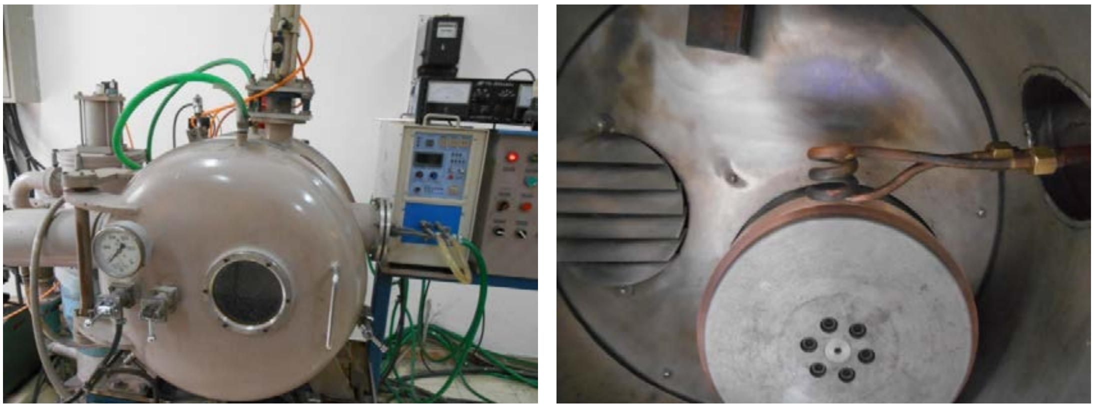

Figure 4.1: (a) Setup for melt spinning system and interior.

4.1.1 Preparation of Fe-Based Hard Magnetic Ribbon by Melt Spin System

The compositions of Fe-Si-B based soft magnetic materials are $Fe_{73.5-x}Cr_xCu_1Nb_3Si_{13.5}B_9$ and $Fe_{76.5-x}Nb_xCu_1Si_{13.5}B_9$ where x substituted as Cr and Nb respectively. The purity and basis of the constituent elements are Fe (99.98%), Cu (99+%), Nb (99.8%), Cr (99.5%), B (99.5%) and Si (99.9%) as obtained from Johnson Mathey, Alfa Aesar. Constituent elements of the alloys have been weighed in the right amount and composed into a quartz tube. The tube has been evacuated down to a pressure of 10^{-6} mbar. Ingots of each composition were prepared using induction melting associated with melt-spin machine. The ingots are then interleaved into an additional quartz tube. An orifice of dimension of 6 mm width and 1 mm thickness has been placed at the closed-end of this tube. Ingots are then melted using induction melting up to the melting point of all the constituents. Appropriate temperature of the melt initially assumed from the color of the melt by eye-estimation. The melt is then purged using Ar pressure to produce ribbon on an average 6 mm wide and 20-25 μm thick, shown in Figure 4.1(b).

Figure 4.1:(b) Prepared ribbons by melt spinning system.

4.2 Thermal Analysis Techniques

Thermal analysis comprises a group of techniques in which a physical property of a substance is measured as a function of temperature, while the substance is subjected to a controlled temperature program. In differential thermal analysis, the temperature difference that develops between a sample and an inert reference material is measured, when both are subjected to identical heat–treatments. The related technique of differential scanning calorimetry relies on differences in energy required to maintain the sample and reference at an identical temperature.

4.2.1 Differential Scanning Calorimetry (DSC)

DSC is a thermo analytical technique in which the difference in the amount of heat required to increase the temperature of a sample and reference are measured as a function of temperature. Both the sample and reference are maintained at very nearly the same temperature throughout the experiment. Generally, the temperature program for a DSC analysis is designed such that the sample holder temperature increases linearly as a function of time [93]. The reference sample should have a well-defined heat capacity over the range of temperatures to be scanned. The basic principle underlying this technique is that, when the sample undergoes a physical transformation such as phase transitions, more (or less) heat will need to flow to it than the reference to maintain both at the same temperature. Whether more or less heat must flow to the sample depends on whether the process is exothermic or endothermic [94]. For example, as a solid sample melts to a liquid it will require more heat flowing to the sample to increase its temperature at the same rate as the reference. This is due to the absorption of heat by the sample as it undergoes the endothermic phase transition from solid to liquid. Likewise, as the sample undergoes exothermic processes (such as crystallization) less heat is required to raise the sample temperature. By observing the difference in heat flow between the sample and reference, differential scanning calorimeters are able to measure the amount of heat absorbed or released during such transitions. DSC may also be used to observe more subtle phase changes, such as glass transitions [95]. DSC is widely used in industrial settings as a quality control instrument due to its applicability in evaluating sample purity and for studying polymer curing. An alternative technique, which shares much in common with DSC, is differential thermal analysis (DTA). In this technique it is the heat flow to the sample and reference that remains the same rather than the temperature. When the sample and reference are heated identically phase changes and other thermal processes cause a difference in temperature between the sample and reference [95]. Both DSC and DTA provide similar information; DSC is the more widely used between these two techniques.

4.2.2 DSC Instrumentation

A typical differential scanning calorimeter consists of two sealed pans: a sample pan and a reference pan (which is generally an empty sample pan). These pans are often covered by or composed of aluminum, which acts as a radiation shield. The two pans are heated, or cooled, uniformly while the heat flow difference between the two is monitored. This can be done at a constant temperature (isothermally), but is more commonly done by changing the temperature at a constant rate, a mode of operation also called temperature scanning [34].

During the determination, the instrument detects differences in the heat flow between the sample and reference. This information is sent to an output device, most often a computer, resulting in a plot of the differential heat flow between the reference and sample cell as a function of temperature. When there are no physical or chemical thermodynamic processes occurring, the heat flow difference between the sample and reference varies only slightly with temperature, and shows up as a flat or very shallow base line on the plot [67]. However, an exothermic or endothermic process within the sample results in a significant deviation in the difference between the two heat flows. The result is a peak in the DSC curve. Generally, the differential heat flow is calculated by subtracting the sample heat flow from the reference heat flow. When following this convention, exothermic processes will show up as positive peaks (above the baseline) while peaks resulting from endothermic processes are negative (below the baseline). The sample (in a condensed form such as powder, liquid, or crystal) is generally placed in an aluminum sample pan, which is then placed in the sample cell. The reference consists of a matched empty aluminum sample pan that is placed in the reference cell of the instrument. The sample pans are designed to have a very high thermal conductivity. Sample sizes generally range from 0.1 to 100 mg. The instrument cells are often airtight to shield the sample and reference from external thermal perturbations. This also allows experiments to be performed under variable pressures and atmospheres [95].

Figure 4.2: Set up of differential scanning calorimeter.

4.2.3 Heat Flux DSC (hf DSC)

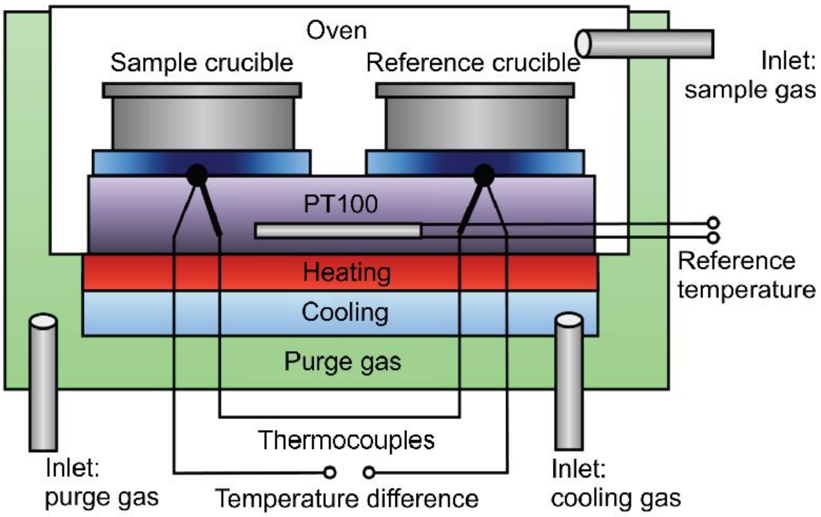

Figure 4.3: Diagram of a heat flux differential scanning calorimeter.

There are two main types of differential scanning calorimeters: heat flux DSC and power compensation DSC. In a heat flux calorimeter, heat is transferred to the sample and reference through a disk made of the alloy constantan or in some cases, silver. The heat transported to the sample and reference is controlled while the instrument monitors the temperature difference between the two. In addition to its function in the heat transfer, this disk serves as part of the temperature-sensing unit. The sample and reference reside on raised platforms on the disk. Under each of these platforms there is a chromel (chromel is an alloy containing chromium, nickel and sometimes iron) wafer. The junction between these two alloys forms a chromel-constant thermocouple. The signal from these sensors is then used to measure the differential heat flow. The temperature is typically monitored by chromel-alumel thermocouples attached beneath the chromel wafers.

4.2.4 Power Compensate DSC (pc DSC)

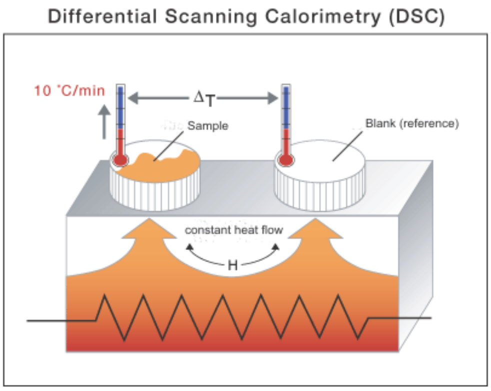

Figure 4.4: Power compensate differential scanning calorimeter.

In power compensated calorimeters, separate heaters are used for the sample and reference. This is the classic DSC design pioneered by the Perkin-Elmer® company. Both the sample and reference are maintained at the same temperature while monitoring the electrical power used by their heaters. The heating elements are kept very small (≈ 1 gm) in order to ensure that heating, cooling, and thermal equilibration can occur as quickly as possible. The sample and reference are located above their respective heaters, and the temperatures are monitored using electronic temperature sensors located just beneath the samples. Generally platinum resistance thermometers are used due to the high melting point of platinum [96].

Electronically, the instruments consist of two temperature control circuits. An average temperature control circuit is used to monitor the progress of the temperature control program. This circuit is designed to assure that the temperature scanning program set by the operator is the average temperature of the sample and reference. A differential temperature control circuit is used to determine the relative temperatures of the sample and reference, and adjust the power going to the respective heaters in such a way as that maintain same temperature for both. The output of the differential temperature control circuit is used to generate the DSC curve.

4.2.5 Understanding DSC Curves

The result of a DSC experiment is a heating or cooling curve. This curve can be used to calculate enthalpies of transitions. This is done by integrating the peak corresponding to a given transition. It can be shown that the enthalpy of transition can be expressed using the following equation [50, 97]

$$\Delta H = KA \tag{4.1}$$

where ΔH is the enthalpy of transition, K is the calorimetric constant, and A is the area under the curve. The calorimetric constant will vary instrument to instrument, and can be determined by analyzing a well-characterized sample with known enthalpies of transition.

4.2.6 Applications of Differential Scanning Calorimetry

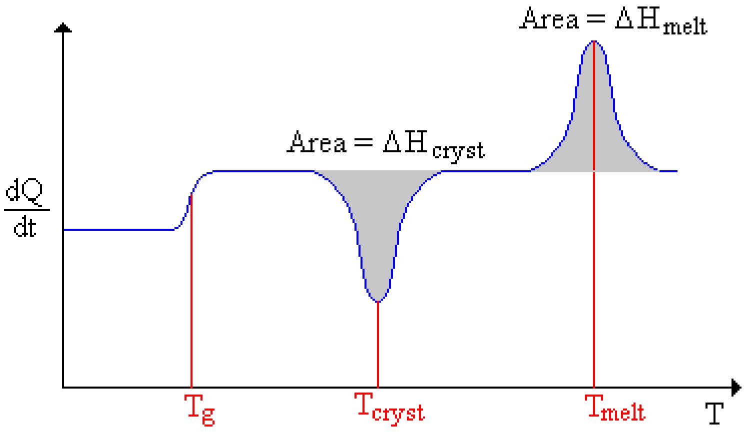

Figure 4.5: A schematic DSC curve demonstrating appearance of several common features.

Differential scanning calorimetry can be used to measure a number of characteristic properties of a sample. Using this technique it is possible to observe fusion and crystallization events as well as glass transition temperatures, (T_{g}). DSC can also be used to study oxidation, as well as other chemical reactions [98].

Glass transitions may occur as the temperature of an amorphous solid is increased. These transitions appear as a step in the baseline of the recorded DSC signal. This is due to the sample undergoing a change in heat capacity, no formal phase change occurs.

As the temperature increases, an amorphous solid will become less viscous. At some point the molecules may obtain enough freedom of motion to spontaneously arrange themselves into a crystalline form. This is known as the crystallization temperature (T_{cryst}) [99]. This transition from amorphous solid to crystalline solid is an exothermic process, and results a peak in the DSC signal. As the temperature increases the sample eventually reaches its melting temperature (T_m). The melting process results in an endothermic peak in the DSC curve. The ability to determine transition temperatures and enthalpies makes DSC an invaluable tool in producing phase diagrams for various chemical systems. DSC may also be used in the study of liquid crystals. As matter transitions between solid and liquid it often goes through a third state, which displays properties of both phases. This anisotropic liquid is known as a liquid crystalline or meso amorphous state. Using DSC, it is possible to observe the small energy changes that occur as matter transitions from a solid to a liquid crystal and from a liquid crystal to an isotropic liquid. Using differential scanning calorimetry to study the oxidation stability of samples generally requires an airtight sample chamber. Usually, such tests are done isothermally by changing the atmosphere of the sample. First, the sample is brought to the desired test temperature under an inert atmosphere, usually nitrogen. Then, oxygen is added to the system. Any oxidation that occurs is observed as a deviation in the baseline. Such analyses can be used to determine the stability and optimum storage conditions for a compound.

DSC is widely used in the pharmaceutical and polymer industries. For the polymer chemist, DSC is a handy tool for studying curing processes, which allows the fine tuning of polymer properties. The cross-linking of polymer molecules that occurs in the curing process is exothermic, resulting in a positive peak in the DSC curve that usually appears soon after the glass transition. In the pharmaceutical industry it is necessary to have well-characterized drug compounds in order to define processing parameters. For instance, if it is necessary to deliver a drug in the amorphous form, it is desirable to process the drug at temperatures below those at which crystallization can occur [99].

In food science research, DSC is used in conjunction with other thermal analytical techniques to determine water dynamics. Changes in water distribution may be correlated with changes in texture. Similar to material science studies, the effects of curing on confectionery products can also be analyzed. DSC curves may also be used to investigate drugs and polymers purities. This is possible because the temperature range over which a mixture of compounds melts is dependent on their relative amounts. This effect is due to a phenomenon known as freezing point depression, which occurs when a foreign solute is added to a solution. Consequently, less pure compounds will exhibit a broadened melting peak that begins at lower temperature than a pure compound. SDT 2960 simultaneous DSC-TGA measures heat flow to or from a sample as a function of temperature and time. The heat flow and temperature of the sample are monitored in comparison with the reference material. The amount of energy absorbed (endotherm) or evolved (exotherm) as the sample undergoes physical or chemical changes (*e.g.* melting, crystallization, curing) is measured in calories as a function of the temperature change. Any such transition involving changes in heat capacity (*e.g.* glass transition) is also detected.

4.3 Experimental Technique for X-ray Diffraction

4.3.1 Interpretation of the XRD data

The XRD data consisting of θ_{hkl} values corresponding to the different following structural information of the nanocrystalline ribbon sample.

(i) Identification of phases

(ii) Lattice parameter determination

(iii) Average grain size determination

(iv) Si- content determination in nanograins

(i) Identification of Phases

X-ray diffractometer has become a very popular and useful instrument for routine X-ray analysis of ribbon samples. In fact the diffractometric technique is often preferred to Debye-Scherrer technique [99] owing to its several inherent merits. The most striking difference between the two methods is in the use of different intensity detection and measuring devices. XRD pattern of as-cast indicates just amorphous pattern of said composition. The XRD patterns were identified as *bcc* α-Fe-Si solid solution, which were developed on the amorphous ribbon after heat treatment. The peak pattern was observed for all the samples at different heat treatment temperatures indicating the *bcc* α-Fe-Si phase, which was developed on amorphous ribbons after heat treatment. Present experiment revels that 450°C is not sufficient temperature to start formation of crystalline nanograins of *bcc* Fe-Si on the amorphous ribbon of said alloy composition.

(ii) Determination of Lattice Parameter

Lattice parameter of crystalline *bcc* Fe –Si nanograins was determined for all the two different amorphous compositions at different heat treatment temperatures. Normally, lattice parameter of an alloy composition is determined by the Debye-Scherrer method after extrapolation of the curve. In this method, at least five fundamental reflections are required to determine lattice parameter. In the present case, only one reflection (110) is prominent in all XRD patterns and we would like to understand how the value of lattice parameter changes with annealing temperature. We have, therefore, determined the lattice parameter using only that particular reflection using equation which is known as Bragg's Law [72, 95].

$$2d_{hkl}\sin\theta = \lambda$$

$$i.e.\ d_{hkl} = \frac{\lambda}{2\sin\theta} \tag{4.2}$$

where λ is the wavelength of the X-ray, θ is the diffraction angle and n is an integer representing the order of the diffraction. Again from the Figure 4.6 is shown that

$$\cos^2\alpha + \cos^2\beta + \cos^2\gamma = 1 \tag{4.3}$$

$$or\quad d = \frac{a}{h}\cos\alpha \Rightarrow \cos\alpha = d\frac{h}{a}$$

Similarly $\cos\beta = d\frac{k}{b}$ and $\cos\gamma = d\frac{l}{c}$

Now substitute the values into equation (4.3) we get

$$d^2\left[\frac{h^2}{a^2} + \frac{k^2}{b^2} + \frac{l^2}{c^2}\right] = 1$$

$$\text{or}\qquad d^2 = \frac{1}{\left[\frac{h^2}{a^2} + \frac{k^2}{b^2} + \frac{l^2}{c^2}\right]}$$

for cubic lattice *a* = *b* = *c*

$$\text{So we have}\qquad d = \frac{a}{\sqrt{h^2+k^2+l^2}} \tag{4.4}$$

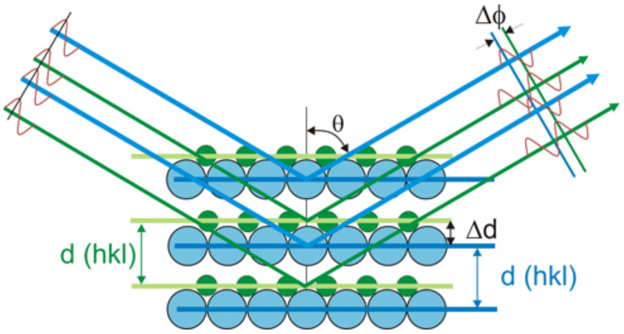

Figure 4.6: Bragg reflection for parallel incident rays.

where *h*, *k*, *l* are the indices of the crystal planes. We get d_{hkl} values from the computer using software. So we got ten '*a*' values for ten reflection planes such as a a_1 , a_2 a_3 …. .... etc. Determine the exact lattice parameter for each sample, through the Nelson-Riley extrapolation method. The values of the lattice parameter obtained from each reflected plane are plotted against Nelson-Riley function [34]. The Nelson-Riley function *F* (*θ*), can be written as

$$F(\theta) = \frac{1}{2}\left[\frac{\cos^2\theta}{\sin\theta} + \frac{\cos^2\theta}{\theta}\right] \tag{4.5}$$

where *θ* is the Bragg's angle. Now drawing the graph of 'a' vs *F*(*θ*) and using linear fitting of those points will give us the lattice parameter 'a_0'. This value of 'a_0' at *F*(*θ*) = 0 or *θ* = 90°. These 'a_0's are calculated with an error estimated to be ± 0.0001Ǻ.

Rules for determining the diffracting {*hkl*} planes in cubic crystals

(iii) Determination of the Grain Size

The aim of the present study is to determine the nanocrystalline grain size for all the heat treatment samples of the alloy composition, where Scherrer's methods employed. The XRD pattern of (110) reflection for different steps of heat treatment temperature of the alloy composition was used to calculate grain size. Grain size is determine by using the Scherrer's formula [84],

$$D_g = \frac{0.9\lambda}{\beta \cos\theta} \tag{4.6}$$

Where, λ = 1.54178Å for Cu-K$_\alpha$ radiation and β = *FWHM* (full width at half maximum) of the peak in radiant. Considering β in degree, we get from Scherrer's formula,

$$D_g = \frac{79.5}{\beta \cos\theta} \tag{4.7}$$

All the values of grain size for every steps of heat treatment temperature of the alloy composition were determined. The FWHM of the peak is large at the lower temperature which getting smaller with the increase of heat treatment temperature.

(iv) Determination of Si-Content in Nanograins

Crystalline nanograins were formed on the ribbon in the process of heat treatment with the alloy composition of Fe-Si. It is therefore important to determine the concentration of Fe and Si in the nanograin. As because the alloys are consists of Fe and Si and we have experimentally determined the lattice parameter of the alloy nanograins for the two compositions at different temperatures. It is easy to calculate the Si content in the nanograins [100]. Where, a simple equation is constructed to calculate Si content from lattice parameter. The equation is

$$X = \frac{(a_0 - 2.8812)}{0.0022}, \tag{4.8}$$

$$b = -\,467a_0 + 1342.8 \tag{4.9}$$

where X/b is at.% Si in the nanograins, a_0 is the determined lattice parameter of nanograins. Si contents for the nanograins develop during the isothermal annealing at various temperatures have been calculated.

4.3.2 Polycrystalline Diffraction

About 95% of all solid materials can be described as crystalline. When X-rays interact with a crystalline substance (Phase), one gets a diffraction pattern. In 1919 A.W. Hull gave a paper titled, “A New Method of Chemical Analysis”. Here he pointed out that, every crystalline substance gives a pattern; the same substance always gives the same pattern; and in a mixture of substances each produces its pattern independently of the others. The X-ray diffraction pattern of a pure substance is, therefore, like a fingerprint of the substance. The powder diffraction method is thus ideally suited for characterization and identification of polycrystalline phases. Today about 50,000 inorganic and 25,000 organic single components, crystalline phases, and diffraction patterns have been collected and stored on magnetic or optical media as standards. The main use of powder diffraction is to identify components in a sample by a search/match procedure. Furthermore, the areas under the peak are related to the amount of each phase present in the sample.

4.3.3 Philips X’Pert Pro X-ray Diffractometer

The X'Pert PRO diffraction system utilizes a modular system approach to provide performance for applications ranging from routine characterization to in-depth research investigations. The Pre-FIX (Pre-aligned Fast-Interchangeable X-ray optics) concept enables the diffraction system to be reconfigured in a few minutes without the need for re-alignment to handle different types of analysis. A suite of data analysis software from Philips is also available. During x-ray diffraction analysis, X-ray beams are reflected off the parallel atomic layers within a mineral over a range of diffraction angles. Because the x-ray beam has a specific wavelength, for any given 'd-spacing' (distance between adjacent atomic planes) there are only specific angles at which the exiting rays will be 'in phase' and therefore, will be picked up by the detector producing a peak on the 'diffractogram'. Just like a 'fingerprint', every mineral has its own distinct set of diffraction peaks that can be used to identify it.

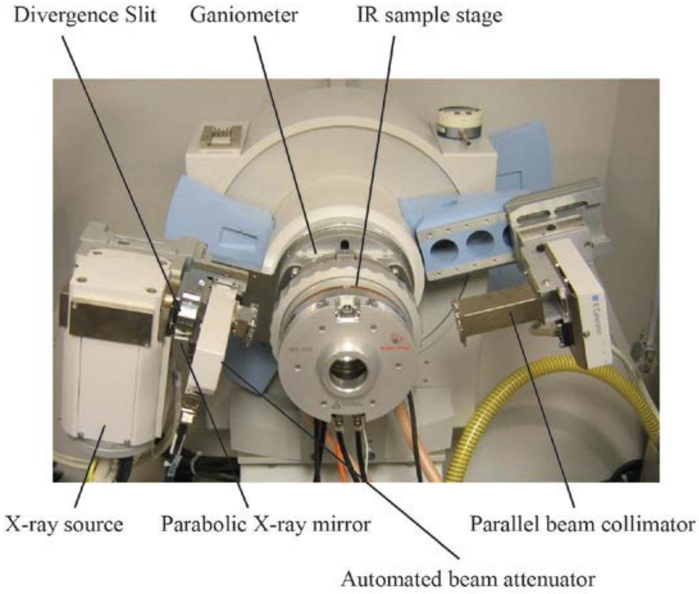

Figure 4.7: Philips PW 3040 X pert pro XRD.

The system enables us to do the analysis on phase identification and quantification, as well as crystal structure studies. The specifications of the system are:

- **X-ray sources**: 3 kW Copper tube
- **Optics**: Focussing and parallel Pre-Fix optics, programmable slits, tunable diffracted beam monochromator
- **Detectors**: Xe proportional counter and solid state X'cellerator
- **Sample Stages**: Single sample holder, 15-sample changer
- **Variable Temperature Capabilitiy**: Anton-Paar 77-725K and 300-1475K cameras
- **Software and Databases**: Data Collector, X'Pert Plus crystallographic analysis software with Rietveld capability, ProFit line profile analysis software
- **Instrument Statistics**: The system uses Cu K_α radiation that has a wavelength of 1.54178 Å. Analyses are commonly run using a 40kV 45mA X-ray tube

voltage, a 0.04° solar slit, 1° divergence and antiscatter slits, and a 1/2° (for powder) or 1/4° (for clays) receiving slit.

4.3.4 Applications of X-ray Diffractions

Phase identification: The most common use of powder (polycrystalline) diffraction is chemical analysis. This can include phase identification (search/match), investigation of high/low temperature phases, solid solutions and determinations of unit cell parameters of new materials.

Polymer crystallinity: A polymer can be considered partly crystalline and partly amorphous. The crystalline domains act as a reinforcing grid, like the iron framework in concrete, and improve the performance over a wide range of temperature. However, too much crystallinity causes brittleness. The crystallinity parts give sharp narrow diffraction peaks and the amorphous component gives a very broad peak . The ratio between these intensities can be used to calculate the amount of crystallinity in the material.

Residual stress: Residual stress is the stress that remains in the material after the external force that caused the stress has been removed. Stress is defined as force per unit area. Positive values indicate tensile (expansion) stress; negative values indicate a compressive state. The deformation per unit length is called strain. The residual stress can be introduced by any mechanical, chemical or thermal process, *e.g.* machining, plating and welding.

The principals of stress analysis by the X-ray diffraction is based on measuring angular lattice strain distributions. That is, we choose a reflection at high 2θ and measure the change in the d-spacing with different orientations of the sample. Using Hooke's law the stress can be calculated from the strain distribution.

Texture analysis : The determination of the preferred orientation of the crystallites in polycrystalline aggregates is referred to as texture analysis, and the term texture is used as a broad synonym for preferred crystallographic orientation in the polycrystalline material, normally a single phase. The preferred orientation is usually described in terms of pole figures.

Grain size : When the size of the individual crystals is less than about 1000 Ǻ, grain size can be determined from line broadening,

$$D_g = \frac{0.9\lambda}{\beta \cos\theta} \tag{4.10}$$

where, D_g = broadening of diffraction line measured at half its maximum intensity (radians). All diffraction lines have a measurable breadth, even when the crystal size exceeds 1000 Ǻ, due to such causes as divergence of the incident beam and size of the sample (in Debye cameras)and width of the X-ray source (in diffractometer) [101]. The breadth *B* refers however, to the extra breadth, or broadening, due to the particle-size effect alone. In other words, *B* is essentially zero when the particle-size effect alone. In other words, B is essentially zero when the particle size exceeds about 1000Ǻ.

4.4 Electron Microscopy

4.4.1 Field Emission Scanning Electron Microscopy

To observe morphology of the synthesized powders we used field emission scanning electron microscope, FESEM (JEOL JSM 7600F). Powder samples were adhered with carbon tape that was attached to a copper stub. Samples were made conductive, coated with platinum by ion sputtering method. Then sample holder was mounted on a holder and inserted in FESEM. The micrographs obtained from FESEM analysis was used for microstructural study [102].

Figure 4.8: Field emission scanning electron microscope (FESEM).

4.4.2 Transmission Electron Microscopy

The transmission electron microscope (TEM) is used to differentiate the microstructure of materials with very high spatial resolution. Information about the surface morphology, crystal structure and imperfections, crystal phases and composition can be obtained by a combination of electron imaging (2.0 Å point resolution), electron diffraction, energy dispersive X-ray spectroscopy, Electron Energy Loss Spectroscopy with small (~ 1 nm) probe capabilities. The small probe can be positioned on very fine features in the sample for microdiffraction information or analysis of X-rays for compositional information. The spatial resolution for this compositional analysis in TEM is much higher, on the order of the probe size.

Conversely the signal is much smaller as sample is very thin and therefore less quantitative [103].

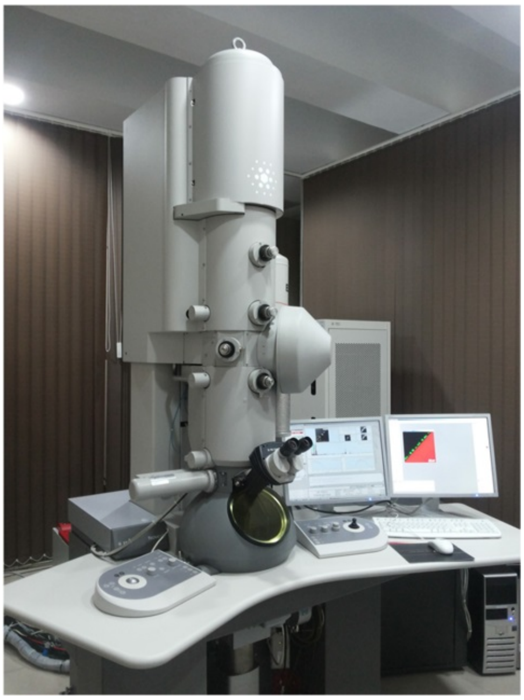

Figure 4.9: Transmission electron microscope (TEM).

The high brightness field-emission gun improves the sensitivity and resolution of X-ray compositional analysis over that obtainable with more customary thermionic sources. The transmission electron microscope uses a high energy electron beam transmitted through a very thin sample to image and analyze the microstructure of materials with atomic scale resolution. The electrons are focused with electromagnetic lenses and the image is observed on a fluorescent screen, or recorded on digital camera. The electrons are accelerated at several hundred kV, giving wavelengths much smaller than that of light. However, whereas the resolution of the optical microscope is limited by the wavelength of light, that of the electron microscope is limited by aberrations inherent in electromagnetic lenses. A TEM specimen must be approximately 1000 Å or less in thickness in the area of interest. The entire specimen must fit into a 3mm diameter cup and be less than about 100 microns in thickness.

4.5 Vibrating Sample Magnetometer

The vibrating sample magnetometer (VSM) has become a broadly used instrument for formative magnetic properties of a large diversity of materials: diamagnetics, paramagnetics, ferromagnetics, and antiferromagnetics. This experimental technique was invented in 1956 by Simon Foner, a scientist of the MIT. EGG Princeton Applied Research (EGG PAR) was the world leader company that started the commercialization of this magnetometers in the sixties. It has a flexible design and combines high sensitivity with easy of sample mounting and exchange. Samples may be interchange rapidly even at any operating temperature.

Figure 4.10: Vibrating sample magnetometer (VSM).

Measurements of magnetic moments as small as 5×10^{-5} emu are possible in magnetic fields from 0 to 9 Tesla (or higher). Maximum applied fields of 2-3 Tesla or 9 Tesla are reached by using conventional laboratory electromagnets and superconducting solenoids, respectively. Vibrating sample magnetometers normally operate over a temperature range from 2.0 to 1050 K. Magnetic properties of powders, bulk and thin films can be studied by VSM.

4.5.1 Principle of VSM

If a sample of any material is placed in a uniform magnetic field, created between the poles of a electromagnet, a dipole moment will be induced. If the sample vibrates with sinusoidal motion a sinusoidal electrical signal can be induced in suitable placed pick-up coils. The signal has the same frequency of vibration and its amplitude will be proportional to the magnetic moment, amplitude, and relative position with respect to the pick-up coils system. Figure 4.11 shows the block diagram of vibrating sample magnetometer.

The sample is fixed to a small sample holder located at the end of a sample rod mounted in a electromechanical transducer. The transducer is driven by a power amplifier which itself is driven by an oscillator at a frequency of 90 Hertz. So, the sample vibrates along the Z axis perpendicular to the magnetizing field. The latter induced a signal in the pick-up coil system that is fed to a differential amplifier. The output of the differential amplifier is subsequently fed into a tuned amplifier and an internal lock-in amplifier that receives a reference signal supplied by the oscillator. The output of this lock-in amplifier, or the output of the magnetometer itself, is a DC signal proportional to the magnetic moment of the sample being studied. The electromechanical transducer can move along X, Y and Z directions in order to find the saddle point. Calibration of the vibrating sample magnetometer is done by measuring the signal of a pure Ni standard of known the saturation magnetic moment placed in the saddle point. The basic instrument includes the electromechanical system and the electronic system (including a personal computer), while the costumer should select the electromagnet or superconducting coil system with the appropriate bipolar power supply. Laboratory electromagnets or superconducting coils of various maximum field strengths may be used. For ultra-high magnetic fields a cryogen-free magnets can be also used. For the characterization of soft magnetic materials a pair of Helmholtz coils may be also used. As accessories the costumer must also select a high temperature oven assembly and a liquid helium cryostat [103].

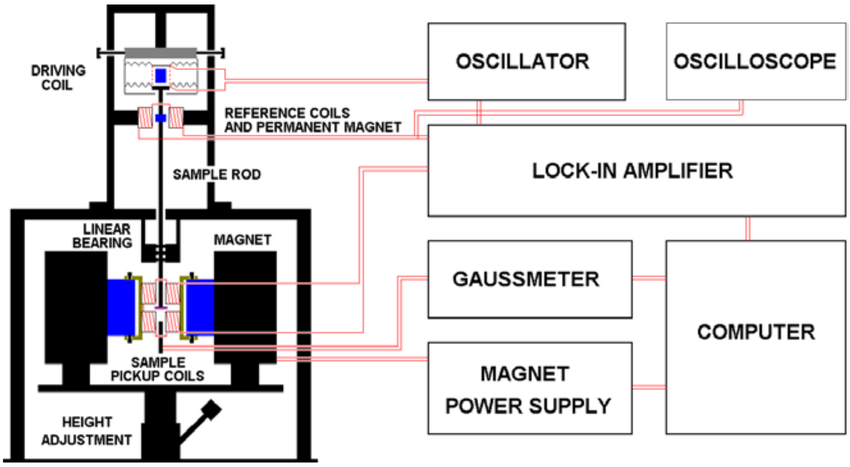

Figure 4.11: Block diagram of vibrating sample magnetometer.

Technical specifications of VSM (typical figure) are shown in Figure 4.11. Maximum sensitivity: 5×10^{-5} emu, Calibrated ranges from 100 to 0.01 emu full scale. Stability of output signal: 0.05 % of full scale per day. Absolute accuracy: better than 2 % angular variation of H: full 360° rotation ~ 0.5°, maximum sample size: 7 mm. Operating temperature range: 2K to 1050 K. Applications using a vibrating sample magnetometer one can measure the DC magnetic moment as a function of temperature, magnetic field, angle and time. So, it allows performing study on susceptibility and magnetization. Frequently performed common measurements are: trace hysteresis loops, susceptibility or saturation magnetization as a function of temperature (thermomagnetic analysis), obtain magnetization curves as a function as a function of angle (anisotropy), and magnetization as a function of time.

4.6 Measurement of Permeability

4.6.1 Inductance Analyzer

The 3255B Precision Magnetics Analyzer provides 2-terminal measurement of inductors and transformers over the frequency range 20Hz to 500 kHz. DC resistance measurements are performed at a drive level of 100 mV. The drive level for AC measurements can be varied from 1 mV to 10 V rms. Automatic level control (ALC) can maintain the drive level at the component. During AC measurements the 3255B can supply a DC bias current which is variable between 1 mA and 1 A and when used with external 3265B DC bias units, up to 125 A DC bias current is available.

Figure 4.12: Wayne Kerr 3255 B inductance analyzer.

The analyzer’s measurement, display and control facilities include:

- Spot frequency measurements
- Multi-frequency measurements at a number of user-defined frequencies
- Display of actual measurement values
- Output of measurement results to an Epson-compatible printer.

All the above functions can be selected via manual front panel control or remote control via the GPIB interface for fully-automated high-speed testing. Self-calibration is performed to set calibration constants for signal processing elements in the measurement hardware and signal generation system, and to compensate for components which drifted with time. To maintain full specified accuracy it should be run at least every three months. To measure the inductance of a component the analyzer should be powered up with the test leads or fixture connected to the front panel BNC connectors. The analyzer should be operated in measurement mode. The component to be measured is connected to the test leads or fixture. The measurement may be performed as single shot mode for single measurement or repetitive mode for continuous measurement.

4.6.2 Details of Impedance Analyzer

The Hewlett Packard 4192A LF Impedance Analyzer can measure eleven impedance parameters absolute value of impedance ($|Z|$), absolute value of admittance ($|Y|$), phase angle (θ), resistance (R), reactance (X), conductance (G), susceptance (B), inductance (L), capacitance (C), dissipation factor (D) and quality factor (Q).

The 4192A can provide measuring frequency, OSC level, and dc bias voltage equivalent to actual operating conditions. The sweep capabilities of the built-in frequency synthesizer and dc bias source permits quick and accurate measurements. The built-in frequency synthesizer can be set to measuring frequency within the range from 5Hz to 13 MHz with 1 mHz maximum resolution. Oscillation level is varied from 5mV to 1.1 V r.m.s value with 1 mV resolution. The internal DC bias voltage source provides ± 35 V in 10 mV increments. Measuring frequency or DC bias voltage can be automatically or manually swept in either direction. OSC level can be manually swept in either direction in 1 mV increments (5mV for levels above 100 mV). Actual test voltage across or test signal current through the device under test is also measured. Thus the 4192A impedance anaqlyzer be used to investigate components and circuits under a wide variety of measurement conditions.

4.6.3 Determination of Real and Imaginary Components of Complex Permeability

Determinations of permeability normally involve the measurements of the change in self-inductance of a coil in the presence of magnetic core. Methods of measurement those are commonly used are:

(i) The LCR bridge method
(ii) Resonance circuits and
(iii) The standing wave method

The behavior of a self-inductance can now be described as follows. If we have an ideal loss less air coil of inductance L_0 , on insertion of magnetic core with permeability μ, the inductance became μL_0. The complex impendence Z of this coil can then be expressed as [80]

$$\begin{aligned} Z = R + iX &= i\omega L_0 \mu\,, \\ &= i\omega L_0 (\mu' - i\mu'') \\ &= \omega L_0 \mu'' + i\omega L_0 \mu' \end{aligned} \tag{4.11}$$

where the resistive part

$$R = \omega L_0 \mu'' \tag{4.12}$$

and the reactive part is

$$X = \omega L_0 \mu' \tag{4.13}$$

The r.f permeability can be obtained from the complex impendence of a coil by equation (4.14). The core is taken in the toroidal form to avoid demagnetizing effects.

4.6.4 Frequency Characteristics of Nanocrystalline Materials

The frequency characteristics of the amorphous of the amorphous ribbons samples *i.e* the permeability spectra, were investigated using an impedance analyzer (LCR) (model no. Wayne Kerr 3255B). The measurement of inductances was taken in the frequency range 1 kHz to 50 kHz. The values of measured parameters of obtained as a function of frequency and the real and imaginary parts of permeability and the loss factor μ' is calculated by using the following formula [104,105].

$$L_s = L_0\mu'$$

$$\mu' = \frac{L_S}{L_0} \tag{4.14}$$

$$\tan\delta = \frac{\mu''}{\mu'}$$

$$\text{and } \mu'' = \mu'\tan\delta \tag{4.15}$$

where, L_S is the self-inductance of the sample core and

$$L_0 = \frac{\mu_0 N^2 S}{\bar{d}\pi}, \tag{4.16}$$

where, L_0 is the inductance of the winding coil without the sample core, N is the number of turns of coil and S is the area of cross section as given below [69]

$$S = m/\pi p\bar{d}, \tag{4.17}$$

m is the mass of ribbon and $\bar{d}$ is the mean diameter of the sample given as follows [106]

$$\bar{d} = \frac{d_1 + d_2}{2} \tag{4.18}$$

The relative quality factor is determined by the ratio $\frac{\mu'}{\tan\delta}$.

4.6.5 Determination of Curie Temperature from Temperature Dependence of A.C. Permeability

The temperature dependence of A. C. permeability was measured by using induction method. A laboratory built technique using an oven in which a heating wire is wound bifillery and two identical induction coils are wound in opposite directions such that the current induced flux in the two coils cancels each other. The whole set up is introduced in an oven. By varying temperature, A.C. permeability of the nanocrystalline amorphous ribbon samples of toroidal shapes as a function of temperature was measured. When the magnetic state inside the amorphous sample changes from ferromagnetic to paramagnetic, the permeability falls sharply. From the sharp fall at specific temperature the T_c is determined.

4.7 Mössbauer Spectroscopy

4.7.1 The Mössbauer Effect

An atomic nucleus can absorb a gamma ray if the energy of the gamma ray is equal to the energy difference between two states of the nucleus. This is known as resonant absorption. A nucleus can also emit a gamma ray when it undergoes a transition from a state of high excitation energy to a state of lower energy. If the nucleus is free, it will recoil when it emits the gamma ray due to the conservation of momentum, and the total energy of the gamma ray and recoiling nucleus will be equal to the energy difference of the two nuclear states. In this case the gamma ray would not have enough energy to be absorbed by another nucleus of the same type undergoing a transition between the same states, and resonant absorption would be suppressed. In 1957, Rudolf Mössbauer showed that if the emitting and absorbing nuclei are bound in lattices, the recoil energy is reduced so that resonant absorption can be observed.

Relative motion between the emitter and the absorber with velocities of the order of millimeters per second will Doppler shift the energy of the gamma ray and destroy the resonant absorption. Very small shifts in nuclear energy levels due to the environment of the nucleus can be measured by determining the relative velocity at which resonant absorption is observed. These small shifts can be explained by three phenomena: Isomer shift, quadrupole splitting, and magnetic splitting.

4.7.2 Iron-57

There are two requirements for an element to be a Mössbauer source. It must emit a low energy gamma ray and have a relatively long-lived excited state. The gamma ray emitted by the nucleus must be low in energy so as not to cause a phonon, or vibration in the lattice. Successful recoilless emission and absorption requires the whole lattice to recoil rather than a small part. Next, a long-lived excited state means a small spectral line width for the transition. The relationship between this line width and the energy of the gamma ray gives us the resolution we need to examine the miniscule change in nuclear transitions, or hyperfine interactions. Iron-57 is the most studied Mössbauer nucleus because it fits these requirements and is the fourth most abundant element in nature, catering to environmental research. It emits a low energy gamma ray of 14.4-keV and this transition has a small line width of 5x10-12-keV. From these two values we calculate a resolution of 1 part in 10 - 12 like measuring the distance from the Earth to the Moon to within the thickness of a piece of paper. Our source consists of cobalt-57 embedded in rubidium, forming the necessary crystal lattice. But, we probe with iron-57, which we gain from nuclear decay. As seen in Figure 4.13, cobalt transforms to iron by electron capture. The Mössbauer gamma ray is given off by a transition from the spin 3/2 excited state to the spin 1/2 ground state.

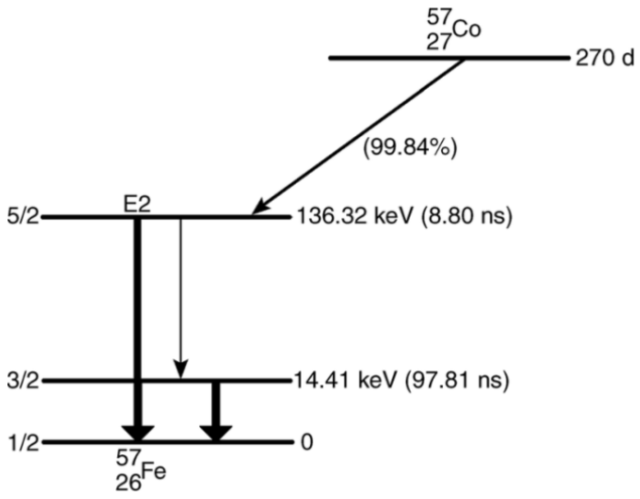

Figure 4.13: Energy level diagram showing the decay of ^{57}Co to ^{57}Fe through electron capture. We are interested in the gamma ray given off by the transition from the first excited state to the ground state of ^{57}Fe.

4.7.3 Isomer Shift

A shift in a nuclear energy level caused by a change in the interaction of the electron cloud with the nucleus is called an isomer shift. As shown in Figure 4.14, the ground and excited states shift. This shift reveals details about the bonding and shielding of iron atoms in the material.

4.7.4 Quadrupole Splitting

A nuclear quadrupole moment occurs in nuclei with non-spherical charge distributions. In the presence of an electric field gradient, or non-uniform electric field, nuclear energy levels may be split. The splitting for the first excited state in ^{57}Fe is shown in Figure 4.14. Measuring the splitting provides information about the electron configuration of iron in the material.

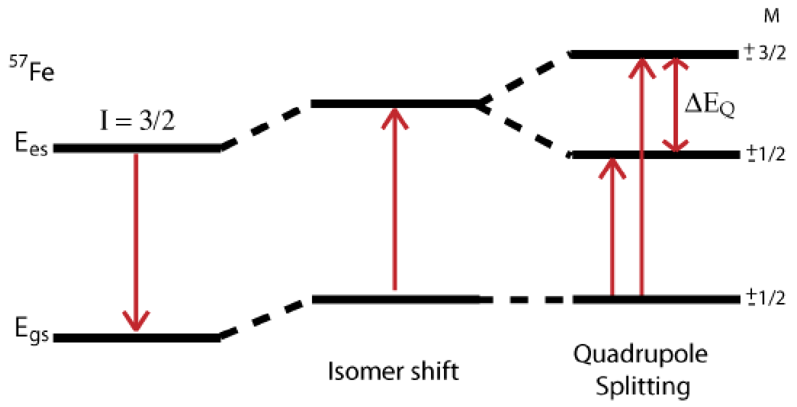

Figure 4.14: Energy level diagram showing the isomer shift and quadrupole splitting for the 3/2 to 1/2 transition in ^{57}Fe.

4.7.5 Magnetic Splitting

Magnetic splitting is caused by the interaction of the magnetic dipole moment of the nucleus with a magnetic field. This effect is illustrated for ^{57}Fe in Figure 4.15. Measurements of the magnetic splitting provide information about the magnetic properties of the material.

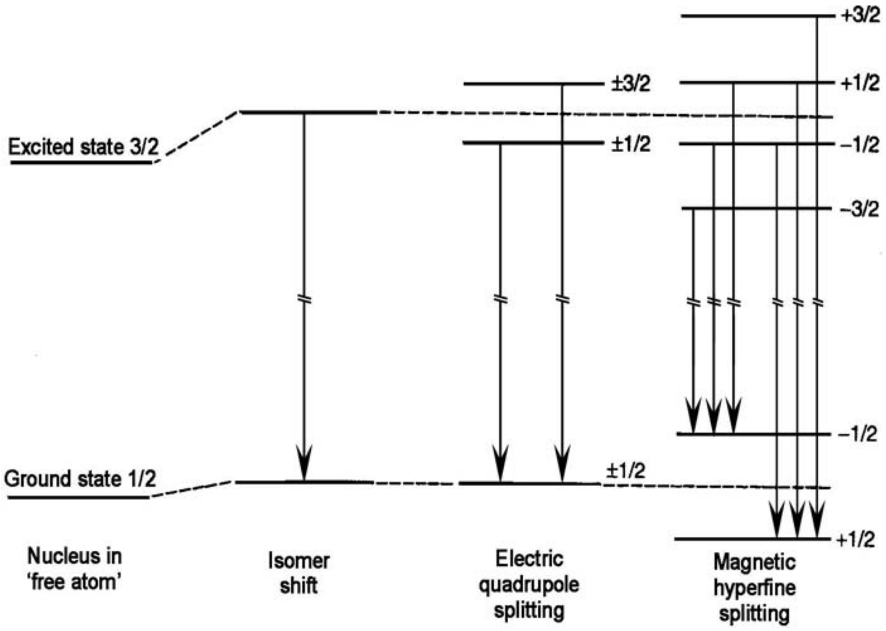

Figure 4.15: Energy level diagram illustrating magnetic splitting in ^{57}Fe.

4.7.6 Theory Behind Mössbauer Spectroscopy

Mössbauer [107] presents how to achieve the phenomenon of resonance absorption by fixing the emission source in a crystal lattice and moving it gently with respect to the absorption source. The first order approximation of the new energy E_{o} given velocity $\boldsymbol{v}$ is given by the Doppler effect:

$$E' = E_o\left(1 + \frac{v}{c}\right) \tag{4.19}$$

The natural line width of an absorption line reflects a fundamental quantum property of incoming radiation the uncertainty in the energy is tied to the uncertainty in the lifetime of the excited state through Heisenberg's relation [108]

$$\Delta E \Delta \mathrm{t} = \hbar/2 \tag{4.20}$$

The spectral line has a Lorentzian profile centered on E_0 with intensity I_0 and full-width half-maximum (FWHM) Γ

$$L(E) = \frac{I_o\left(\frac{\Gamma}{2}\right)^2}{(E - E_o)^2 + \left(\frac{\Gamma}{2}\right)^2} \tag{4.21}$$

of course, both the emission and absorption line have the above profile, with intensities I_0 and σ_0, respectively. To model the observed absorption spectrum after it has passed through an absorber of width x, we use the following equation in [109,110]. Below, A and N are the atomic weight of ^{57}Fe and N is the Avogadro's number, respectively

$$C(v) = \eta \int_0^\infty L(E) e^{-\frac{\sigma_0\left(\frac{\Gamma}{2}\right)^2 \frac{N}{A} x}{\left[E_o\left(1+\frac{v}{c}\right) - E_o - \Delta C\right]^2 + \left(\frac{\Gamma}{2}\right)^2}} \, dE \tag{4.22}$$

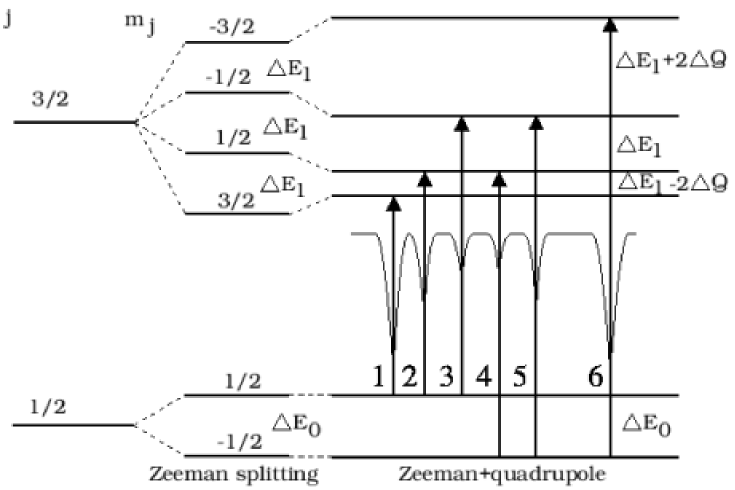

Figure 4.16: Left to right: energy level diagram of the 14.4 keV $\frac{3}{2} \rightarrow \frac{1}{2}$ ^{57}Fe transition, split by the Zeeman effect, altered by the electric quadrupole interaction [108].

4.7.7 Hyperfine Interactions

Three physical phenomena contribute to the number, location and width of observed absorption peaks. Under the influence of a magnetic field, such as that exhibited internally by iron in some compounds, Zeeman splitting of the energy levels according to total angular momentum number j occurs. Following [111], we report nuclear magnetic moments as multiples of the nuclear magneton μN. The energy shift from the original energy level E_i is, for a given angular number m_j and state i is given in [112]:

$$\Delta E(j,i) = -\mu_i B_0 = \left(\frac{g_i \mu N I}{\hbar}\right) B_0 = -g_i \mu N m_j B_0 \tag{4.23}$$

Where μ_i is the magnetic moment, expressed as a fraction Landig factor, g_i of the nuclear magneton $\mu N = 3.15 \times 10^{-12}$ eV/gauss, and B_0 is the magnetic field of the nucleus. Since m_j comes in multiples of one-half, the observed spacing between two energy levels with different m_j numbers will some integer multiple of $g_i \mu N B_0$. The quadrupole interaction is caused by an electric quadrupole moment in the atomic crystal lattice. The ground state of the atom is not affected, but the first excited state is split into sublevels that correspond to different magnitudes of m_j. Let q be the gradient of the electric potential and e^2Q the quadrupole moment. The energy shift ΔQ for the m_j ± 3/2 sublevels (the $m_j = \pm 1/2$ energy shift has the same magnitude but opposite sign) is given in [113]

$$\Delta Q = \frac{qe^2Q}{4j(2j-1)}\left[3m_j^2 - j(+j)\right] = \frac{1}{4}qe^2Q \tag{4.24}$$

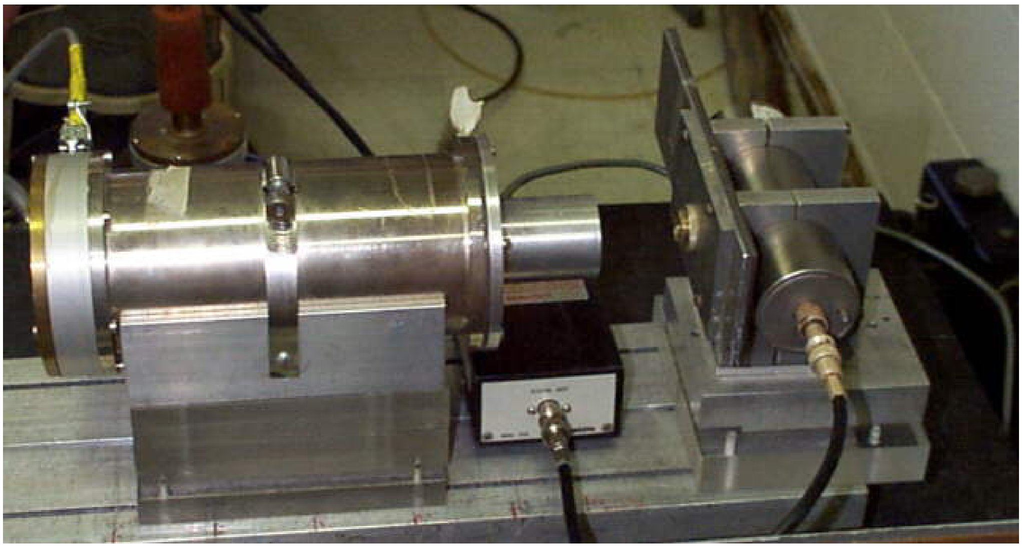

Figure 4.17: Mössbauer spectroscopy apparatus used in this study.

An energy diagram of combined quadrupole-interaction and Zeeman splitting is given in Figure 4.16. The chemical isomer shift is caused by a difference in chemical environment between source and absorber. It has the effect of shifting all energies by a small amount. A more detailed description is given in [113]. We may correlate the ultrasoft magnetic properties with volume fraction of amorphous and α-Fe(Si) soft nano composites through Mössbauer spectroscopy experiment. It also used to determine chemical shift, hyperfine field distribution (HFD) and peak width of different phases.

Chapter 5

Results and Discussion

5.1 Compositions I ($Fe_{73.5-x}Cr_xCu_1Nb_3Si_{13.5}B_9$)

5.1.1 Crystallization Phase Analysis by Differential Scanning Calorimetry

Differential scanning calorimetry (DSC) is a state-of- the-art instrument to study the crystallization kinetics of amorphous materials through which the beginning of crystallization, the temperature of primary and secondary crystallization can be discerned. Kinetics of crystallization of dissimilar crystalline phases of $Fe_{73.5-x}Cr_xCu_1Nb_3Si_{13.5}B_9$ ribbons have been evaluated by differential scanning calorimetry (DSC). Figure 5.1 of $Fe_{73.5-x}Cr_xCu_1Nb_3Si_{13.5}B_9$ alloys where x = 1, 5, 10, 12.5 and 17.5 of the amorphous ribbons show the DSC scan in nitrogen atmosphere with continuous heating at the rate of 20°C.min^{-1}. Curves show exothermic peaks in which the first one corresponds to the crystallization of α-Fe(Si) phase and the second peak stands for the formation of iron boride, Fe-B. It is observed that the crystallization of each phase has occurred over a wide range of temperature and that the peak temperature shift to higher value with the increase of Cr content. The shift of peak crystallization temperatures with increasing Cr content essentially demonstrate the thermal stability of Cr substituted alloys with increasing Cr content. Two exothermic peaks which are clearly seen corresponds to two different crystallization events as mentioned before and depicted at temperatures T_{p1} and T_{p2},

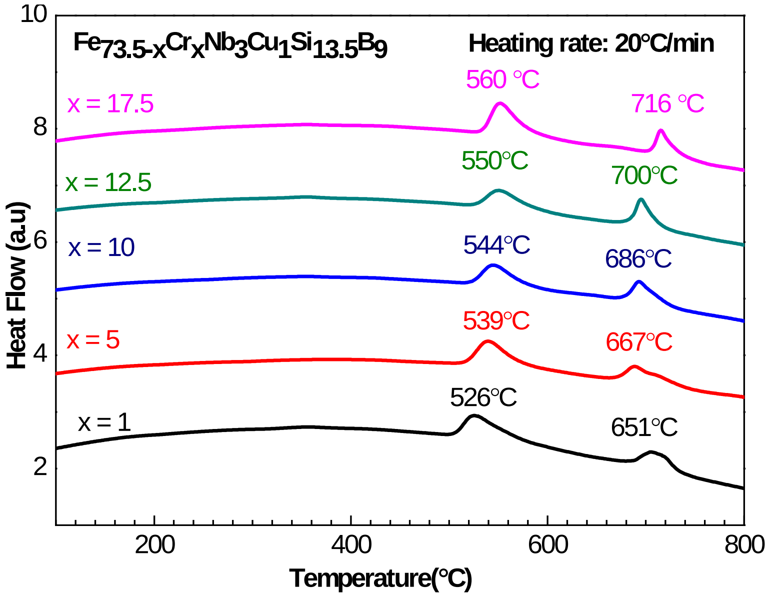

Figure 5.1: DSC thermograms of amorphous ribbons $Fe_{73.5-x}Cr_xCu_1Nb_3Si_{13.5}B_9$ alloys where x = 1, 5, 10, 12.5 and 17.5.

respectively. The initiation of crystallization phenomena begin at temperatures where exothermic heat flow just start rising. The soft magnetic properties correspond to the primary crystallization (T_{x1}) until finishing passing through the maximum peak of

Table 5.1: **P**rimary and secondary crystallization temperatures of $Fe_{73.5-x}Cr_x\ Cu_1\ Nb_3\ Si_{13.5}B_9$ for x = 1, 5, 10, 12.5 and 17.5.

Cr (x)	Heating rate /min	Primary crystallization onset temperature T_{x1} in °C	Primary peak temperature T_{p1} in °C	Secondary crystallization onset temperature T_{x2} in °C	Secondary peak temperature T_{p2} in °C
1	20°C	494	526	640	651
5		509	539	652	667
10		514	544	667	686
12.5		517	550	675	700
17.5		524	560	698	716

α-Fe(Si) nanograin formation and that of a secondary crystallization (T_{x2}) corresponds to Fe-B phase that impart magnetic hardening to the nanocrystalline alloy. The primary and secondary crystallization onset temperatures (T_{x1} and T_{x2}) and peak temperatures (Tp_1 and Tp_2) exhibit exothermic peak *i.e.* exhaust heat for the duration of the crystallization of Fe (Si) and Fe-B phases.

The minimum amount of energy is required to bring the reactant in such a state of a chemical reaction that they may undergo a chemical transformation is termed as activation energy. According to the transition-state theory, the activation energy represent the difference of energy configuration between the energy activated or transition state and the initial state of the reactant. For initiate a reaction at a countable rate it is required that an appreciable number of reactant should have energy equal or greater than the activation energy [114]. Several effective methods have been developed for the calculation of activation energy. Among them the Arrhenius plot of Kissinger's equation (see equation 5.1 in section 5.2 for details) is one of the popular methods to calculate activation energy of crystallization of α-Fe (Si) and Fe-B [115]. We have avoided presenting activation energy data for the sample $Fe_{73.5-x}Cr_xCu_1Nb_3Si_{13.5}B_9$ which are already available in the literature. It is found in the reference [116] that the authors have obtained the primary and secondary activation energy of crystallization are E_1 = 3.18eV and E_2 = 4.62eV respectively for Cr concentration x = 3 from the slop of the Kissinger plot of DSC data. The large difference in the activation energy between primary and secondary crystallization clearly demonstrates that the thermal stability of these alloys strongly influenced by the addition of Cr content.

5.1.2 X-ray Diffraction Analysis of $Fe_{73.5-x}Cr_xNb_3Cu_1Si_{13.5}B_9$

The $Fe_{73.5-x}Cr_xNb_3Cu_1Si_{13.5}B_9$ (x = 1, 5, 10, 12.5 and 17.5) alloys synthesized for the study were found to be amorphous which have already been displayed in Figure 3.5(a). It is observed from the Figure 3.5(a) that all the samples of the series show humps at around $2\theta = 45^{o}$ extended up to 10^{o}. These diffused extended humps clearly demonstrates the amorphous nature of all the as cast samples.

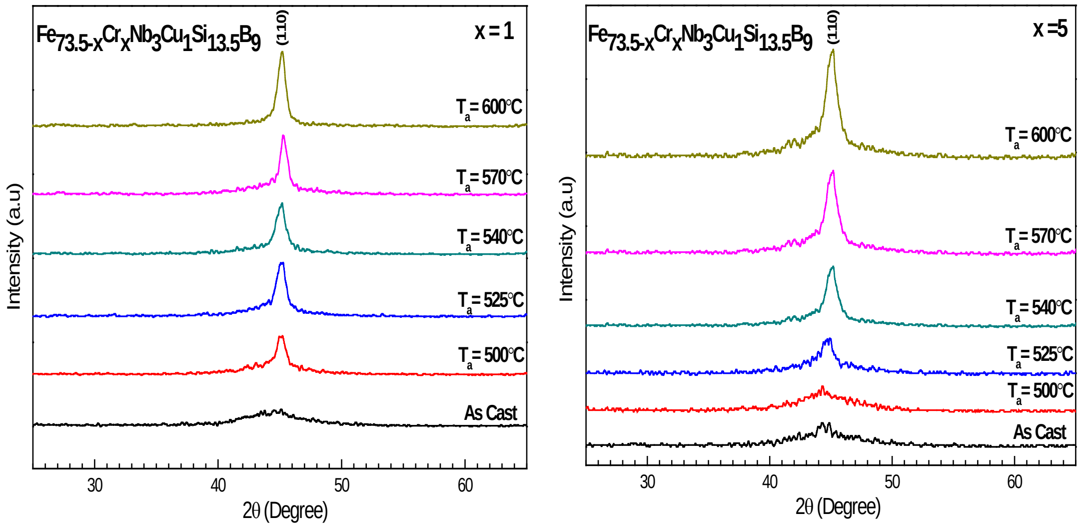

(a) (b)

Figure 5.2: XRD pattern at different annealing temperature of $Fe_{73.5-x}Cr_xNb_3Cu_1Si_{13.5}B_9$ alloys for (a) x = 1 and (b) x = 5.

Figure 5.2 depicts the XRD patterns of x = 1 sample annealed at different temperature based on the results of DSC thermogram. It is seen that as cast sample is amorphous while other samples annealed between 500~600°C show different degree of crystallization. As the temperature of annealing, T_a increases, the sharpness and intensity of the XRD pattern increases along with the narrowing of pattern. This indicates that the nanograins have started to grow and becoming larger with increasing T_a. It is also observed that crystallization has already initiated at temperature as low as 500°C, while from DSC it is seen that the crystallization peak temperature for sample x = 1, is 526°C and onset of crystallization temperature would be around 500°C. This means that crystallization of the sample starts much before the peak temperature, T_{p1} near the temperature of onset of primary crystallization at $T_{x1} \approx$ 594°C as seen in DSC thermogram and the XRD data presented in Table 5.1 and Figure 5.2 are quite comparable with DSC data.

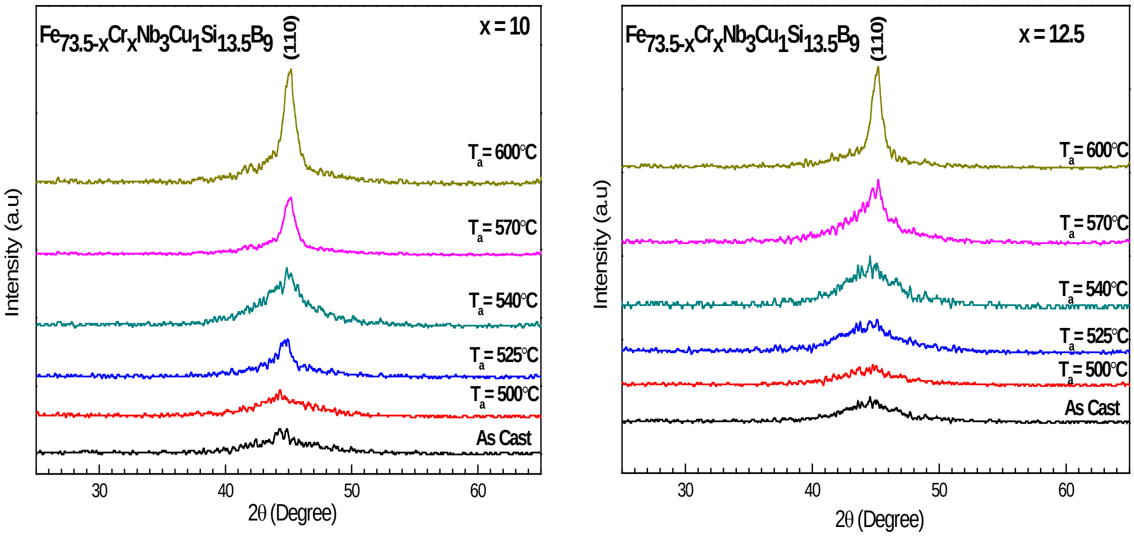

(a) (b)

Figure 5.3: XRD pattern at different annealing temperature of $Fe_{73.5-x}Cr_x Nb_3Cu_1Si_{13.5}B_9$ alloys for (a) x = 10 and (b) x = 12.5.

The crystallization is well matured at T_a = 540°C and above as clearly depicted in XRD pattern in Figure 5.2. It observed in Figure 5.2(b), Figure 5.3(a) ,(b) and Figure 5.4 from XRD pattern for samples with higher Cr content *i.e.* x = 5, 10, 12.5 and 17.5 the crystallization begins to develop gradually at temperature lower than peak temperature, T_{p1} and become mature at higher annealing temperature T_a. In all these XRD patterns it is evident that onset of crystallization event is delayed with increasing Cr content. With the increase of annealing temperature, T_a the peak area shrinks, becomes sharper indicating the growth of nanograins. For the samples with x = 12.5 and 17.5, the crystallization phenomenon become very sluggish and negligible until T_a = 570°C. This demonstrates the thermal stability of higher Cr content that inhibits the crystallization process. It is quite noticeable that sample with x = 17.5 at temperature as high as T_a = 600°C, crystallization process has not been completed perfectly as seen from its diffuseness of the peak. Analysis of the peaks revealed that it corresponds to *bcc* α-Fe (Si) phase.

.

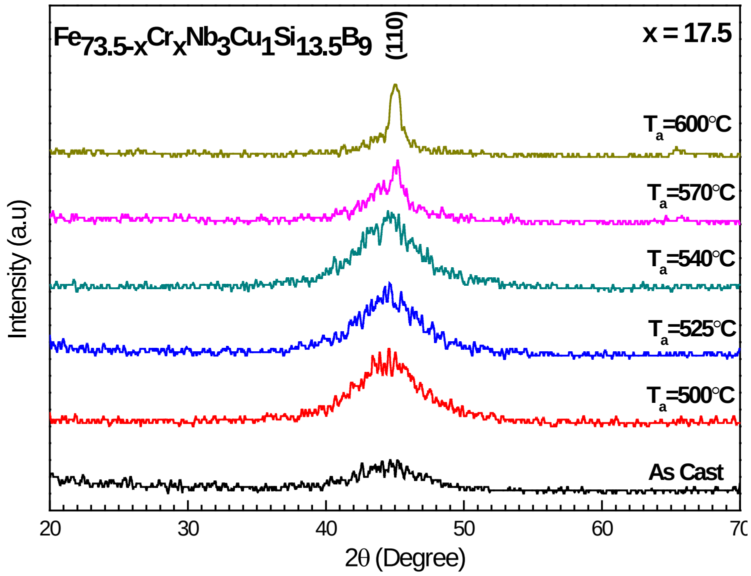

Figure 5.4: XRD pattern of $Fe_{73.5-x}Cr_xNb_3Cu_1Si_{13.5}B_9$ alloy annealed at different temperatures, where x = 17.5.

The grain size determined by using the Scherrer's formula [84],

$$D_g = \frac{0.9\lambda}{\beta\cos\theta}$$

where, $\lambda = 1.54178$ Å for Cu-K$_\alpha$ radiation and $\beta = FWHM$ (full width at half maximum) at different annealing temperature, T_a is presented in Table 5.2. It can be observed that grain size vary significantly with annealing temperature for all the studied samples. From Table 5.2 it is clearly seen that the increasing of Cr content in FINEMET alloy, the grain sizes are found to decrease significantly and the increasing in annealing temperature has contributed substantially to increase the grain growth.

For higher Cr content sample crystallization is delayed resulting in smaller grain sizes.

Table 5.2: Grain size estimated from the XRD data of crystalline $Fe_{73.5-x}Cr_xNb_3Cu_1Si_{13.5}B_9$ alloys with different Cr content and annealing temperature.

Content Cr(x)	Annealing temperature, T_a (°C)	Crystalline Phase	Grain size (nm)
1	As cast	Amorphous	-
	500	α-Fe(Si)	10
	525	α-Fe(Si)	12
	540	α-Fe(Si)	15
	570	α-Fe(Si)	17
	600	α-Fe(Si)	20
5	As cast	Amorphous	-
	500	Amorphous	-
	525	α-Fe(Si)	4
	540	α-Fe(Si)	11
	570	α-Fe(Si)	13
	600	α-Fe(Si)	18
10	As cast	Amorphous	-
	500	Amorphous	-
	525	Amorphous	-
	540	α-Fe(Si)	4
	570	α-Fe(Si)	12
	600	α-Fe(Si)	18
12.5	As cast	Amorphous	-
	500	Amorphous	-
	525	Amorphous	-
	540	Amorphous	-
	570	α-Fe(Si)	6
	600	α-Fe(Si)	15
17.5	As cast	Amorphous	-
	500	Amorphous	-
	525	Amorphous	-
	540	Amorphous	-
	570	α-Fe(Si)	4
	600	α-Fe(Si)	14

For samples having Cr content x = 1 grain size become 10 nm at T_a = 500°C while it is 11 nm for sample x = 5 at T_a = 540°C. But for samples with x = 12.5 and 17.5, no grains are detected even at T_a = 540°C implying that thermal energy required to trigger crystallization event is insufficient at this temperature. Well defined crystallization is only observed at T_a = 600°C from XRD pattern indicating the grain growth inhibiting nature and thermal stability of Cr addition. For higher Cr content sample XRD pattern are not well developed for which grain size calculation using Scherrer's formula is an approximation [84]. Due to large amount of refractory Cr metal present in the sample intrinsic crystallization behavior of the amorphous precursor in the form of ribbon is heavily jeopardized resulting in heterogeneous crystallization. The maximum grain sizes attained after the annealing treatment at T_a = 600°C are 18-20 nm for low Cr content samples and 14-15 nm for higher Cr content as clearly depicted in Table 5.2. For sample with x = 12.5 and 17.5 it is seen from the XRD pattern that the initiation of crystallization starts visible only at T_a = 570°C but still diffused and slightly matures at T_a = 600°C. Thus the role of Cr in the crystallization of $Fe_{73.5-x}Cr_xCu_1\ Nb_3Si_{13.5}B_9$ amorphous alloy system subjected to thermal treatment around the primary crystallization temperature is clearly understood from a detail study of XRD spectrum.

5.1.3 Microstructural study of $Fe_{73.5-x}Cr_xNb_3Cu_1Si_{13.5}B_9$ by FESEM

Field Emission Scanning Electron Microscopy (FESEM) is a useful technique for microstructural study. The white line in the micrograph scale stands for 100 nm.

Figure 5.5(a) - (d) shows the microstructure developed after heat treatment of the sample Cr = 1 at T_a = 480, 520 and 550°C along with the as cast sample. As cast sample (Figure 5.5(a)) does not show any sign of crystallization with clear background. All other as cast samples demonstrate similar behavior. As the annealing temperature increases crystallization event starts develop. In Figure 5.5(b) at T_a = 480°C, for sample x = 1 no grains are detected but a cluster like agglomerate is clearly visible which may be considered as the stage just before the initiation of crystallization. Figure 5.5 (c) shows the microstructure of the annealed sample at T_a =

520^{o}C. Here crystallization has already started and nanograins have developed. But they are far apart from each other and are agglomerated while sample annealed at T_a = 550^{o}C shows complete crystallization. Large numbers of closely spaced nanograins have grown but still they are agglomerated. The grain size estimated from the microstructure appears to be much larger than that of calculated from the XRD data and tabulated in Table 5.2

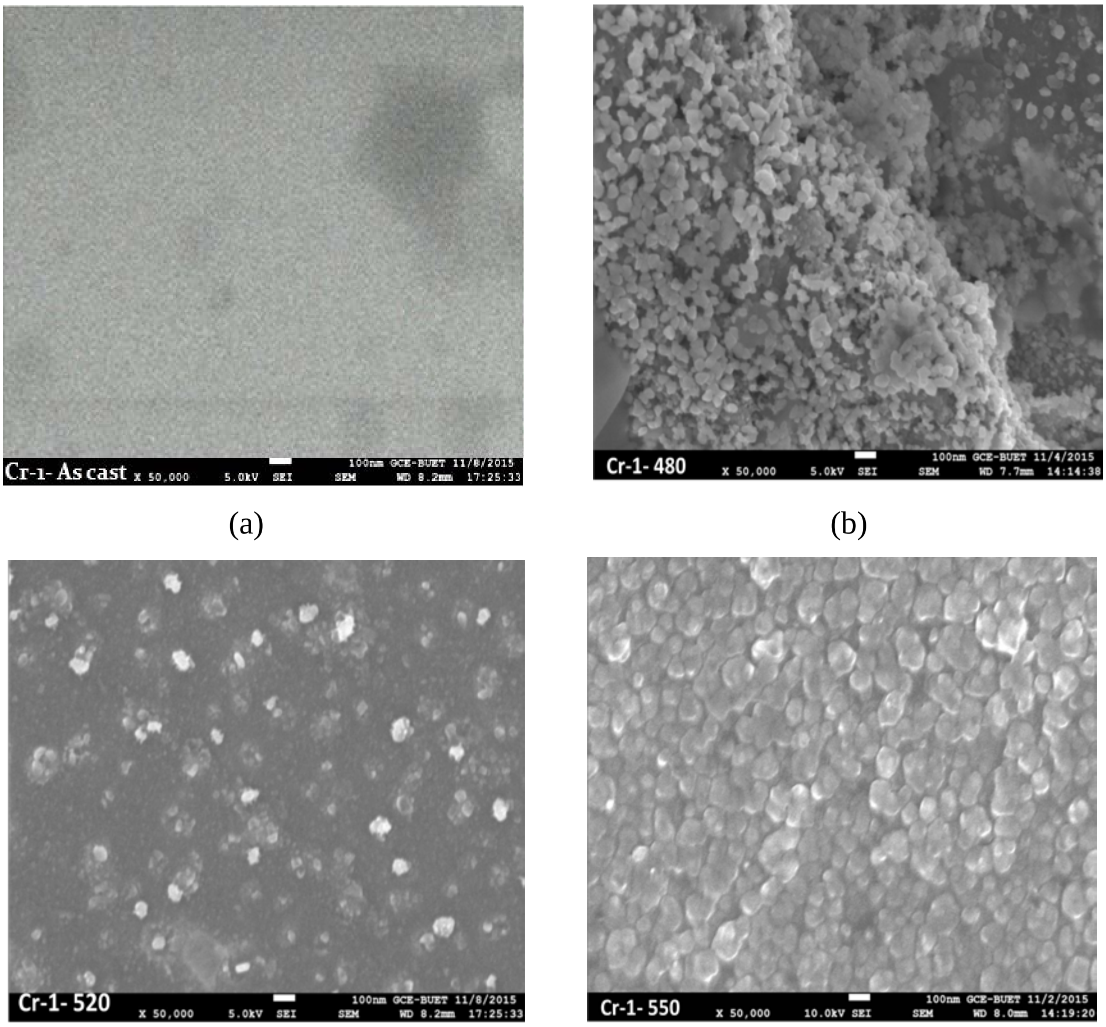

(a) (b)

(c) (d)

Figure 5.5: FESEM microstructure of $Fe_{73.5-x}Cr_xNb_3Cu_1Si_{13.5}B_9$ where x = 1 (a) as cast and annealed at temperatures (b) 480^{o}C, (c) 520^{o}C and (d) 550^{o}C.

Generally grain sizes observed from the SEM images are larger due to light scattering and shadow effect including the agglomeration tendency of nanometric size grain due to reduction of surface energy [117]. XRD spectrometry is much better technique for the determination of nanograin size less than 50 nm. Inspite of that careful and critical observation of the microstructure will reveal that the grains are less than 25 nm. Similar is the case with other sample having higher Cr content [118].

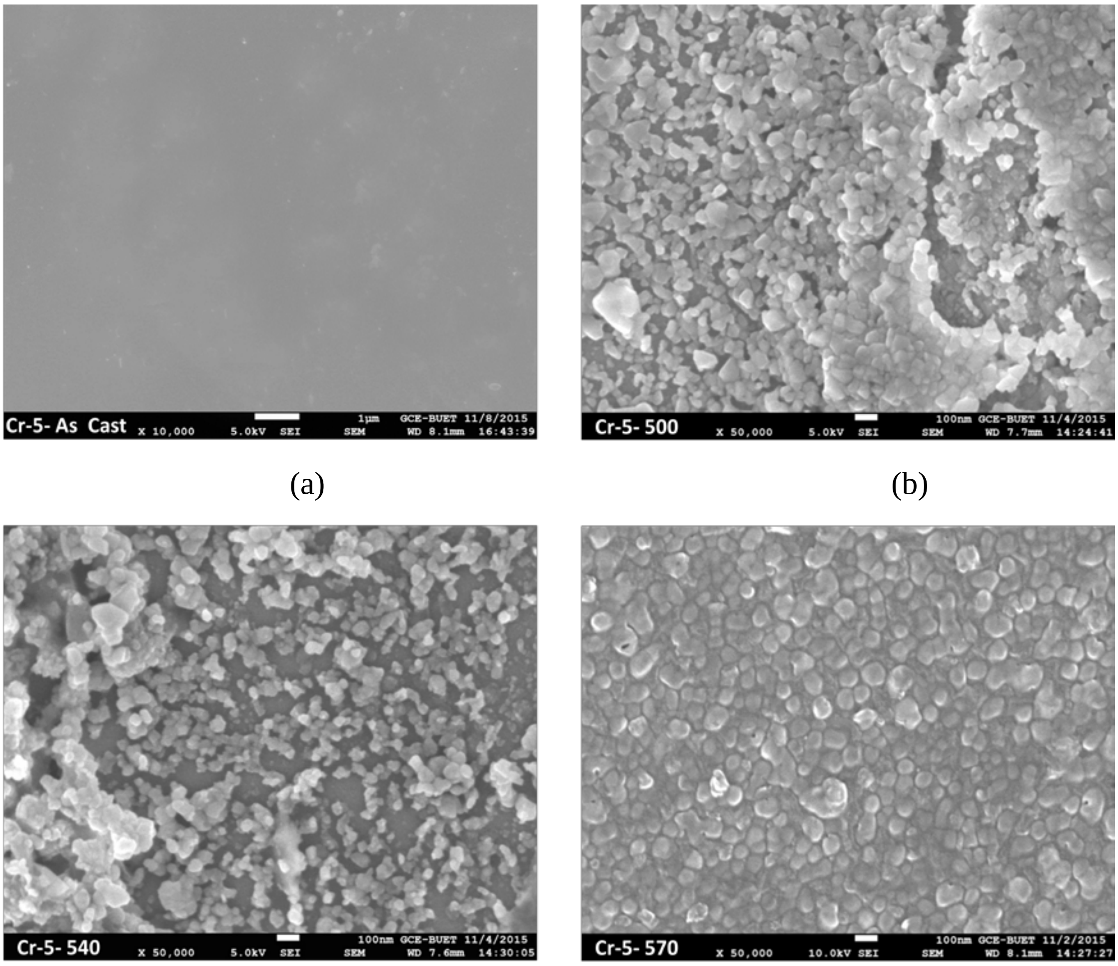

(a) (b)

(c) (d)

Figure 5.6: FESEM microstructure of $Fe_{73.5-x}Cr_xNb_3Cu_1Si_{13.5}B_9$ where x = 5 at (a) as cast and annealed at temperatures (b) 500^{o}C, (c) 540^{o}C and (d) 570^{o}C.

All the samples understudy show crystallization event at annealing temperature which is around the primary crystallization peak temperature T_{p1} determined from DSC thermogram where well defined nanograins are observed. The result of DSC, XRD and FESEM are quite comparable. Figure 5.6(a) – (d) shows the microstructure of the sample with x = 5 in as cast and annealed at T_a = 500, 540, and 570^{o}C.

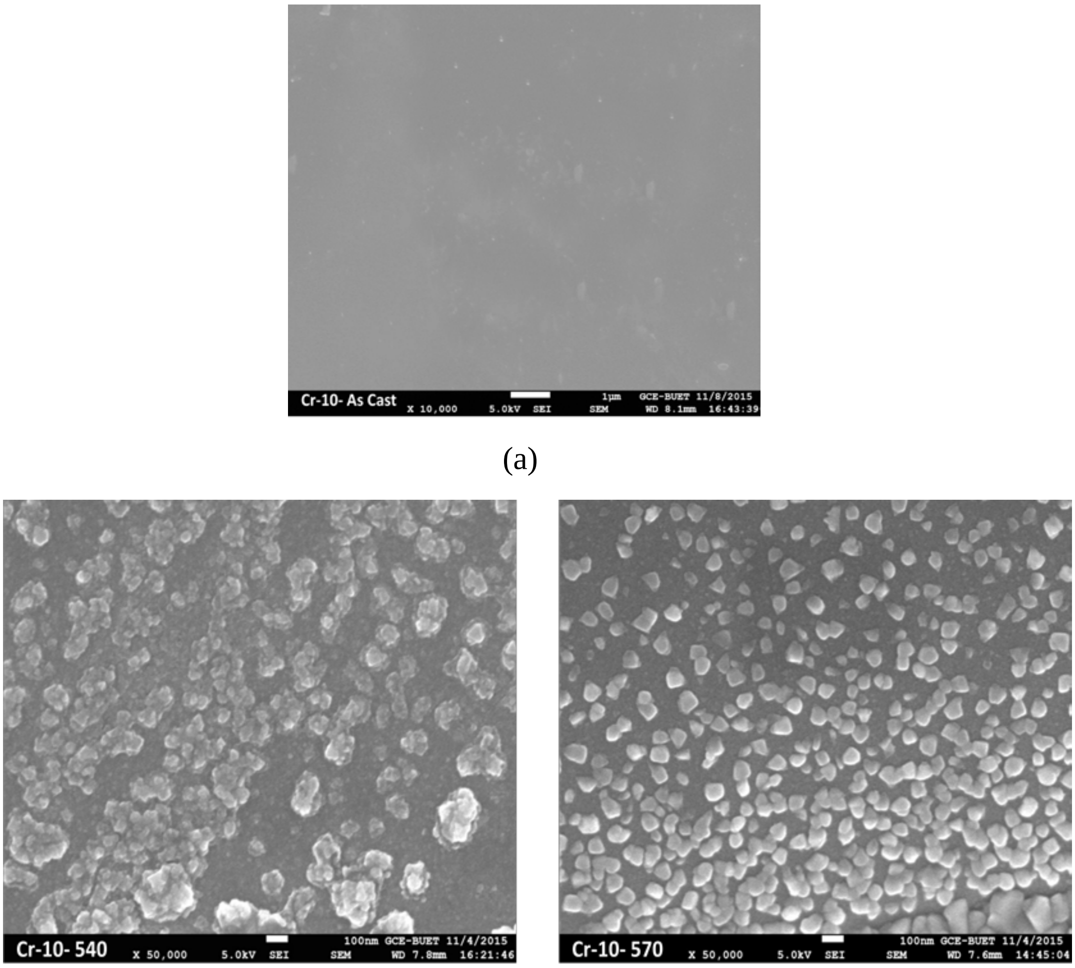

(a)

(b) (c)

Figure 5.7: FESEM microstructure of $Fe_{73.5-x}Cr_xNb_3Cu_1Si_{13.5}B_9$ where x = 10 (a) as cast and annealed at temperatures (b) 540^{o}C, and (c) 570^{o}C.

In Figure 5.7 it is observed that crystallization has started at T_a = 540^{o}C with highly agglomerated grains which are far apart from each other and it is difficult to determine their sizes. At T_a = 570^{o}C, crystallization is well matured having grain sizes less than 25nm. Because of agglomeration actual grain size cannot be observed. XRD analysis revealed the grain size of the sample x = 10, as 4 nm and 12 nm for T_a = 540 and 570^{o}C respectively. The peak crystallization temperature T_{p1} for the sample is T_{p1} = 544^{o}C and crystallization onset temperature T_{x1} = 514^{o}C based on DSC data as seen in Table 5.1. The results of FESEM, DSC and XRD are found to be quite compatible.

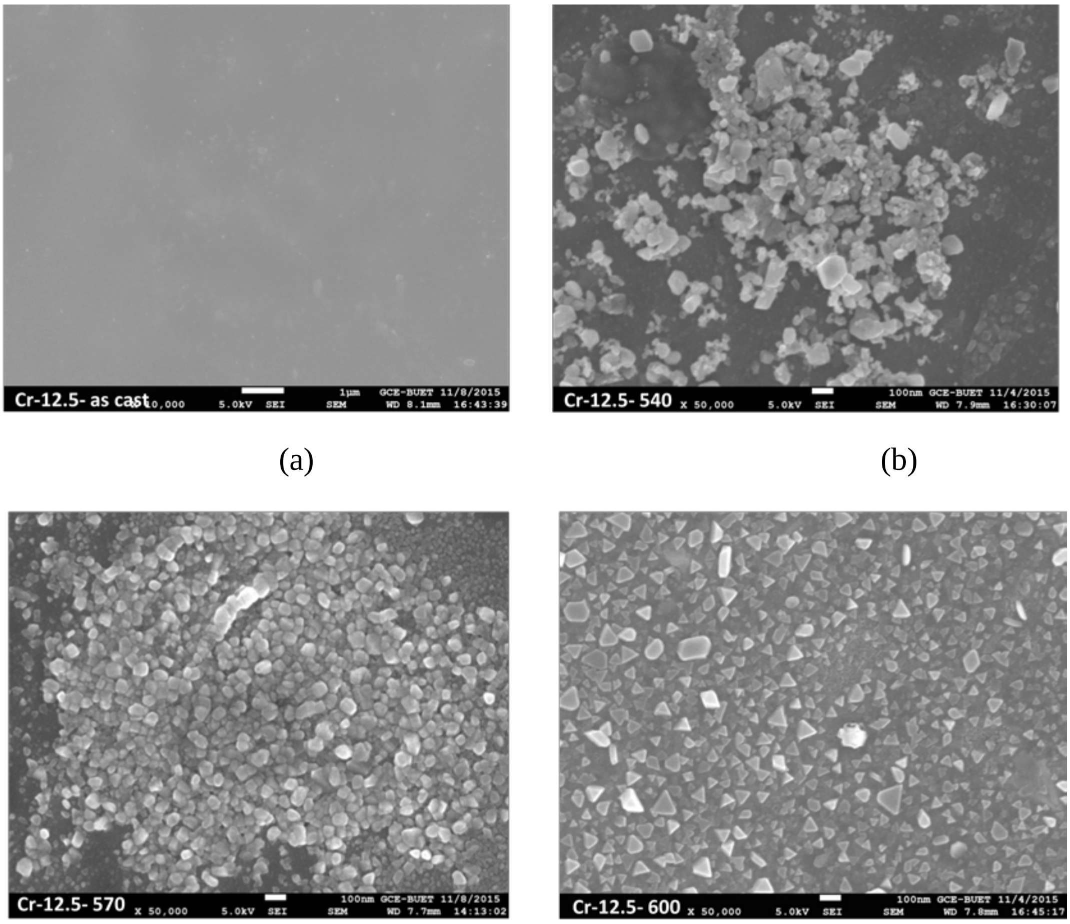

(a) (b)

(c) (d)

Figure 5.8: FESEM microstructure of $Fe_{73.5-x}Cr_xNb_3Cu_1Si_{13.5}B_9$ where x = 12.5 (a) as cast and annealed at temperatures (b) 540^{o}C, (c) 570^{o}C and (d) 600^{o}C.

Figure 5.8 (b), (c), (d) shows the microstructure development when annealed at T_a = 540, 570 and 600^{o}C for the sample with Cr = 12.5. It is seen from the SEM image that initiation of crystallization has taken place at T_a = 540^{o}C comparable with DSC data of T_{x1} = 517 and T_{p1} = 550^{o}C. At T_a = 570^{o}C agglomerated grains are clearly visible with low nanometer sizes while matured nanometric grains are demonstrated at T_a = 600^{o}C. The results are comparable with XRD data as depicted in Table 5.2. The result of microstructure of the sample with Cr = 17.5 done by FESEM is displayed in Figure 5.9 annealed at T_a equal to 570, 600 and 650^{o}C. The sample annealed at T_a = 570^{o}C shows unique nanograins (see Figure 5.9(b)) having grain size lower than 10 nm corresponding to 4 nm determined from XRD spectrum.

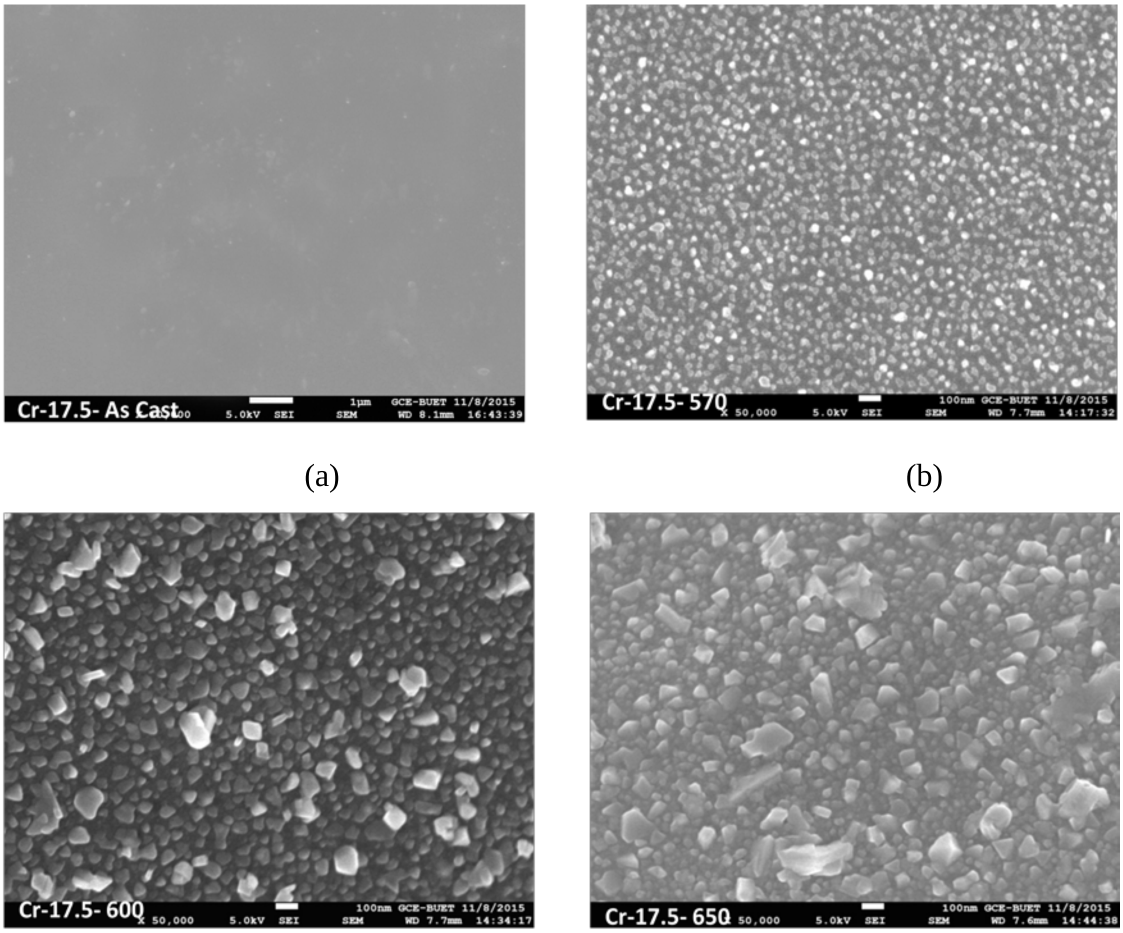

(a) (b)

(c) (d)

Figure 5.9: FESEM microstructure of $Fe_{73.5-x}Cr_xNb_3Cu_1Si_{13.5}B_9$, where, x = 17.5 (a) as cast and annealed at temperatures (b) 570°C, (c) 600°C and (d) 650°C.

The microstructure has matured with much larger grains size for samples annealed at T_a = 600°C as displayed in Figure 5.9(c). The size of the grains reasonably matches well with the data calculated from XRD spectrum and found to be around 14 nm. From the microstructural study done by FESEM it is clearly demonstrated that crystallization behavior of $Fe_{73.5-x}Cr_xCu_1Nb_3Si_{13.5}B_9$ amorphous alloys in the form of ribbons of 25µm thickness is strongly dependent on Cr concentration and temperature of thermal treatment. Higher the Cr content, difficult is the crystallization event to take place, which means that Cr has the effect of thermal stability against crystallization. With increasing Cr content growth of nanograins are inhibited which have been reflected well through the experiment. As Cr content increases in the alloy system grain size decreases while annealed at the same temperature. This is clearly reflected in the result of XRD data (Table 5.2) and microstructural images taken for the samples with varying Cr content and annealed at different temperatures.

5.1.4 Saturation Magnetization

Saturation magnetization, M_s, a basic parameter of magnetic materials, has been calculated using a vibrating sample magnetometer (VSM) data calibrated with a standard Ni sample. Figure 5.10 shows the *M* -*H* hysteresis loop measured at room temperature (*RT*) in as cast and annealed condition annealed at T_a = 500 and 600°C. It is evident from the curves that the magnetization is saturated for the studied samples with x = 1, 5 and 10 measured at room temperature. While the sample with x >10 do not show any sign of saturation with applied field up to H_a = 20000 Oe in as cast condition. This *M-H* curve typically shows the sign of paramagnet. This means that samples with x ≤ 10 are ferromagnets and x >10 are paramagnet at room temperature without any thermal treatment.

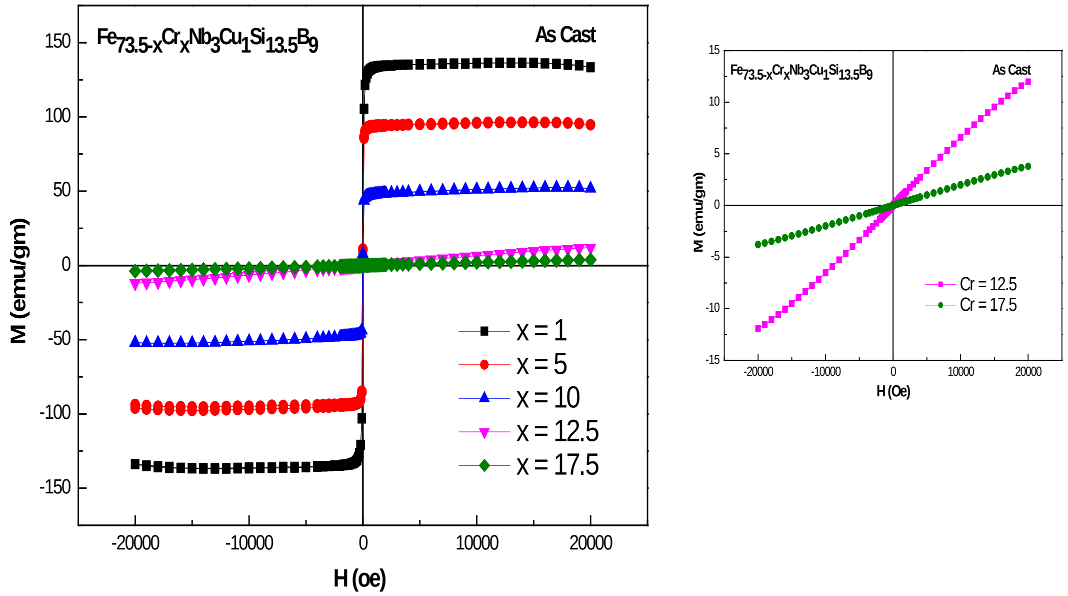

Figure 5.10: M-H curve of $Fe_{73.5-x}Cr_xNb_3Cu_1Si_{13.5}B_9$ for as cast sample at room temperature. Figure at right shows the magnified view near the origin for Cr content x = 12.5 and 17.5.

)

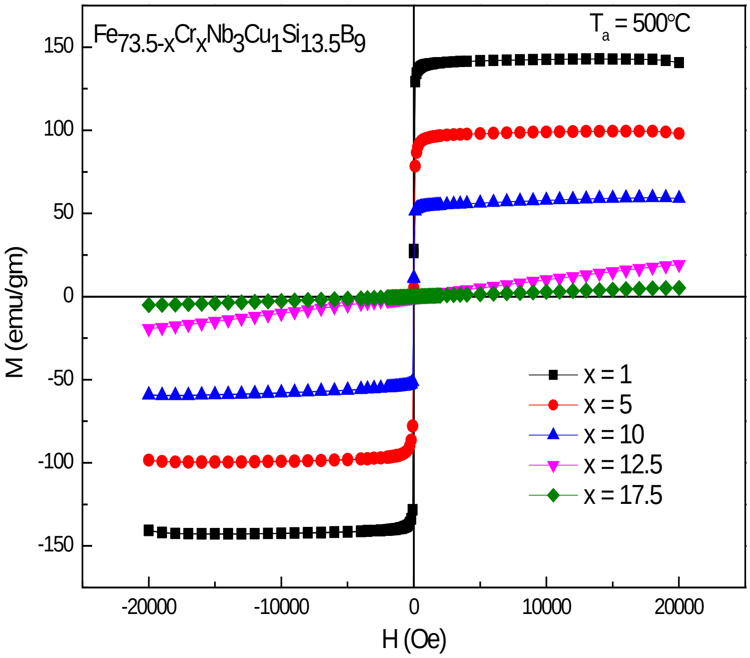

Figure 5.11: M-H curve of $Fe_{73.5\text{-}x}Cr_xNb_3Cu_1Si_{13.5}B_9$ at RT annealed at 500°C.

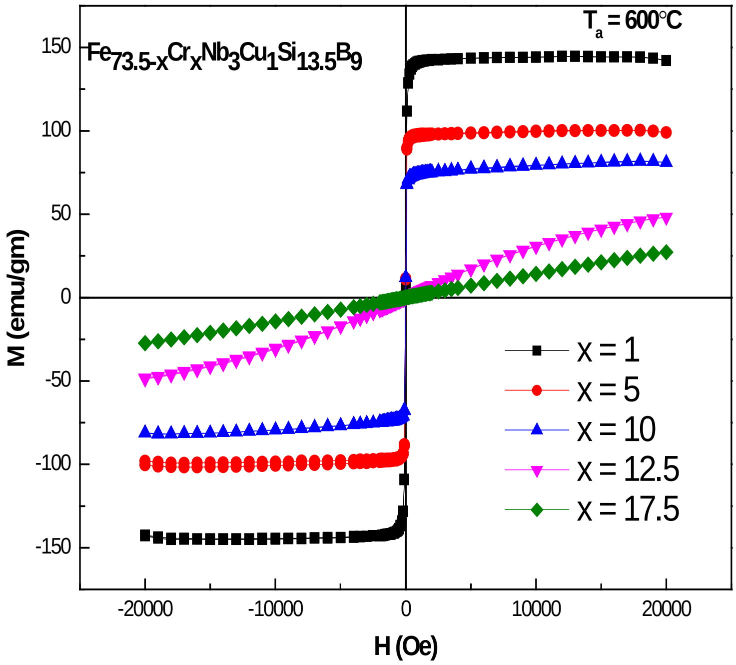

Figure 5.12: M-H curve of $Fe_{73.5\text{-}x}Cr_xNb_3Cu_1Si_{13.5}B_9$ at RT annealed at 600°C.

All the magnetization, M_s value of these sample are tabulated in Table 5.3. It is observed that as the Cr content increase, the magnetization value gradually decreases in as cast and annealed condition. The coercivity, H_C is quite negligible. The decrease of magnetization

Table 5.3: Saturation magnetization, M_s in emu/gm at room temperature for as cast and annealed at different temperature (T_a).

Cr x (at%)	M_s (emu/gm) at RT as cast	M_s (emu/gm) at RT $T_a = 500^oC$	M_s (emu/gm) at RT $T_a = 600^oC$
1	134	141	143.4
5	96	98.5	100.3
10	52	59.3	81.5
12.5	12.1	19.3	48.7
17.5	3.8	5.2	27.4

resulting from non-magnetic Cr substitution is obviously due to the simple dilution of magnetic matrix. But slight increase of M_s due to annealing at $T_a = 500$ and 600^oC is due to relaxation effect, decrease of stress, slight increase of density, decrease of porosity for $T_a = 500^oC$, while for $T_a = 600^oC$, it is due to crystallization of Fe-(Si) nanograins having high magnetization and strong magnetic coupling between the nanograins. As the porosity and mechanical stress decreased as a result of annealing, the magnetization is increased. Because of the small coercive field of the FINEMET alloy, particular concentration was paid to the demagnetizing process of the samples. These hysteresis loops also demonstrate the good excellence of our quasi-static measurements. By determining the soft magnetic properties for samples annealed around the optimal conditions, it is seen that the characteristics of magnetic softness (H_C and μ_0) are about 5-10 times better for Fe-Si-B based alloys compared to the FeZrB based ones [5] although the latter have the advantage of having a saturation magnetization of about 25-45% higher than the first one. Concerning the conditions for magnetic softness, the magnetostriction measurements at room temperatures on nanocrystalline alloys [6] have confirmed a close to zero magnetostriction for both alloys near to the optimum annealing [7].

Most interesting and noticeable thing in this table is that M has increased substantially on annealing at T_a = 600^{o}C particularly for samples with x > 10. An increase of magnetization (M) is clearly evident from 3.8 emu/gm in as cast condition to 27.4 emu/gm annealed at T_a = 600^{o}C for sample x = 17.5 and from 12.1 emu/gm to 48.7 emu/gm for sample x = 12.5 annealed at the same temperature T_a = 600^{o}C. This radical increase of magnetization is the result of crystallization of magnetic nanograins of Fe-(Si) phase. This unique phenomena of growth of magnetic nanograins having high saturation magnetization is the root of being FINEMET alloys are very important from the technological point of view. To make these alloys technically potential detail crystallization behavior from the prepared amorphous state necessitates extensive research from amorphous matrix which otherwise display paramagnetic characteristics with very low magnetization value. The changes in magnetization as affected by annealing at T_a = 500 and 600°C for various Cr concentration of the studied alloys compared with as cast sample in amorphous state are shown in Table 5.3.

5.1.5 Measurement of Permeability

5.1.5.1 Frequency Dependent Permeability

Permeability is an important parameter for any magnetic material from the engineering application point of view. For an AC application frequency depended of real part of permeability clearly demonstrates its practical application range up to which the device made from the material can be fruitfully utilized. The landmark for its application on frequency dependence is limited by the resonance frequency where the real part of permeability, μ' starts decreasing very rapidly while the imaginary part, μ'' which corresponds to magnetic loss component or loss tangent, $\tan\delta = \mu''/\mu'$, rises to very high value attaining μ''max or tan$\delta = \mu''/\mu'$= maximum . The complex permeability related as $\mu = \mu' - i\mu''$ according to equation (2.32). The real part of permeability strongly depends on the density, number of pores, non-magnetic phase, crystal anisotropy and magnetic anisotropy [118]. For the demagnetizing field, the permeability is related to the shape of the particles. It is large for needles and small for flakes [119]. These parameters can make an impression on wall dislocation and spin rotation. For example, the incidence of a nonmagnetic material between the magnetic components acts likewise to an air gap, as a source of demagnetizing field. The pores act as pinning sites for the domain wall motion. As a result, domain wall movement is restricted and this limits the rate of growth of real part of permeability.

Figure 5.13 and 5.14 show the real part of permeability as a function of frequency for the annealed samples at T_a = 500 and 550°C. As the Cr content increases the permeability decreases resulting from the lower magnetization value as a function of Cr concentration. The annealing temperature dependence on permeability are depicted in the Figure 5.13 and 5.14 where the value of permeability is strongly affected by the annealing temperature and relatively low value at lower annealing temperature [120]. The annealing temperatures of the samples were T_a = 500 and 550^{o}C respectively.

It is observed that a two fold increase of permeability is attained when annealed at T_a = 550^{o}C compared with T_a = 500^{o}C as seen in Figure 5.13 and Figure 5.14. Generally all FINEMENT alloys including Fe-Si-B show permeability values of 300 to 400 in the amorphous samples. A sharp increase of permeability on annealing is clearly observed which may be attributed to the crystallization of Fe-(Si) nanograins, strong exchange coupling between the α-Fe(Si) magnetic nanograins through the residual amorphous matrix due to increasing volume fraction of Fe(Si) nanograins. It is observed from the Figure 5.13 and Figure 5.14 that μ' gradually decrease with increase of frequency which may be attributed to the increase of hysteresis and anomalous loss resulting from difficulty of spin rotation and domain wall motion and magnetization reversal which can no longer follow the applied AC field.

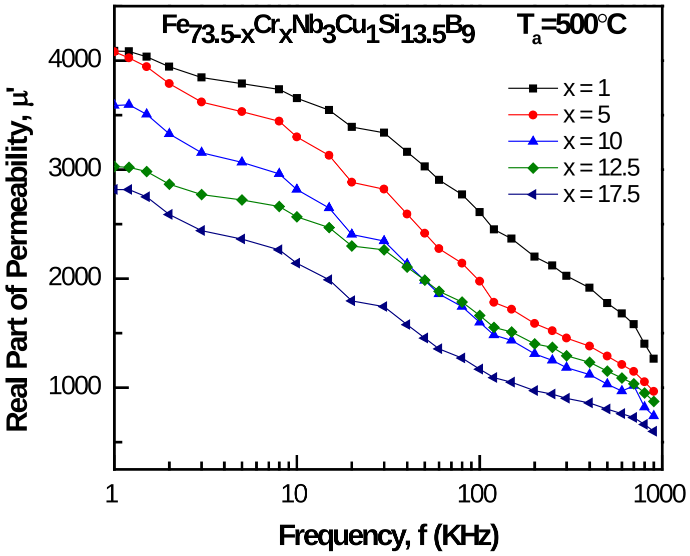

Figure 5.13: Real part of the permeability at room temperature as a function of frequency for $Fe_{73.5-x}Cr_xNb_3Cu_1Si_{13.5}B_9$ alloys annealed at T_a = 500°C.

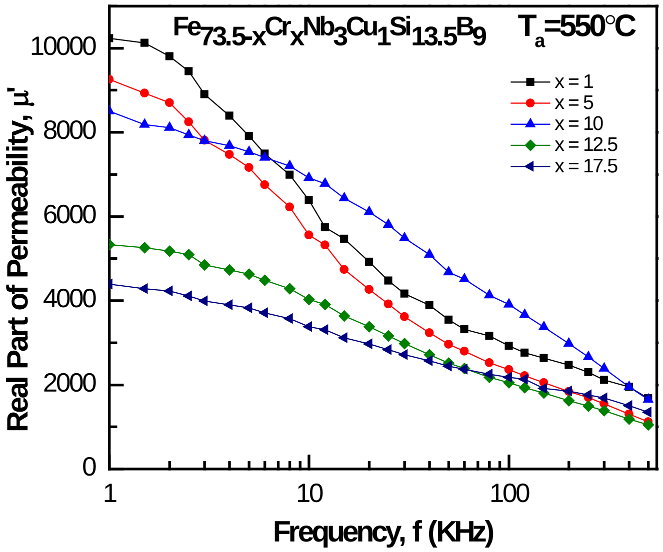

Figure 5.14: Real part of the permeability at room temperature as a function of frequency for $Fe_{73.5-x}Cr_xNb_3Cu_1Si_{13.5}B_9$ alloys annealed at T_a = 550°C.

5.1.5.2 Imaginary Part of Permeability

Figure 5.15 and 5.16 show the frequency spectra of imaginary μ'' part of the complex permeability of the toroid shape cores prepared from different composition with x = 1, 5, 10, 12.5 and 17.5.

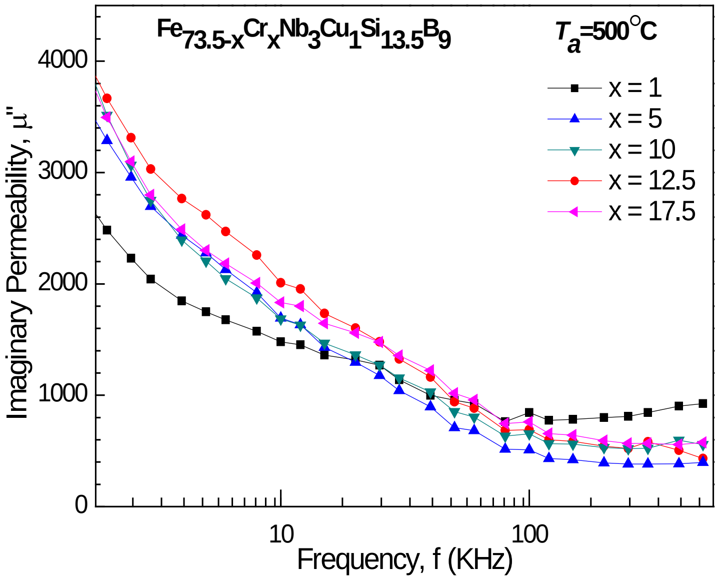

Figure 5.15: Frequency dependent imaginary part of permeability at room temperature for $Fe_{73.5-x}Cr_xNb_3\ Cu_1Si_{13.5}B_9$ alloys annealed at T_a = 500°C.

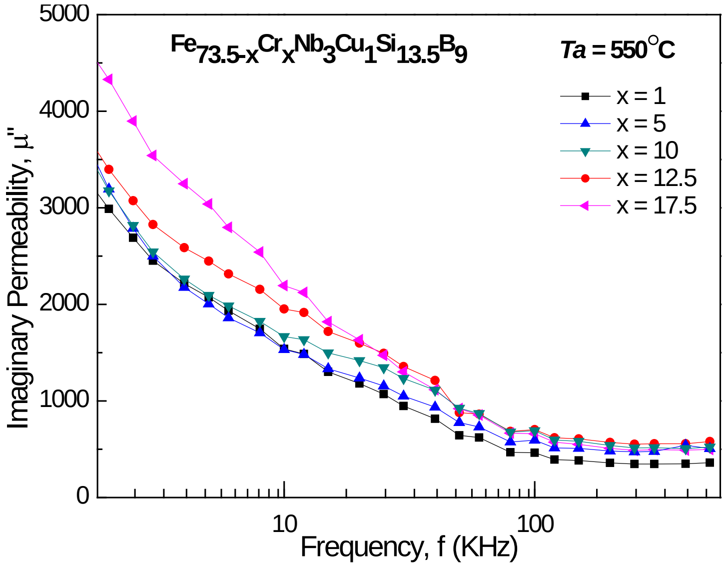

Figure 5.16: Frequency dependent imaginary part of permeability at room temperature for $Fe_{73.5-x}Cr_xNb_3\ Cu_1Si_{13.5}B_9$ alloys annealed at T_a = 550°C.

It can be seen that imaginary part of permeability μ'' of the sample decrease sharply at low frequency region and sluggishly at higher frequency region. Imaginary part of the complex permeability reflects the power loss due to eddy currents and hysteretic response. The imaginary part of permeability, μ'' decreased with increasing frequency. It is clearly seen that the increasing in Cr content has a tendency to increasing in imaginary value of permeability. Which is in contrast with real part *i.e*, μ' that decrease with increasing Cr content This is probably due to impediment of crystallization of soft magnetic α-Fe(Si) phase in the amorphous matrix imposed by higher content of refractory Cr. This restricts the growth of α-Fe(Si) nanocrystals resulting in inhomogeneous distribution of magnetic nanograins having weak exchange coupling. This situation favours higher magnetic loss component. *i.e.* μ'' increases with increasing of Cr content. The imaginary part μ'' has attained minimum value at frequency of around 100 kHz and above, implying that around this frequency range the device made from these ribbons would be suitable for practical applications.

5.1.5.3 Loss Tangent

The magnetic loss of a soft ferromagnetic material depends on the irreversible magnetization process and is predominantly obtained by pinning of domain wall motion. The hysteresis losses are partially due to pinning sites from deficiencies in the material and stresses established in the material during rapid solidification. In order to relieve the stresses a heat treatment protocol was applied [121]. From the Figure 5.17 and 5.18 it is demonstrated that loss tangent ($\tan\delta = \mu''/\mu'$) of all the samples have attained minimum value at AC frequency of around 100 kHz. It is also observed that higher Cr content sample show higher $\tan\delta$ compared with low Cr content. These results show that higher Cr content alloys are not suitable for application as core material. Minimum magnetic loss (tanδ) is demonstrated for sample with Cr = 1 and at frequency of f = 100 kHz.

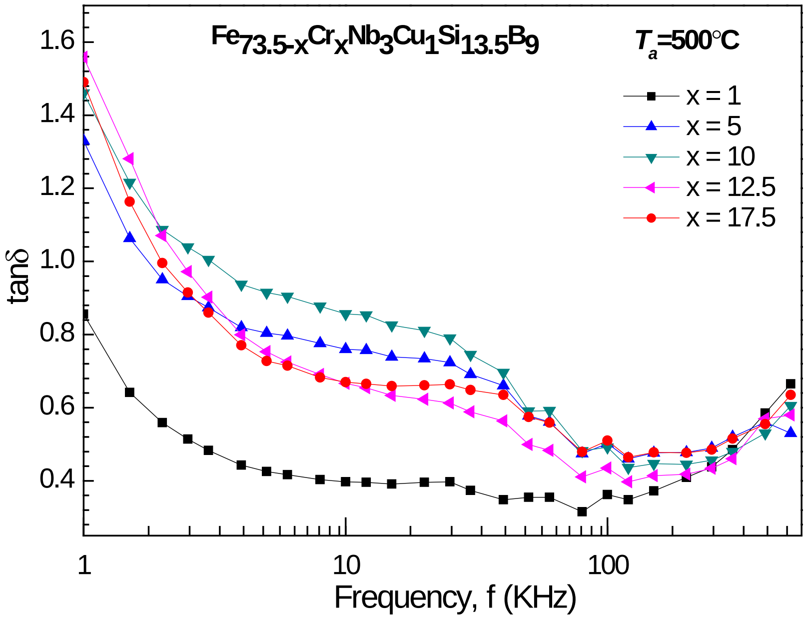

Figure 5.17: Frequency dependent loss tangent for $Fe_{73.5-x}Cr_xNb_3Cu_1Si_{13.5}B_9$ alloys at T_a = 500°C.

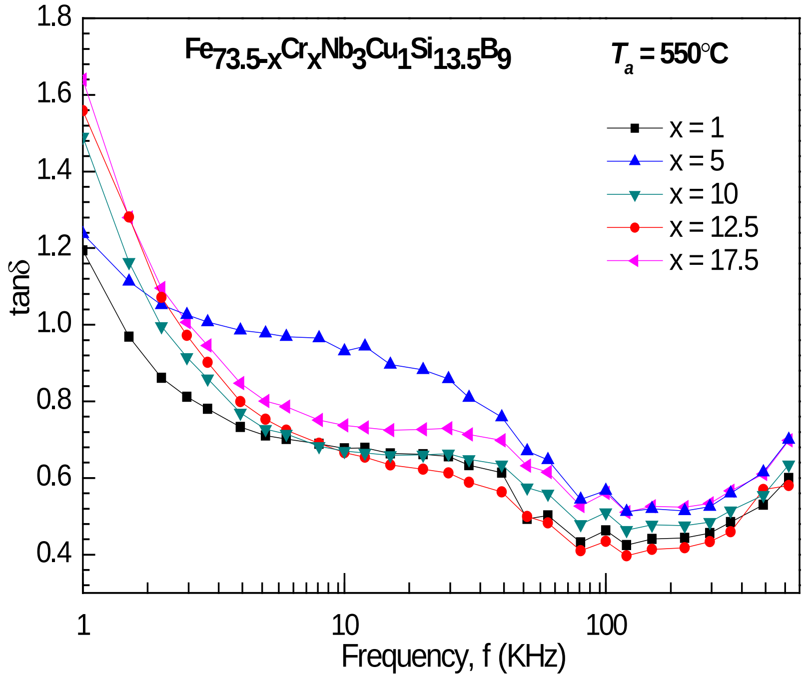

Figure 5.18: Frequency dependent loss tangent for $Fe_{73.5-x}Cr_xNb_3Cu_1Si_{13.5}B_9$ alloys at T_a = 550°C.

5.1.6 Analysis of Mössbauer Spectroscopy

Conventional results obtained in Mössbauer measurements for the $Fe_{73.5x}Cr_xNb_3$ $Cu_1Si_{13.5}B_9$ alloy as a function of the annealing temperature, T_a, are presented in Figure 5.19 - 5.23. As can be seen, the arrangement of the nanocrystalline phase as well as the changes of the magnetic properties of the retained amorphous phase is evidently noticeable. The spectra in Figure 5.19 of the fully amorphous samples of the as-quenched sample of x = 1 consist of strongly overlapping Zeeman sextet which illustrate distinctive amorphous phase for amorphous alloys which was measured by the fitting procedure of experimental data with theoretical prediction.

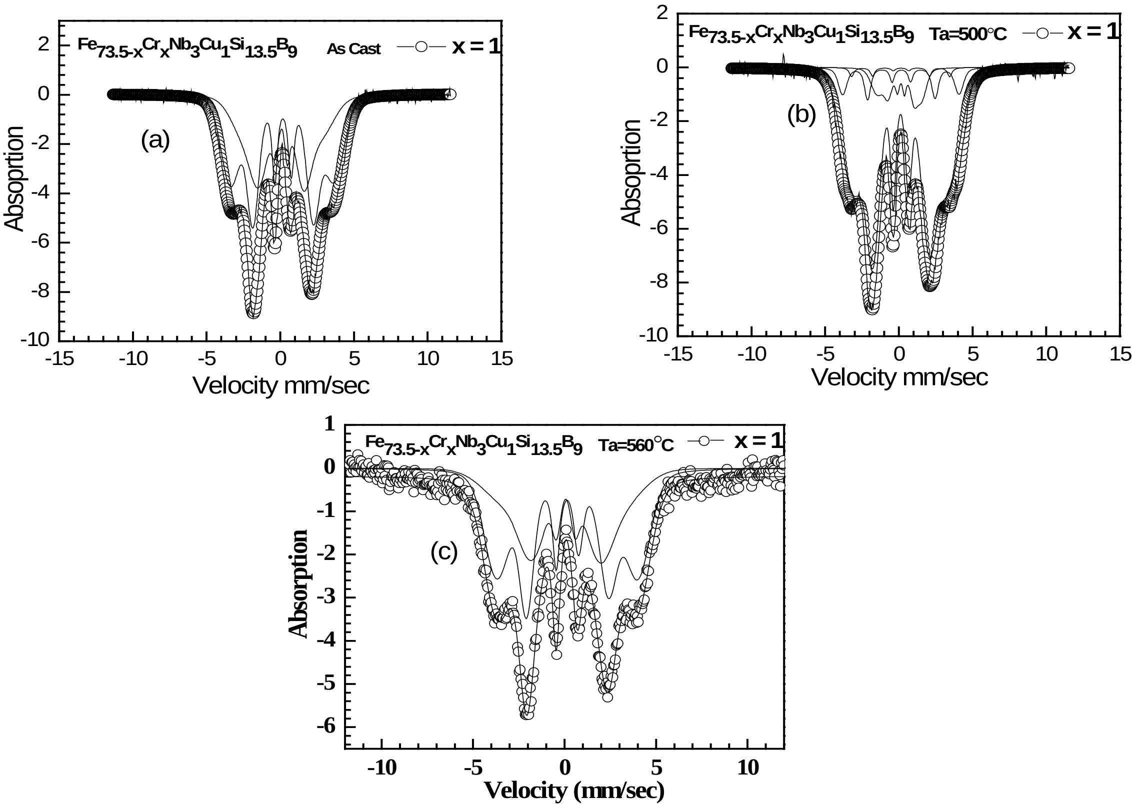

Figure 5.19: Mössbauer spectra of $Fe_{73.5-x}Cr_xNb_3Cu_1Si_{13.5}$ B_9 alloy for x = 1 at (a) as cast, (b) 500°C and (c) 560°C.

The Mössbauer spectra of the entire samples were recorded at room temperature by using ^{57}Fe Mössbauer spectrometry in transmission geometry with constant acceleration spectrometer. We assume Cr = 1 for as cast, 500°C and 560°C. From this

Figure 5.19 we can see the good agreement with theoretical and experimental results for as cast sample. Am_1 is 41% and 60 % respectively. The amount of amorphous or iron rich phase represented by Am_1 and iron depleted amorphous phase is represented as Am_2. At increased temperature 500°C, the Am_2 is decreased and it is observed that 34.2 % amorphous and 65.8% α-Fe-Si phase and at 560°C Am_1 is 18.2% and α-Fe-Si phase 81.8%. When annealing temperature is increased the Am_1 decreased and α-Fe-Si increased. The amount of amorphous, crystalline α-(Fe-Cr)-Si phase and % of Fe are presented in Table 5.4.

Table 5.4: Hyperfine parameters of Mössbauer spectra of $Fe_{73.5-x}Cr_xCu_1Nb_3Si_{13.5}B_9$ in as-cast and annealed condition for x = 1.

Anneal Condition	Species	H (T)	dH (T)	V_0 mm/s	Rel. Area (%)	% of Fe	Wt. fraction of phases (%)
As-Cast	Am_1	15.82	0.843	0.148	0.410	47.46	Amorphous~100
	Am_1	21.73	0.575	0.0537	0.606	65.19	
500°C for 30 min	Am_2	9.26	0.313	0.209	0.342	27.78	Amorphous~34.2 α-(Fe-Cr)-Si~65.8
	α-Fe-Si	20.58	0.0134	0.029	0.644	61.74	
	α-Fe-Si	24.43	0.200	0.029	0.014	73.29	
560°C for 30 min.	Am_1	13.29	1.781	0.086	0.182	39.87	Amorphous~18.2 α-(Fe-Cr)-Si~81.8
	α-Fe-Si	19.84	0.027	0.0031	0.270	59.52	
	α-Fe-Si	24.72	0.041	0.551	0.106	74.16	
	α-Fe-Si	30.99	0.059	0.551	0.210	92.97	
	α-Fe-Si	14.70	1.817	0.551	0.232	44.1	

The relative contributions of these spectral components transform with annealing temperature. The enhanced annealing temperature causes a boost of the relative amount of the nanocrystalline phase from about 10% to about 20% at T_a = 500°C and 560°C which is represented in Figure 5.19(b) and 5.19(c) respectively. The involvement of the interfacial region also decreases at the rate of the component equivalent to the amorphous matrix. It is noted that spin orientations are different in the amorphous and interfacial regions. There is a strong preference for the in planes spin orientation in the retained amorphous phase, whereas spins of Fe atoms in the interfacial regions reveal random orientation [122].

The line intensity ratio of the second to third line in the elementary Zeeman sextet increases markedly from about 2 for the as-quenched alloy in Figure 5.20 to about 4 for the $Fe_{73.5-x}Cr_xNb_3Cu_1Si_{13.5}B_9$ at 500, 580 and 600^oC where x = 5. This indicates that the spin orientation in the starting alloy is random, whereas annealing introduces anisotropy which persuades preferential spin orientation in plane of the ribbon. Annealing at T_a > 490°C, when the nanocrystalline phase is formed, as indicated by the DSC and XRD studies, [123] caused clear changes in the Mössbauer spectra in Figure 5.20. The spectra of the two-phase amorphous and nanocrystalline systems description the attendance of three components: the Zeeman sextet with a distinct value of the hyperfine field, and corresponding to the interfacial region between the *bcc*-Fe nanocrystals and the amorphous matrix. In the crystalline or amorphous interfacial regions Fe atoms located at the surface of the nanograins and/or in their nearest neighborhood experience various local atomic structures as a result of which the hyperfine field is reduced as compared with Fe atoms in the core of the *bcc*-Fe grains, which have a well-defined crystalline structure [124]. The average hyperfine field at room temperature corresponding to the amorphous phase decreased due to annealing as compared with the as-quenched alloy Figure 5.20. Formation of the *bcc*-Fe phase causes a decrease of iron content in the retained amorphous phase and leads to a decrease of Curie temperature of the amorphous phase. Figure 5.20 the Mössbauer spectra of melt spinning ribbon sample of composition $Fe_{73.5-x}Cr_xNb_3Cu_1Si_{13.5}B_9$ where x = 5 for as cast and annealed like 500^oC, 580^oC and 600^oC are presented. The Mössbauer spectrum of the as cast and annealed condition for all composition shows sextet pattern, the spectra consist of broad overlapped lines assigned to disorder structural position of resonant alloys and the sharp narrow lines indicate a percentage of *bcc*-Fe crystalline. Hence consider Cr = 5 for as cast, 500°C, 580 and 600°C. From these Figure we can observe that, the excellent harmony between theoretical and experimental results for as cast sample was in almost amorphous. At 500°C, the Am_1 is decrease and it is shown 41.4% amorphous and 53.9% α-Fe-Si phase, at 580°C, Am_1 is 26.7% and α-Fe-si phase 73% and at 600°C, Am_1 is 23% and α-Fe-si phase is 79%. It can perceive that, when annealing temperature is increased, Am_1 decreased and α-Fe-Si increased. The amounts of amorphous, crystalline α-(Fe-Cr)-Si and % of Fe are presented in the Table 5.5.

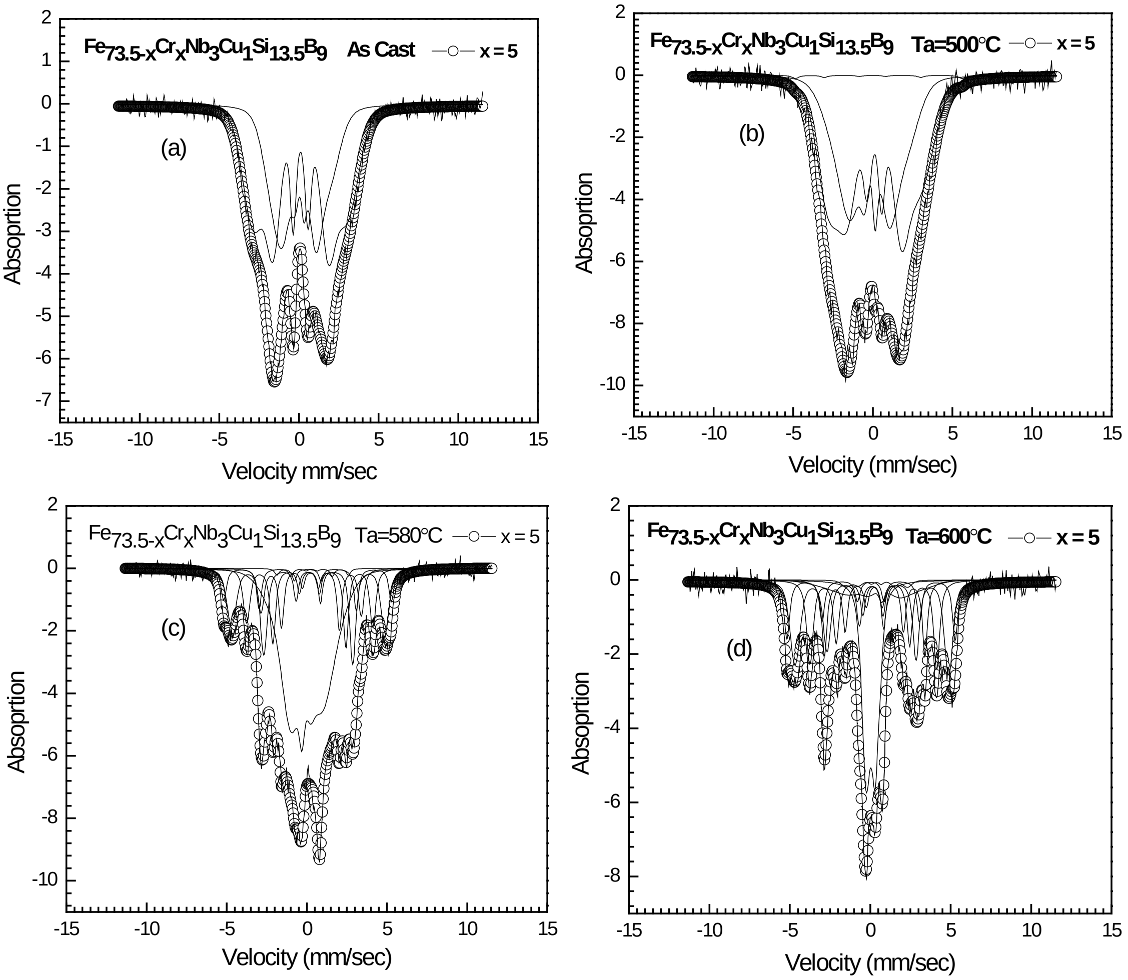

Figure 5.20: Mössbauer spectra of $Fe_{73.5-x}Cr_xNb_3Cu_1Si_{13.5}B_9$ for x = 5 at (a) as cast, (b)500°C, (c) 580°C and (d) 600°C .

Table 5.5: Hyperfine parameters of Mössbauer spectra of $Fe_{73.5-x}Cr_xCu_1Nb_3Si_{13.5}B_9$ in as-cast and annealed condition for x = 5.

Anneal Condition	Species	*H* (*T*)	d*H* (*T*)	V_0 mm/s	Rel. Area (%)	% of Fe	Wt. fraction of phases (%)
As-Cast	Am_1	18.11	0.629	0.0214	0.588	54.33	Amorphous-100
	Am_1	10.64	0.562	0.079	0.391	31.92	
500°C for 30 min	Am_1	12.20	0.830	0.00	0.414	36.6	Amorphous~41.4
	α-Fe-Si	32.34	0.0159	0.00	0.539	97.02	α-(Fe-Cr)-Si~53.9
580°C for 30 min	Am_1	14.70	1.608	0.536	0.177	44.1	Amorphous~26.7 α-(Fe-Cr)-Si~73.3
	Am_1	13.79	0.010	0.536	0.090	41.37	
	α-Fe-Si	19.33	0.0917	0.536	0.086	57.99	
	α-Fe-Si	24.33	0.114	0.536	0.114	72.99	
	α-Fe-Si	29.60	0.200	0.536	0.157	88.8	
	α-Fe-Si	29.40	0.0659	0.536	0.067	88.2	
	α-Fe-Si	9.63	0.855	0.000	0.309	28.89	
600°C for 30 min	Am_1	15.14	1.120	0.600	0.152	45.42	Amorphous~23 α-(Fe-Cr)-Si~79.1
	Am_1	11.76	0.200	0.600	0.079	35.28	
	α-Fe-Si	19.31	0.011	0.600	0.129	57.93	
	α-Fe-Si	24.37	0.0921	0.600	0.175	73.11	
	α-Fe-Si	29.53	0.200	0.600	0.222	88.59	
	α-Fe-Si	32.34	0.048	0.600	0.139	97.02	
	α-Fe-Si	28.81	0.160	0.102	0.126	86.43	

The Mössbauer spectra recorded at room temperature at 500°C and 600°C annealing temperature for Cr = 10 which are shown in Figure 5.21 for 30 minutes.

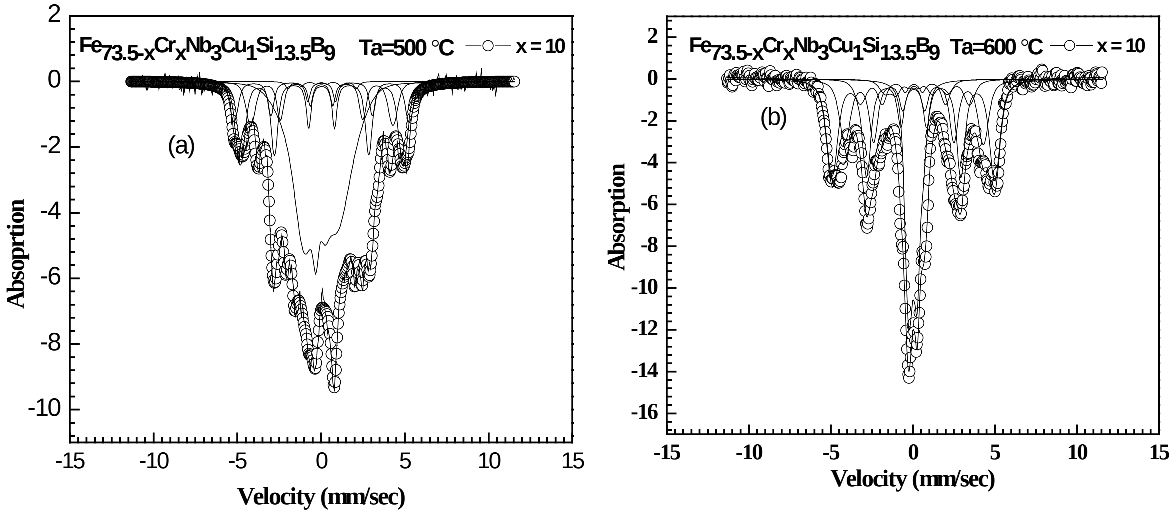

Figure 5.21: Mössbauer spectra of $Fe_{73.5-x}Cr_xNb_3Cu_1Si_{13.5}B_9$ for x =10 at (a) 500°C and (b) 600°C.

The doublet in the spectra is attended by the sidebands which reproduce the shape of the central collapsed constituent. Full collapse of the magnetic hyperfine structure occurred what shows that the magnetic anisotropy in these alloys is considerably smaller than the intensity of the external field [110].

The Mössbauer spectra of Cr = 10 were recorded at room temperature by using ^{57}Fe Mössbauer spectrometry in transmission geometry with constant acceleration spectrometer. Here, the value were taken for Cr = 10 for as cast, 500^{o}C and 600^{o}C which are represented in Figure 5.21. From this figure it is seen that, the agreement between theoretical and experimental results are well fitted for both annealed samples. When temperature increases at 500^{o}C, the Am$_1$ is 78% and α-Fe-Si phase is 22% whereas for 600^{o}C, Am$_2$ is 38.4% and α-Fe-Si phase 62%. So it can be concluded that, when annealing temperature is increased, Am$_1$ decreased and α-Fe-Si increased. But for high Cr content crystallization is delayed. The amount of amorphous crystalline α-(Fe-Cr)-Si and % of Fe are presented in Table 5.6.

Table 5.6: Hyperfine parameters of Mössbauer spectra of $Fe_{73.5-x}Cr_xCu_1Nb_3Si_{13.5}B_9$ in as-cast and annealed condition for x = 10.

Anneal condition	Species	H (T)	dH (T)	V_0 mm/s	Rel. Area (%)	% of Fe	Wt. fraction of phases (%)
500°C for 30 min	Am$_1$	2.89	0.214	0.064	0.430	8.67	Amorphous~78 α-(Fe-Cr)-Si~22
	Am$_1$	12.63	0.010	0.049	0.0081	37.89	
	Am$_2$	26.25	0.200	0.049	0.089	78.75	
	Am$_2$	14.70	2.35	0.085	0.255	44.1	
	α-Fe-Si	30.06	0.200	0.049	0.154	90.18	
	α-Fe-Si	32.34	0.157	0.049	0.068	97.02	
600°C for 30 min	Am$_2$	23.52	20.00	0.126	0.348	70.56	Amorphous~38.4 α-(Fe-Cr)-Si~62
	α-Fe-Si	17.23	0.180	0.126	0.344	51.69	
	α-Fe-Si	24.70	0.190	0.126	0.026	74.1	
	α-Fe-Si	30.15	0.162	0.126	0.096	90.45	
	α-Fe-Si	33.03	0.148	0.126	0.161	99.09	

The Mössbauer results in Figure 5.22 clearly show that the nanocrystalline phase is weak ferrimagnetic than both the starting amorphous phase and the retained amorphous matrix in which the nanocrystals are embedded. The Mössbauer measurements of x = 12.5 performed as a function of the field intensity for the sample annealed at 580^{o}C and 600^{o}C provided detailed information concerning the anisotropy fields. The onset of the spectral collapse effect in the as-cast amorphous alloy is clearly seen in Figure 5.22. The induced magnetization is observed in the Mössbauer spectrum as a complete collapse of the magnetic hyperfine structure to the quadruple split doublet [109]. This means that the magnetic anisotropy field in the amorphous phase is considerably smaller than 32T but probably somewhat larger than 2T. A further increase of the field intensity does not affect the shape of the collapsed central doublet Figure 5.22. Such a field intensity dependence of the collapse effect strongly suggests that the magnetic anisotropy in the amorphous as-quenched alloy is well depended and has fairly narrow distribution.

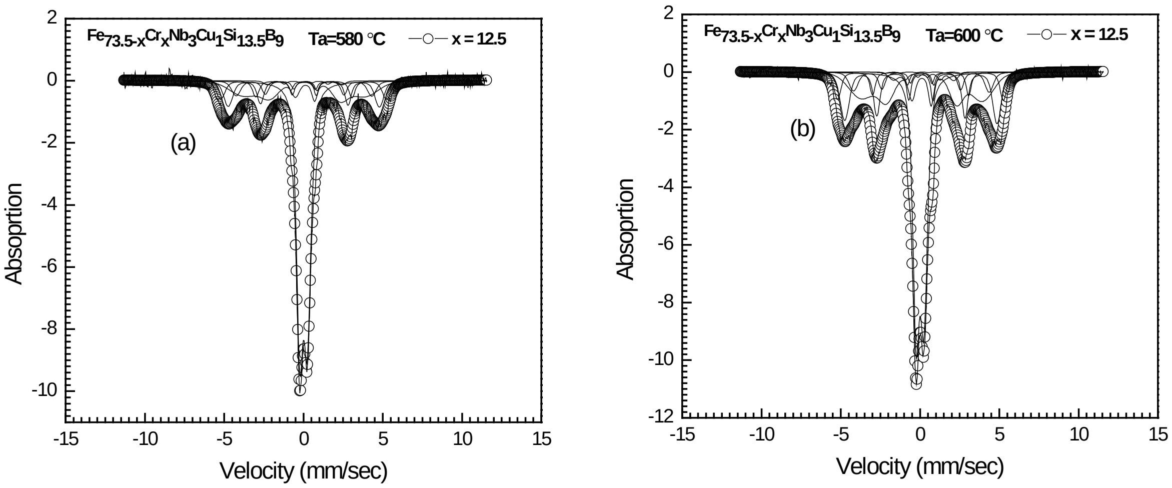

Figure 5.22: Mössbauer spectra of $Fe_{73.5-x}Cr_xNb_3Cu_1Si_{13.5}B_9$ for x = 12.5 at (a) 580^{o}C and (b) 600^{o}C.

The increase of the field intensity leads to a complete collapse of the spectral component, characteristic for the retained amorphous phase, to a central quadruple doublet. However, the collapsed in doublet is still considerably broadened, which suggests that the magnetic hyperfine field was not completely averaged to zero in clear distinction to the case of the as cast alloy from Figure 5.22 for x = 12.5, in which the field was sufficient to induce a complete collapse [109,110]. Also at the central collapsed doublet contains magnetic wings. Such a behavior of the collapsed pattern strongly suggests that despite the fact that the retained amorphous phase is magnetically very soft, it clearly shows magnetic anisotropy larger than the as-quenched, fully amorphous alloy. The Mössbauer spectra of x = 12.5 for both of amorphous and α-Fe-Si phases were documented at room temperature by using ^{57}Fe Mössbauer spectrometry in transmission geometry with constant acceleration spectrometer. The sample for Cr = 12.5 were annealed at at 580^{o}C and 600^{o}C which represented at Figure 5.22 from where it can deduce that the theoretical and experimental observation for both annealing temperature at 580^{o}C and 600^{o}C are matched in good manner. The amorphous Am_1 and α-Fe-Si phase quantity are 45.3% and 53.7 % for 580^{o}C respectively. Likewise increase in temperature at 600^{o}C, the Am_1 is decrease at 39% as amorphous and α-Fe-Si phase is 59%. So, from the above information we found that, when annealing temperature is increase, Am_1 decreased and α-Fe-Si increased. The amounts of amorphous, crystalline α-(Fe-Cr)-Si and % of Fe are presented in are given in Table 5.7.

Table 5.7: Hyperfine parameters of Mössbauer spectra of $Fe_{73.5-x}Cr_xCu_1Nb_3Si_{13.5}B_9$ in as-cast and annealed condition for x = 12.5.

Anneal condition	Species	H (T)	dH (T)	V_0 mm/s	Rel. Area (%)	% of Fe	Wt. fraction of phases
580°C for 30 min	Am_1	2.25	0.100	0.00	0.453	6.75	Amorphous~45.3 α-(Fe-Cr)-Si ~53.7
	α-Fe-Si	14.7	0.106	0.211	0.035	44.1	
	α-Fe-Si	26.46	0.200	0.211	0.177	79.38	
	α-Fe-Si	29.47	0.200	0.211	0.133	88.41	
	α-Fe-Si	32.34	0.188	0.211	0.192	97.02	
600°C for 30 min	Am_1	2.33	0.100	0.001	0.390	6.99	Amorphous~39 α-(Fe-Cr)-Si~59
	α-Fe-Si	11.76	0.200	0.293	0.041	35.28	
	α-Fe-Si	14.7	0.015	0.293	0.096	44.1	
	α-Fe-Si	26.46	0.200	0.293	0.174	79.38	
	α-Fe-Si	29.69	0.200	0.293	0.191	89.07	
	α-Fe-Si	32.34	0.131	0.293	0.088	97.02	

The *bcc*-Fe nanocrystalline magnetic component in the Mössbauer spectra collapse significantly which is shown in Figure 5.23 for x = 17.5 some narrowing of this six-line spectral component can be detected for the internal field applied. Thus, the magnetic anisotropy in the bcc-Fe grains is much larger than that of the retained amorphous phase and is sufficiently large to prevent the peaks collapse. From the Mössbauer spectra in Figure 5.23 we can deduce that the magnetic anisotropy in the retained amorphous phase has an average value below while the existence of the magnetic wings in the spectrum recorded with a field applied suggests a fairly broad distribution of anisotropy fields related probably to the stresses in the amorphous phase due to the precipitation of the nanocrystalline phase. The nanocrystalline phase is magnetically much harder than the retained amorphous phase. The collapse of the six-line spectral component is almost negligible even for the field which proves that the magnetic anisotropy exceeds and prevents magnetization reversal.

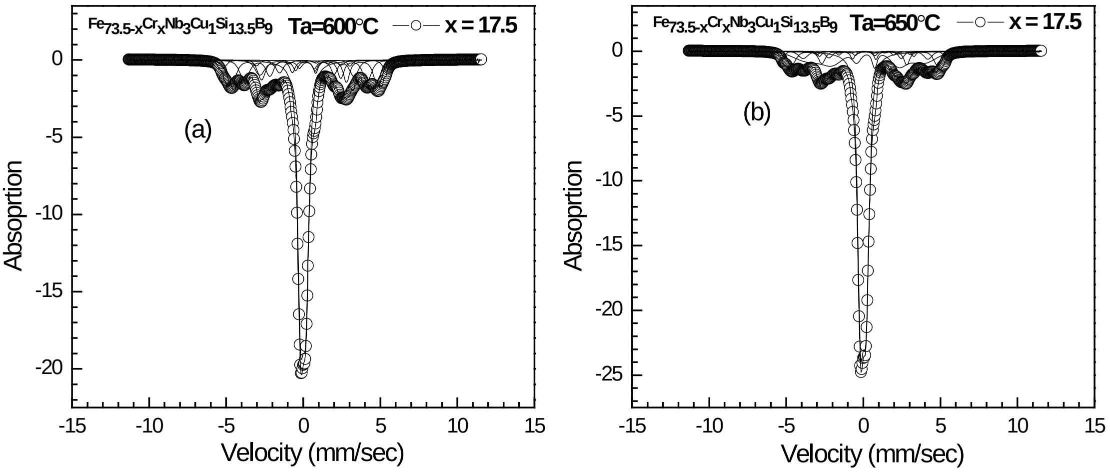

Figure 5.23: Mössbauer spectra of $Fe_{73.5-x}Cr_xNb_3Cu_1Si_{13.5}B_9$ for x = 17.5 at (a) 600°C and (b) 650°C.

That the dilution of the magnetic moment of amorphous and nanocrystalline phase gradually increases with the depletion of Fe. In Figure 5.23 it is seen that observed that central doublet region of the sample annealed at 600°C is smaller than the sample annealed at 650°C. This is because as the annealing temperature increases, the Fe is depleted more in the α-Fe-Si nanograins due to anneal at higher temperature. This reduces the exchange interaction between the α-Fe-Si nanograins as a result of which overall magnetic contribution decrease for higher temperature. Theoretical and experimental fitting matches well within six subspecies. After fitting it can be observed that ~65% contribution is paramagnetic (fast relaxation) and ~35% contribution is ferromagnetic (slow relaxation) for the annealing temperature at 600^{o}C. Whereas, for temperature at 650^{o}C, the contribution from amorphous phase is 45% which has reduced due to higher annealing temperature and the contribution of a nanocrystalline phase is 55%. Though at higher annealing temperature advantage of

Table 5.8: Hyperfine parameters of Mössbauer spectra of $Fe_{73.5-x}Cr_xCu_1Nb_3Si_{13.5}B_9$ in as-cast and annealed condition for x = 17.5.

Anneal Condition	Species	H (T)	dH (T)	V_0 mm/s	Rel. Area (%)	% of Fe	Wt. fraction of phases
600°C for 30 min	Am_1	11.76	0.200	0.449	0.011	35.28	Amorphous~76 α-(Fe-Cr)-Si~24
	Am_1	1.73	0.105	0.0015	0.600	5.19	
	Am_2	25.02	0.200	0.449	0.052	75.06	
	Am_2	29.40	0.200	0.449	0.097	88.2	
	α-Fe-Si	18.82	0.034	0.449	0.200	56.46	
	α-Fe-Si	32.34	0.010	0.449	0.040	97.02	
650°C for 30 min	Am_2	1.66	0.103	0.00	0.450	4.98	Amorphous~45 α-(Fe-Cr)-Si~55
	α-Fe-Si	13.38	0.093	0.536	0.035	40.14	
	α-Fe-Si	18.82	0.200	0.536	0.106	56.46	
	α-Fe-Si	24.59	0.200	0.536	0.143	73.77	
	α-Fe-Si	29.40	0.200	0.536	0.152	88.2	
	α-Fe-Si	32.34	0.085	0.536	0.115	97.02	

α-Fe-Si nanograins increased the percentage of large volume fraction of amorphous phase indicates exchange interaction between the nanograins and Mössbauer spectrograph is characterized by the mixed relaxation. The amounts of amorphous, crystalline α-(Fe-Cr)-Si and % of Fe are presented in Table 5.8. From the Cr content spectra we can see that when Cr content was lower we get select pattern as we increase Cr content we can see change of spectrum from sextet to doublet at Cr = 17.5 this is due to the dilution of magnetization. As Cr content increase magnetic dilution occurs and the pattern of the spectra changes from ferromagnetic to paramagnetic state.

5.2 Compositions II ($Fe_{76.5-x}Nb_xCu_1Si_{13.5}B_9$)

5.2.1 Crystallization Phase Analysis by Differential Scanning Calorimetry

Differential scanning calorimetry (DSC) has been performed on selected sample of $Fe_{76.5-x}Nb_xCu_1Si_{13.5}B_9$ system with x = 3, 5 and 7 to elucidate the crystallization temperatures. Figure 5.24 shows the DSC curves with constant heating rate of 20^oC/min for these three samples where two exothermic peaks corresponding to primary and secondary crystallization phenomena are observed. The first peak corresponds to α-Fe(Si) phase and the second one corresponds to Fe-B phase. Our interest from these curves is only with primary crystallization temperature because for the soft magnetic properties the primary phase α-Fe(Si) plays a vital role in magnetic softening. In contrary the secondary phase corresponding to Fe-B is determined for soft magnetic properties due to its high magnetic anisotropy energy. For this reason, annealing is always carried out at temperature lower than the crystallization temperature of secondary phase formation. Therefore these DSC curves help us to confidently decide the appropriate temperature for annealing treatment.

It is observed from curves that primary crystallization peak temperature shifts to higher temperature range as the Nb content is increased, indicating that Nb addition enhances the thermal stability of the alloys. Thus the crystallization event becomes more difficult for sample with higher Nb content of x = 7 where primary crystallization temperature become 586°C compared with 555°C for the sample x = 5.

From DSC thermogram, it is seen that the secondary peak temperature also shifted to higher value with the increasing of Nb content. The results are displayed in Table 5.9.

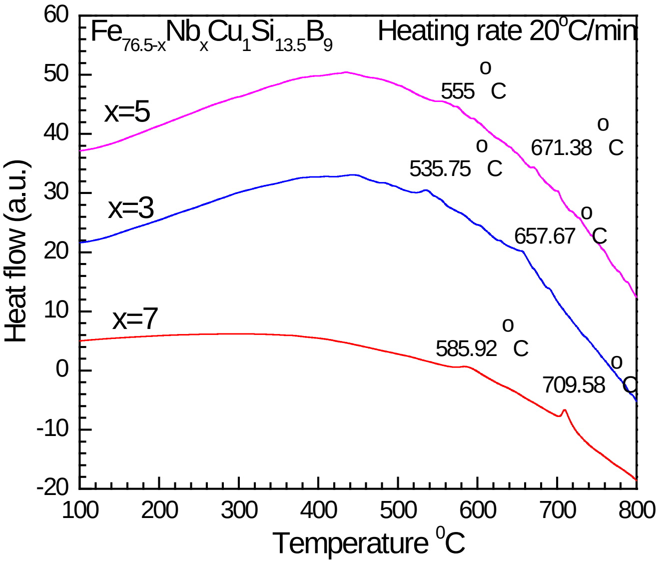

Figure 5.24: DSC thermogram of $Fe_{76.5-x}Nb_xCu_1Si_{13.5}B_9$ alloys for x = 3, 5 and 7 at heating rate 20°C /min.

Table 5.9: Primary and secondary crystallization temperatures of $Fe_{76.5-x}Nb_xCu_1Si_{13.5}B_9$ for x = 3, 5 and 7.

Nb (x)	Heating rate /min	Primary peak temperature T_{p1} in °C	Secondary peak temperature T_{p2} in °C
3	20°C	536	658
5		555	671
7		586	710

Figure 5.25 depicts the heating rate dependence of DSC thermogram for x = 7 sample. Analyzing the data of peak temperature and the heating rate we calculated activation energy using the following Kissingers relation [114].

$$\ln\left(\frac{B}{T_P^2}\right) = -\frac{E}{k_B}T_P + \text{constant} \qquad (5.1)$$

where, B is the heating rate, T_P is the crystallization peak temperature, E is the crystallization activation energy and k_B is the Boltzman constant. From the Arrhenius plot of equation (5.1) we found the value activation energy as 4.24 eV and 7.68 eV for primary and secondary crystallization of the sample x = 7 respectively. The primary crystallization peak temperature T_{p1} and secondary crystallization peak temperature T_{p2} corresponds to 576 and 709°C respectively for heating rate of 10°C/min. The primary and secondary crystallization temperatures for different heating rates are shown in Table 5.10. It is observed that the crystallization temperature increased with increasing Nb content and the crystallization peak temperature has been shifted towards the higher temperature value which necessitates an increase in crystallization energy. The DSC study on selected samples has clearly demonstrated that Nb has strong effect on the crystallization kinetics of the FINEMET alloys [125, 126]. The higher the Nb content the higher is the stability of FINEMET alloys. It means that higher thermal energy is required to initiate the crystallization event. In the proceeding section we will show that increasing Nb content will retard the grain growth due to obstacles made by refractory Nb keeping grain size limited to lower values [127, 128].

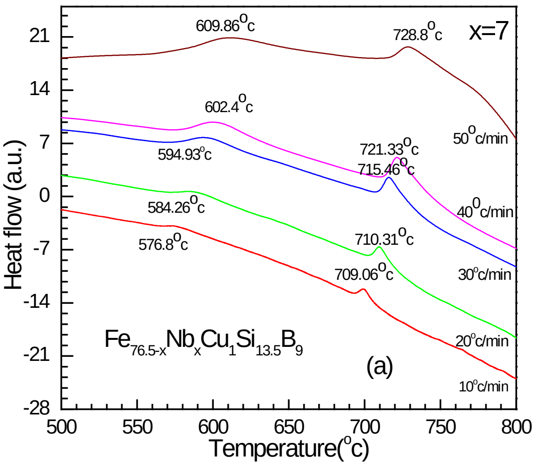

Figure 5.25: (a) DSC thermograms of $Fe_{76.5-x}Nb_xCu_1Si_{13.5}B_9$ alloys for x = 7 at different heating rate and (b) Kissinger plot for the same DSC data.

Table 5.10: Onset of primary crystallization temperature T_{x1}, primary crystallization peak temperature T_{p1}, onset of secondary crystallization temperature T_{x2}, secondary crystallization peak temperature T_{p2}, difference between two peak temperature ΔT, activation energies of primary and secondary crystallization E_{a1} and E_{a2} respectively. Where Nb content x = 7.

Heating rate (°/min)	Primary crystallization onset temperature T_{x1} in ^oC	Primary peak temperature T_{p1} in ^oC	Secondary crystallization onset temperature T_{x2} in ^oC	Secondary peak temperature T_{p2} in ^oC	Difference between two peak temperature ΔT	Activation energy of Fe(Si) phase E_{a1} in eV	Activation energy of Fe-B phase E_{a2} in eV
10	565	576	693	709	133	4.24	7.68
20	577	586	702	710	126		
30	582	595	708	716	121		
40	585	604	713	721	117		
50	596	610	719	729	119		

5.2.2 X-ray Diffraction Analysis of $Fe_{76.5-x}Nb_xCu_1Si_{13.5}B_9$

The crystal structure of the studied samples was analyzed by an X-ray powder diffractometer using Cu-Ka radiation. The XRD patterns of $Fe_{76.5-x}Nb_xCu_1Si_{13.5}B_9$ (x = 1, 2, 3, 4, 5, 6 and 7) alloys in as cast and annealed at 550, 580 and 600^{o}C for 30min are shown in Figures 5.26. The typical amorphous structure of as quenched or as cast samples is clearly revealed in the diffraction pattern with the manifestation of broader peaks characteristics of typical amorphous phase in Figure 5.26(a). The samples annealed at 550, 580 and 600^{o}C exhibit crystalline peaks at [110] plane belonging to the α-Fe(Si) phase as confirmed by search and match method using high score plus software. Crystallization effect on annealing for the studied samples are shown in Figure 5.26(b),(c),(d) as XRD pattern where broadened diffused peaks of the amorphous phase have become sharper representing crystalline state of the samples. It is observed in Figure 5.26(b) that at annealing temperature, T_a = 550°C all the samples except Nb = 6 and 7 have been crystallized. We observed here a good coincidence with DSC thermogram that peak crystallization temperature of x = 5 and

7 are T_{p1} = 555 and T_{p1} = 586°C respectively. It is obvious that annealing at T_a = 550°C may not trigger crystallization in these two alloys, while samples with x ≤ 5 have displayed profound effect of crystallization. All samples with x ≤ 5 show sharp and narrow crystallization peaks implying that crystals have already grown on the amorphous matrix. It does happened because the annealing temperature T_a = 550°C is higher than

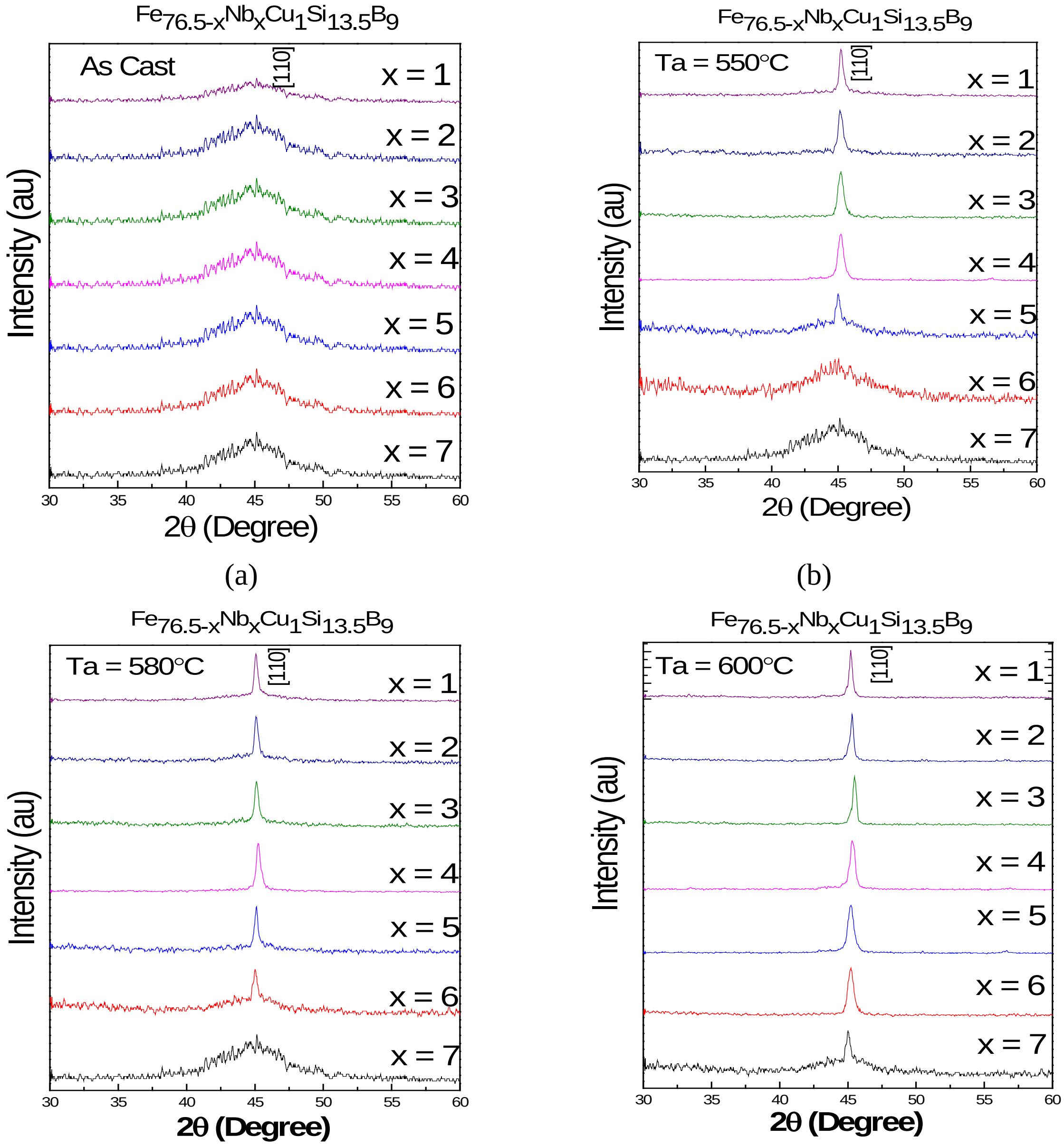

(a)

(b)

(c)

(d)

Figure 5.26: XRD patterns of $Fe_{76.5-x}Nb_xCu_1Si_{13.5}B_9$ in (a) as cast and annealed at (b) 550^{o}C, (c) 580^{o}C and (d) 600^{o}C for different Nb content x.

the crystallization peak temperature of the alloys with $x \leq 5$. An improvement in the crystallization effect is clearly observed when the annealing temperature is set at T_a = 580°C for 30 min for all the samples (see Figure 5.26(c). Sample with x = 6 displays sharp peak and for x = 5 peak becomes more matured and sharp, but for x = 7 no peak is manifested. It is still in the amorphous state because the crystallization peak T_{p1} for x = 7 is 586°C which is higher than the set annealing temperature at T_a = 580°C. Figure 5.26(d) depicts complete crystallization of all the studied samples where no broad diffused peak corresponding to amorphous state is evidenced. This due is to the reason that the set T_a = 600°C is higher than the peak crystallization temperature determined from the DSC thermogram for all the studied samples. Later during the microstructural study using FESEM, we will correlate these observations with the growth of nanocrystals on the amorphous matrix as a function of annealing temperature.

XRD is a unique technique to determine the crystallite size and or grain size developed through thermal treatment called annealing at an appropriate temperature above or close to the crystallization peak temperature (T_{p1}) obtained from the DSC thermogram. It is generally calculated using Scherrer's formula from the X-ray diffraction pattern where full width at half maximum (FWHM) is taken as a parameter. This is to be noted that grain sizes from 1 nm to 100 nm can be calculated using this formula. When an amorphous material is crystallized, it shows well defined sharp peak at different crystalline planes in contrast with broad hump peak for the amorphous state. The sharper and narrower the diffraction peak, larger is the grain size [84, 129].

Table 5.11: Grain size estimated from XRD peak of crystalline for $Fe_{76.5-x}Nb_xCu_1Si_{13.5}B_9$ alloys with different Nb content and annealing temperature.

T_a (°C)	Nb Content (x)	Crystalline Phase	Grain size (nm)
As cast	1	All samples are amorphous	-
	2		-
	3		-
	4		-
	5		-
	6		-
	7		-
550	1	α-Fe(Si)	16
	2	α-Fe(Si)	12
	3	α-Fe(Si)	9
	4	α-Fe(Si)	7
	5	α-Fe(Si)	6
	6	amorphous	-
	7	amorphous	-
580	1	α-Fe(Si)	22
	2	α-Fe(Si)	18
	3	α-Fe(Si)	12
	4	α-Fe(Si)	11
	5	α-Fe(Si)	10
	6	α-Fe(Si)	9
	7	amorphous	-
600	1	α-Fe(Si)	24
	2	α-Fe(Si)	19
	3	α-Fe(Si)	14
	4	α-Fe(Si)	11
	5	α-Fe(Si)	9
	6	α-Fe(Si)	8
	7	α-Fe(Si)	6

FWHM values were measured from the XRD pattern annealed at different temperature from Figure 5.26(b), (c), (d). Since Figure 5.26 (a) does not show any crystalline peak, meaning that no crystals have developed. Using the determined FWHM values, the grain sizes of the developed crystallites upon thermal treatment at various temperature around T_p were calculated and displayed in Table 5.11 for all the studied samples. It is observed from the table that grain sizes decrease with increasing Nb content (x) and increase gradually as the annealing temperature T_a increases for same Nb content sample. This may be attributed due to the role of Nb as a refractory metal having high thermal stability and larger atomic radius. Noteworthy that during the process of crystallization Cu enhances the nucleation of nanograin while Nb with a large atomic size restricts the nanocrystalline growth.

Since the Cu content is constant in the studied alloys, role of Nb is the driving force for the control of the size of nanograin including temperature. The increasing of nanograin size with temperature is simply connected with energy minimization scheme [8]. The grain size decreases from 24 nm for x = 1 to 6 nm for the sample x = 7 at an annealing temperature of T_a = 600° C while at T_a = 550° C, the grain size decreases from 16 nm for x = 1 to 6 nm of the sample with x = 5 having no grains developed for x > 5 samples. It is because the annealing temperature T_a = 550° C is lower than the crystallization temperature of these alloys. These findings clearly demonstrate the role of grain growth inhibitor Nb, effect of temperature and the crystallization behavior of nanocrystalline FINEMET type of alloys prepared initially in the amorphous state by rapidly solidified technique.

5.2.3 Microsrtuctural study of $Fe_{76.5-x}Nb_xCu_1Si_{13.5}B_9$

Field Emmission Scanning Electron Microscope (FESEM) is very useful technique for microstructural study. The main objective of the present study is to determine the nanocrystalline grain size [130]. The white lines in the micrograph scale represent 100 nm. The FESEM microstructure of the alloys of $Fe_{76.5-x}Nb_xCu_1Si_{13.5}B_9$ with x = 1, 2, 3, 5 and 7 in as cast form and after the heat treatment at different annealing temperature has been done. Figure 5.27 (a) and (b) show the microstructures of x = 1 in the as cast and after the heat treatment at T_a = 500°C. As cast sample in Figure 5.27 (a) does not show any sign of crystallization with clear background. All other as cast samples like x = 2, 3, 5 and 7 show similar behavior. But at the annealing temperature of T_{a} = 500°C for the sample x = 1 and 2, it is revealed that T_a = 500^{o}C is sufficient to start the formation of *bcc* Fe-(Si) nanograins but not well defined grains which are embedded in the residual amorphous matrix as clearly presented in Figure 5.27 (b) and 5.28 (a).The grains are agglomerated or in the form of clusters from where exact grain size cannot be ascertained. From Figure 5.28(b), for Nb = 2, it is observed that with increasing annealing temperature, the grain size appears more matured and clearly visible when annealing temperature increased from 500 to 550°C. This is a combined effect of Cu and Nb where, Cu acts as nucleation agent and Nb hinders the grain growth.

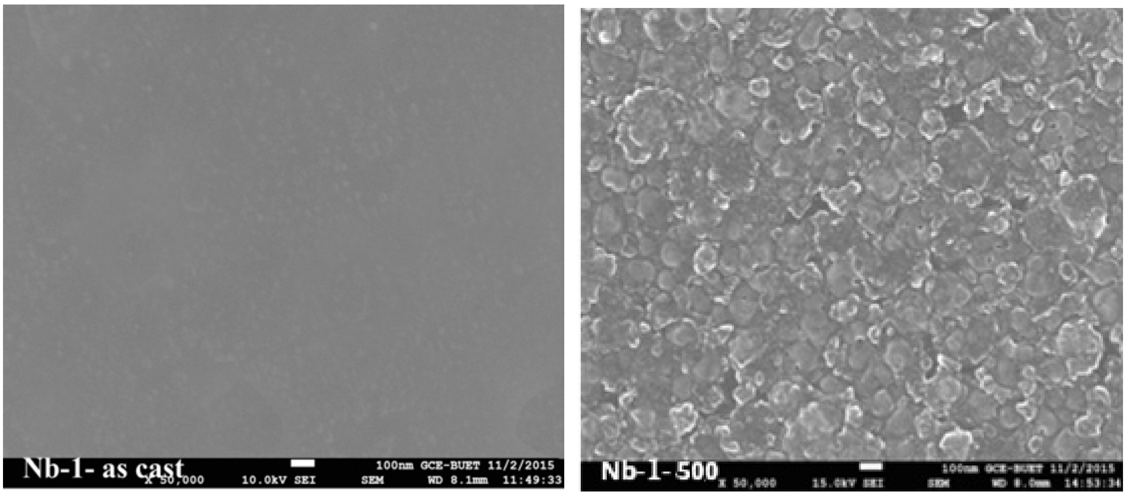

(a) (b)

Figure 5.27: FESEM microstructure of $Fe_{76.5-x}Nb_xCu_1Si_{13.5}B_9$ where x = 1 in (a) as cast and annealed at temperature (b) 500^{o}C.

Figure 5.29(a),(b),(c) represents the microstructure of the sample x = 3. As cast sample distinctly show amorphous state, while annealed sample at T_a = 530°C which is very close to crystallization peak temperature of T_{p1} = 536°C according to our DSC, elegantly display ultrafine grained mustard seed like grains homogeneously dispersed on the remaining amorphous matrix (Figure 5.29(b)). But when annealed at T_a = 550°C as shown in Figure 5.29(c) which is higher than T_{p1} = 536°C clearly shows well developed grains. These grains are highly agglomerated. But the growth of grain size with increasing temperature is perfectly visible. If we compare the grain with Nb content Nb < 3, then it understood that optimum Nb content around 3 is required to have controlled grain growth with uniform distribution throughout the matrix. Probably for this reason the optimum composition of FINEMET alloy contain Nb = 3. From our XRD data we found that at T_a = 550°C grain size was 9 nm which increases 12 nm at T_a = 580°C and 14 nm at T_a = 600°C. It is clearly seen that the microstructure is characterized by a homogeneous, ultrafine grain structure of α-Fe(Si) with grain sizes around < 25 nm and random texture, matrix. The formation of this particular structure is ascribed to the combined effects of elements as α-Cu (which promotes the nucleation of grains) and Nb, and their low solubility in α-Fe(Si)

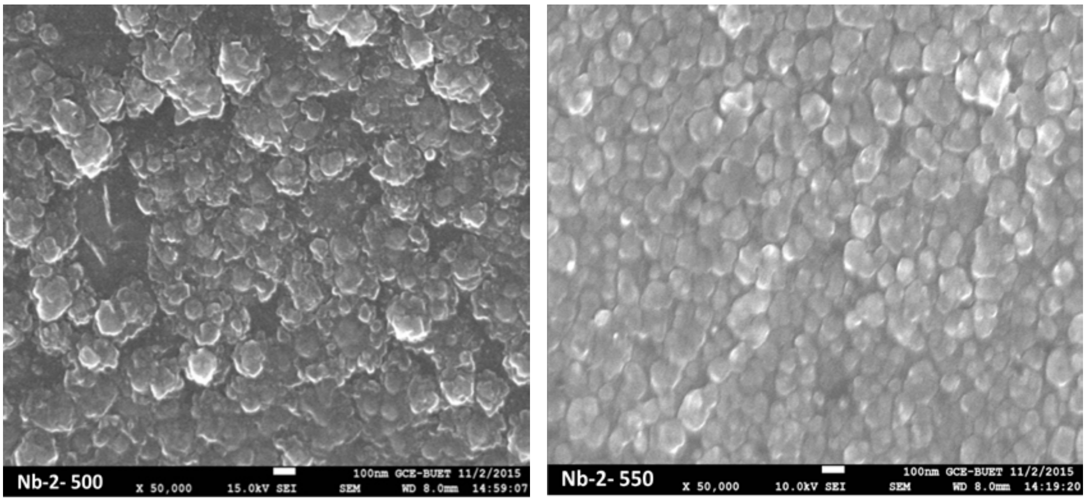

(a) (b)

Figure 5.28: FESEM microstructure of $Fe_{76.5-x}Nb_xCu_1Si_{13.5}B_9$ for x = 2 annealed at temperatures (a) 500^{o}C and (b) 550^{o}C.

[10, 131]. The increase of grain size with increasing annealing temperature may be attributed to the diffusion of silicon into the nano grains. Because of this diffusion effect, the Si content (at.%) increases and hence the grain size. For the sample with maximum grain size we get the maximum Si content and vice versa. Si contents in Fe(Si) nano grains created at different heat treatment conditions have been determined by the abrupt increasing mode. Figure 5.30 shows FESEM images of the sample of x = 5 in as cast and after annealing at T_a = 530, 550 and 580°C. Materials with excellent soft magnetic properties could be obtained by the crystallization of the Fe-Si-B alloys with the addition of Cu and Nb. The addition of Cu and Nb led to the dispersion of

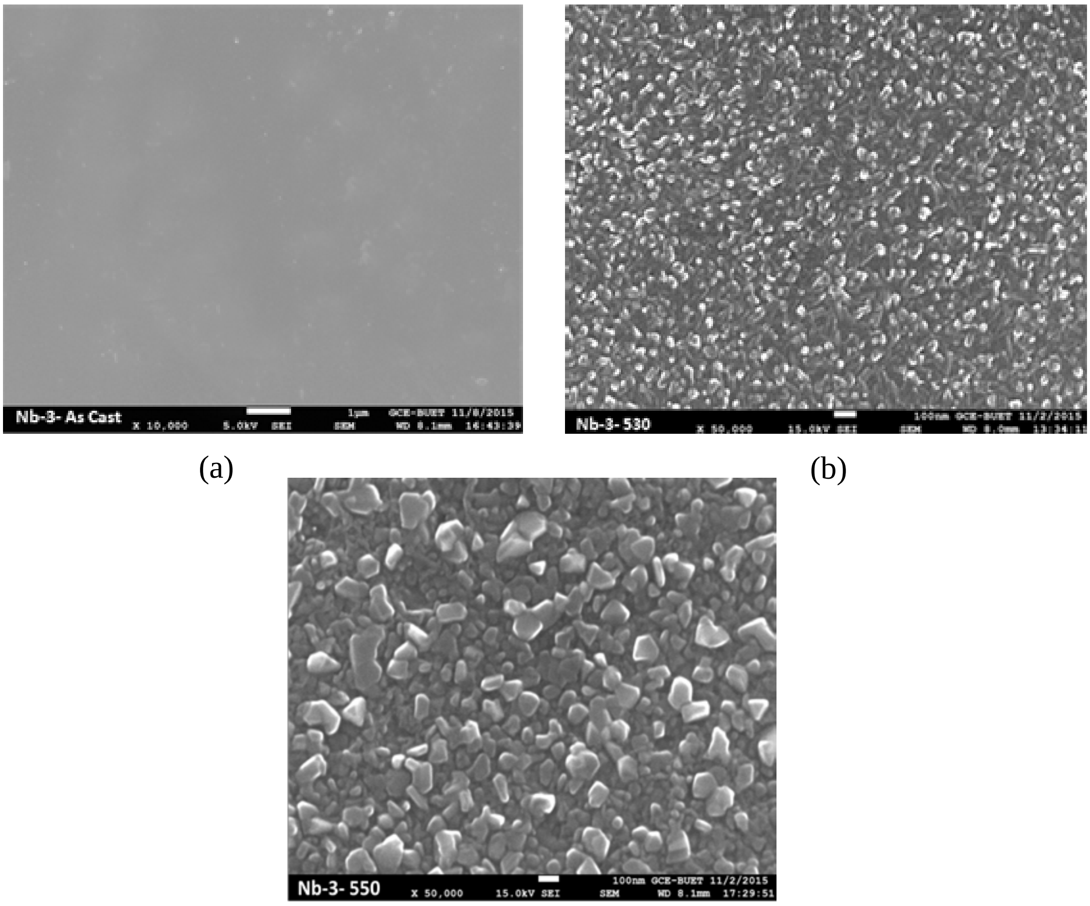

(a) (b)

(c)

Figure 5.29: FESEM microstructure of $Fe_{76.5-x}Nb_xCu_1Si_{13.5}B_9$ where x = 3 in (a) as cast and annealed at temperatures (b) 530°C and (c) 550°C.

ultrafine α-Fe(Si) nano-particles in an amorphous matrix, which averaged out the magnetocrystalline anisotropy energy [15] resulting in high permeability of the FINEMET alloys. It is evidenced from the microstructure that the grain size is slightly reduced compared with the sample with x = 3 which is compatible with XRD data.

The grain size for sample x = 5 is 6 nm and 10 nm at T_a = 550 and 580°C respectively compared with 9 nm and 12 nm for the sample x = 3 at the same annealing temperature, T_a. Figure 5.31 shows the FESEM microstructure of T_a = 650°C. The

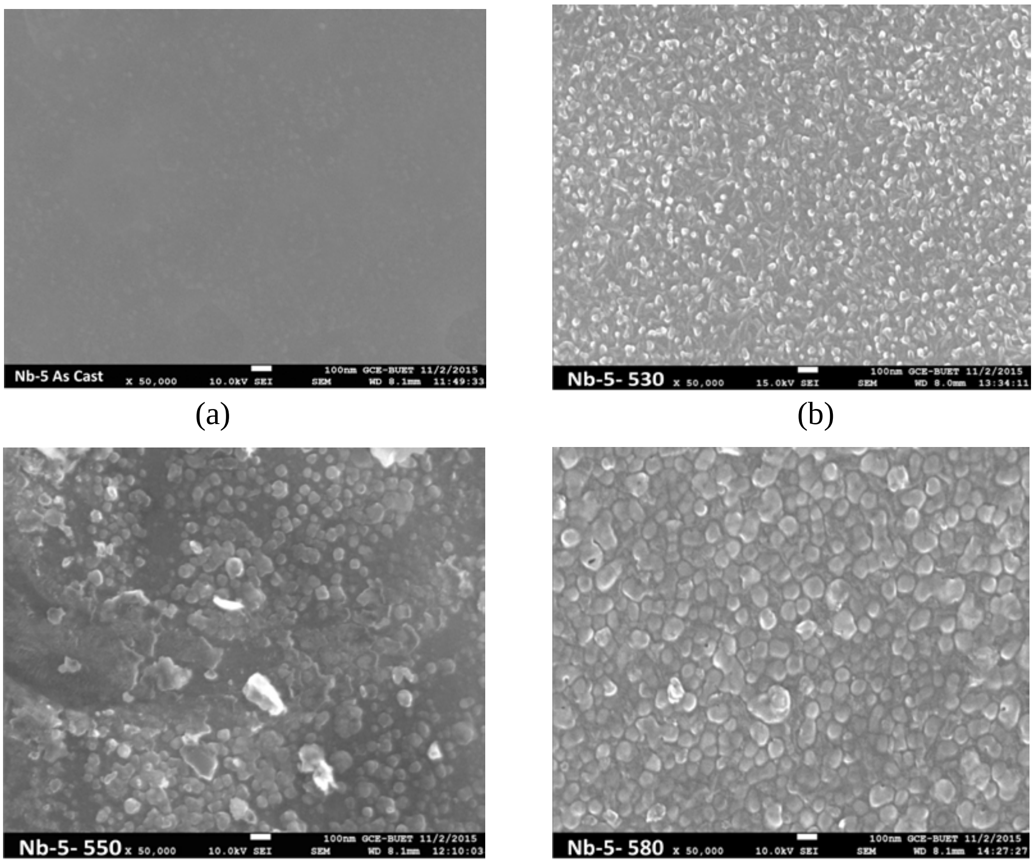

(a) (b)

(c) (d)

Figure 5.30: FESEM microstructure of amorphous $Fe_{76.5-x}Nb_xCu_1Si_{13.5}B_9$ for x = 5 in (a) as cast and annealed at temperatures (b) 530°C, (c) 550°C and (d) 580°C.

of x = 7 in as cast and annealed at T_a = 600 and 650°C. It is observed from Figure 5.31(b), (c) that small crystallites have started developing at T_a = 600°C for the sample with x = 7 while large agglomerates have developed at annealing temperature volume fraction of the grains is not sufficient and the grains are not close enough so that strong magnetic exchange coupling can occur among the nanograins. This has an adverse effect on the magnetization and inparticular permeability of the sample. This is probably due to powerful influence of large amount of grain growth inhibitor Nb = 7. The grain growth was suppressed but to reduce surface energy they are highly agglomerated. The grain size from such microstructure is difficult to determine from FESEM microstructure. If we compared these microstructural feature with XRD data we observe that for the sample x = 7 no crystallization event has taken place up to T_a = 580°C. At temperature only from 600° C slight rising crystalline peak has just

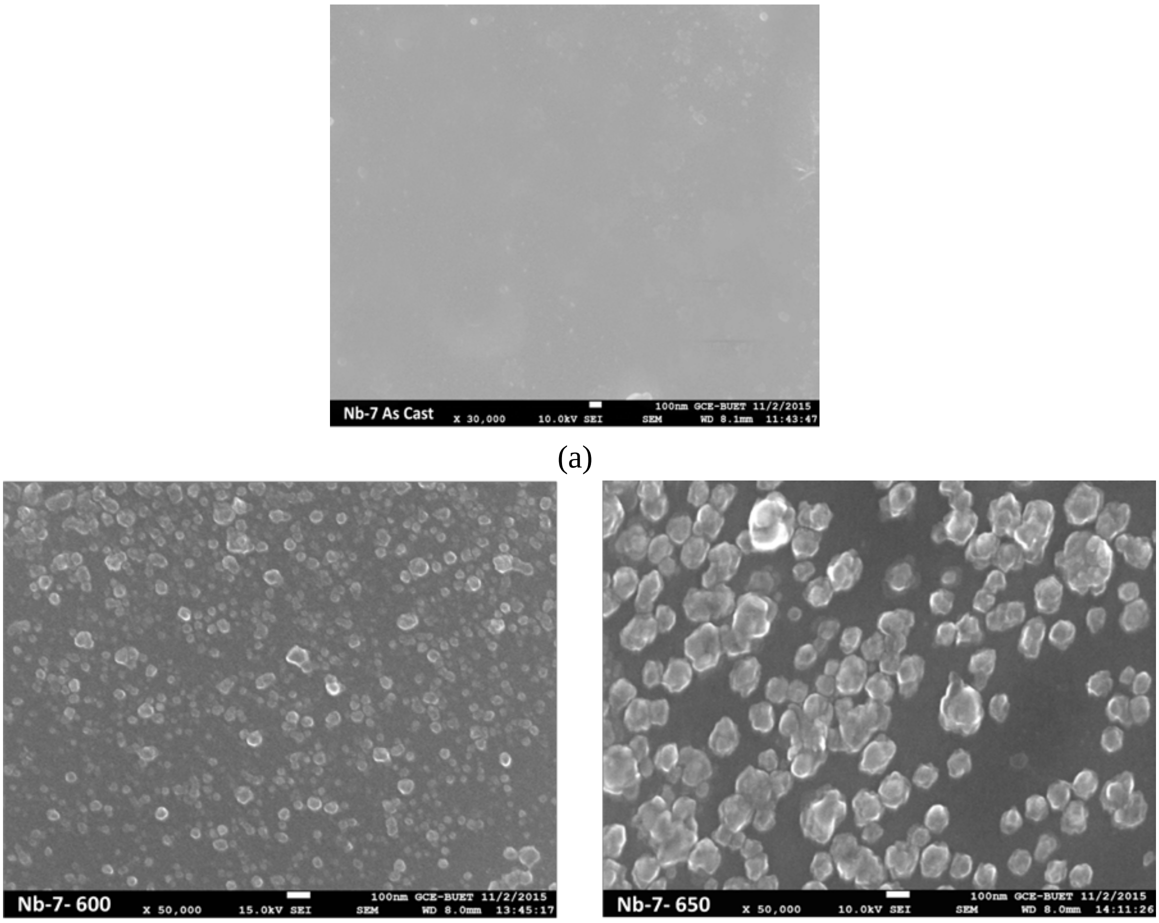

(a)

(b)

(c)

Figure 5.31: FESEM microstructure of amorphous $Fe_{76.5-x}Nb_xCu_1Si_{13.5}B_9$ for x = 7 in (a) as cast and annealed at temperatures (b) 600^{o}C and (c) 650^{o}C.

appeared which was estimated to be around 6 nm as shown in Table 5.11. From XRD data a grain size of 6 nm was estimated for the sample x = 5 at T_a = 550°C which clearly show the grain growth inhibiting power of refractory Nb metal or in general the restricted crystallization behavior of higher Nb content sample.

This implied that the addition of Nb element could effectively suppress the grain growth in the nanocrystalline Fe-based alloy and the effect of Nb on the refinement of grains of the α-Fe(Si) solid solution phase is saturated at a very small amount of Nb [132]. Accordingly to theory, it is necessary to obtain nanocrystalline grains of ~12 nm in order to rotate the magnetic domain easily [133]. The magnetic behavior of soft magnetic nanocrystalline alloys depends strongly on the microstructure formed after the partial devitrification of the melt-spun amorphous ribbons [134].

From the microstructural study it is understood that intermediate concentration of Nb = 3 or little higher appears to be optimum level of addition for appropriation of grain size in the FINEMET nanocrystalline Fe-Si-B based alloys. Around this concentration of Nb, homogenous microstructure with optimum grain size and their distribution is expected to envolve through thermal treatment annealing at a temperature of T_a = 550°C.

Hence, it can be concluded that the addition of appropriate amount of Nb controlled the grain size in the Fe-Si-B-Nb-Cu alloy ribbon consisted of ultrafine crystal grain size of 10-12 nm.

3.2.4 Transmission Electron Microscope (TEM) Image

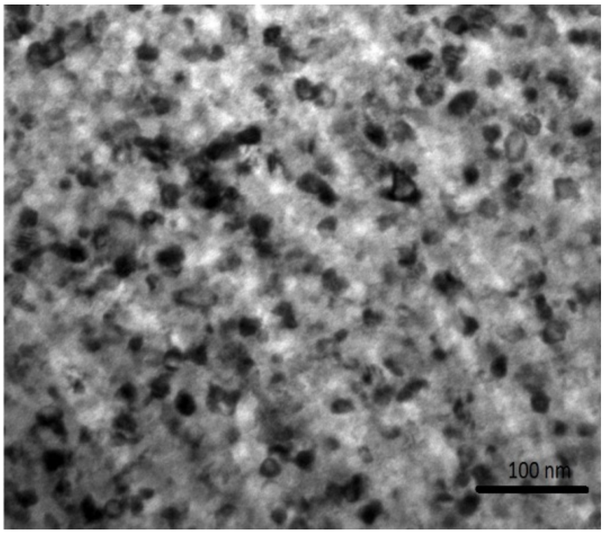

Figure 5.32: TEM image for the sample with composition x = 3 showing uniform distribution of grains.

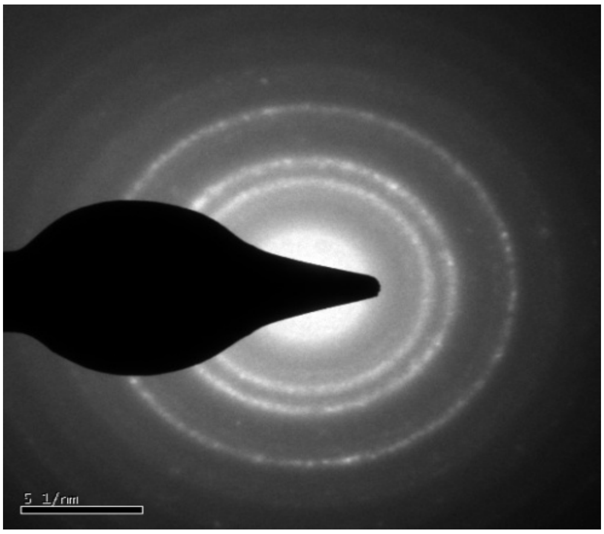

Figure 5.33: Electron diffraction image of $Fe_{76.5-x}Nb_xCu_1Si_{13.5}B_9$, for x = 3.

The microstructure of annealed sample $Fe_{76.5-x}Nb_xCu_1Si_{13.5}B_9$ where x = 3 at 580^{o}C for 30 min has been studied by TEM [102]. The Bright field (BF) image shown in Figure 5.32 confirms nano crystallinity. Some bright spots found by selective area electron diffraction (SAED) pattern of annealed sample shown in Figure 5.33 which is the replica of BF image. Grains found in the bright field image is nominated as *bcc α*-Fe(Si) phase. The grain size of the phase is found to be approximately 13 nm by using Image J software.

5.2.5 Magnetic Field Dependence of Magnetization

Magnetic field dependence of magnetization *M*(*H*) for as cast samples has been measured at room temperature, 300K and at 80K up to *H* = 16000 Oe and presented in Figure 5.34 and Figure 5.35 respectively. A Vibrating Sample Magnetometer (VSM) was used to get the variation of magnetization with applied magnetic field.

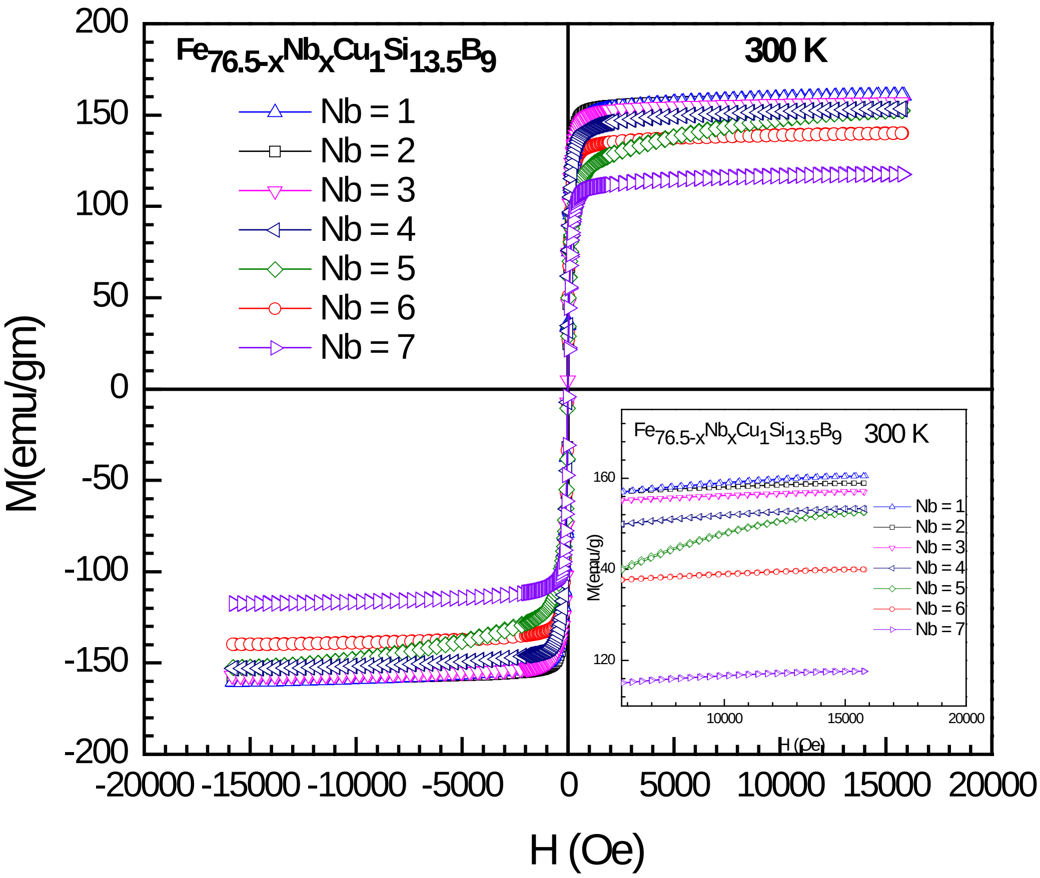

Figure 5.34: Field dependence of magnetization (M-H curve) of $Fe_{76.5-x}Nb_xCu_1Si_{13.5}B_9$ ribbons with x = 1, 2, 3, 4, 5, 6 and 7 at 300K.

From the graphs it is clearly observed that magnetization increases very rapidly with applied field reaching almost saturation value within *H* = 1000 Oe and gradually attains complete saturation at *H* = 16000 Oe. The saturation magnetization (M_s) value depends on Nb content [135]. It is clearly seen that the increasing in Nb content results in decreasing the saturation magnetization, M_s. This decrease of M_s can be

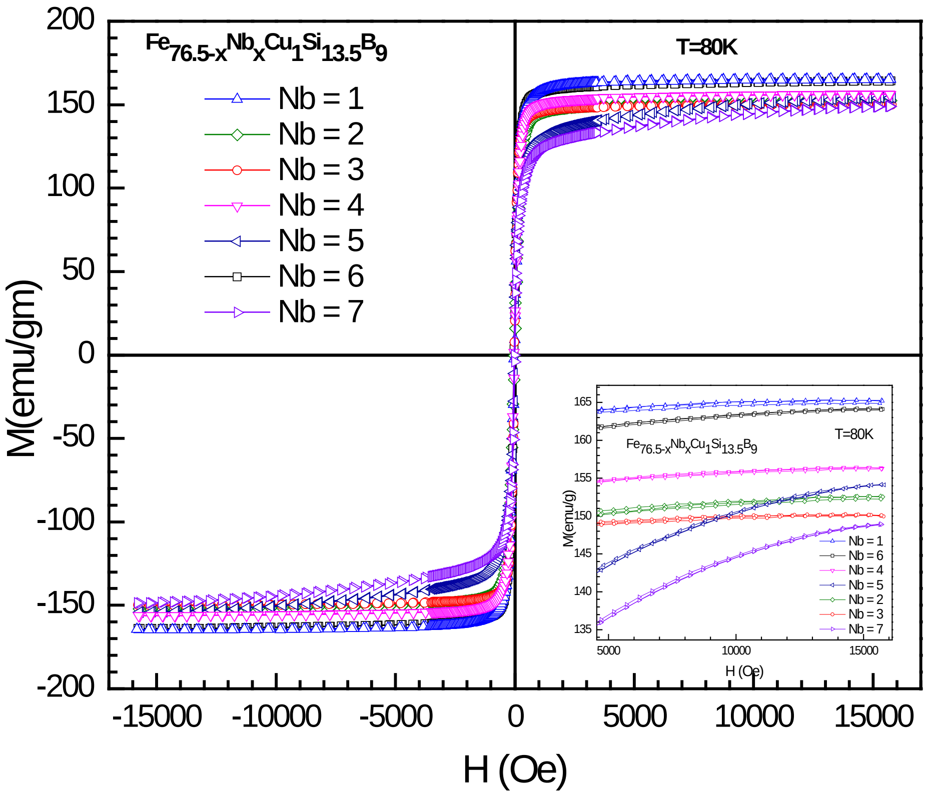

Figure 5.35: Field dependence of magnetization (M-H curve) of $Fe_{76.5-x}Nb_xCu_1Si_{13.5}B_9$ ribbons with x = 1, 2, 3, 4, 5, 6 and 7 at 80K.

attributed to simple dilution of Fe magnetic moment of the alloy matrix due to substitution of nonmagnetic Nb.

There is a large difference of M_s value measured at temperature of T = 300K and 80K. All the samples display ferromagnetic nature at both measuring temperature as evidenced from the saturation magnetizaon value and the S shaped histerisis loop. Saturation magnetization M_s at 300K is always lower than at 80K value which is related to thermal effect of disordering the magnetic spins following blocks spin wave $T^{3/2}$ theory of temperature dependence of magnetization $M(T) = Mo(1-BT^{3/2} - CT^{5/2})$ [135]. The M_s value for the sample with x = 1 at 300K is 159 emu/gm and 165 emu/gm at 80K compared with 118 emu/gm for x = 7 at 300K and 146 emu/gm at

80K respectively. The Table 5.12 shows that M_s monotonically decreases due to increasing the addition of nonmagnetic Nb for both measurement temperature of 300K and 80K. The analysis of complete cycle hysteresis loops revealed that insignificant hysteresis effect have been observed with the manifestation of extremely low value of remanent magnetization, M_r and Coeracivity, *Hc*. It implies that all the studied samples in the as prepared amorphous state are excellent soft ferromagnets.

5.2.6 Temperature Dependence of Magnetization of $Fe_{76.5-x}Nb_xCu_1Si_{13.5}B_9$

5.2.6.1 Temperature Dependent Magnetization and Curie temperature Measurements of $Fe_{76.5-x}Nb_xCu_1Si_{13.5}B_9$ alloy

Temperature dependence of magnetization $M(T)$ is widely used technique to disclose magnetic behavior and crystallization phenomena of a magnetic system provided the crystallized products are ferromagnetic in nature. Since the product of primary and secondary crystallization of these alloy systems are α–Fe(Si) and Fe-B respectively which are both ferromagnetic having well defined phase transition temperature the measurement of $M(T)$ would clarify magnetic as well as crystallization event of this samples understudy. From these measurements, Curie temperature, T_c which is also a fundamental parameter of any magnetic system would easily be discerned. T_c is a basic quantity in the study of magnetic materials. It corresponds to the temperature at which a magnetically ordered material becomes magnetically disordered, *i.e.*, becomes paramagnet. T_C also signifies the strength of the exchange interaction between the magnetic atoms.

From the temperature dependent magnetization M(T) with the application of moderate low field we can find out the T_c of the amorphous or as cast sample along with the evolution of magnetization of a newly crystallized ferromagnetic phase and finally the

T_c value of the new ferromagnetic phase developed through crystallization phenomena of an amorphous magnetic would be determined.

Table 5.12: M_s for as cast sample at room temperature and 80 K of $Fe_{76.5-x}Nb_x$ Cu_1-$Si_{13.5}B_9$ alloys obtained from M-H curve and T_c from $M(T)$ curve.

Content Nb X	***Ms* in emu/gm at RT as cast**	***Ms* in emu/gm at 80 K**	**T_c (^oC)**
1	159	165	410
2	156	161	397
3	152	157	380
4	150	154	369
5	146	150	352
6	143	148	340
7	118	146	323

Nanocrystalline amorphous ribbons of compositions $Fe_{76.5-x}Nb_xCu_1Si_{13.5}B_9$ alloys have been used to measure temperature dependent magnetization $M(T)$ during heating cycle at a heating rate of 5°C/min with constant applied magnetic field of 50 Oe and 500 Oe for the sample x = 2, 5 and x = 1, 3, 4, 6 and 7 respectively which are shown in Figure 5.36, 5.37 and 5.38.

From Figure 5.36 and 5.37which correspond to $M(T)$ curves for the samples x = 2 and x = 5, it is observed that as the temperature increases magnetization decreases slightly upto certain temperature range beyond which an abrupt decrease of magnetization takes place. Magnetization attains a very low value close zero and remains constant upto certain temperature range dependent on Nb content before it starts rising again to higher value. The initial decrease of magnetization and particularly a sudden sharp fall of magnetization is connected with decoupling of magnetic moments due to thermal energy and or decrease of exchange energy. From these M vs T data, the Curie temperature, T_c of the as cast samples has been determined as the point where numerical derivative $\frac{dM}{dT}$ attains its maximum value. At the Curie temperature the thermal energy overcomes the magnetic ordering or the exchange energy resulting in a phase transition from ferro-para magnetic at $T = T_c$ of the amorphous state. For the sample x = 2 and 5, T_c values have been found to be 397 and 352°C respectively.

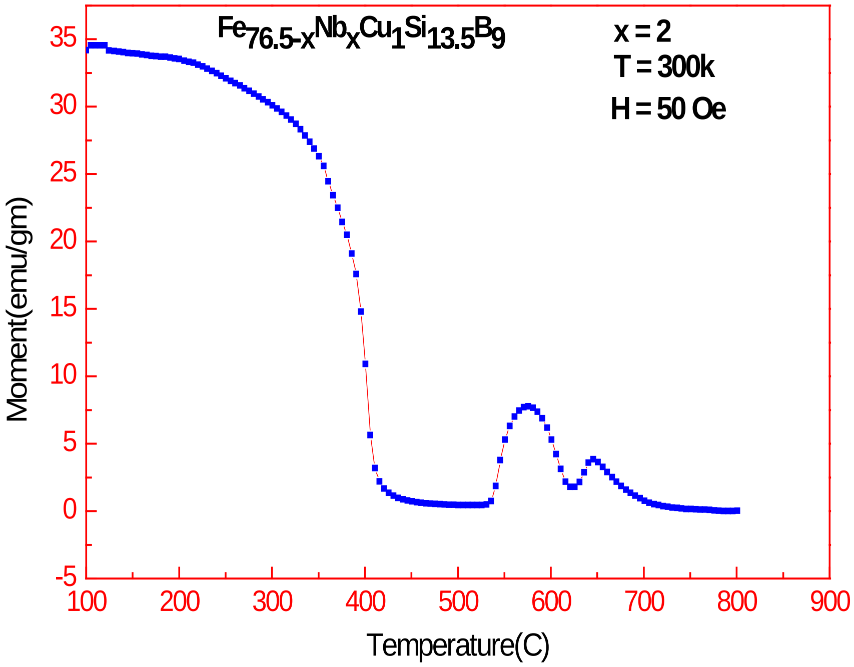

Figure 5.36: Temperature dependent magnetization of $Fe_{76.5-x}Nb_xCu_1Si_{13.5}B_9$ for x =2.

It is understood from the measurement that T_c decrease with the increase of Nb content. One interesting thing we learn from this measurement that inspite of chemical and structural disorder, ferromagnetic metaglasses have well defined magnetic ordering temperature and becomes completely magnetic disorder at $T = T_c$. It is observed from both the $M(T)$ curves that from the temperature above T_c until T = 538 and 600°C for x = 2 and 5 respectively magnetization value of both the samples is nearly zero since they are paramagnetic in that temperature range. At temperature

temperature above *T* = 538 and 600°C for the sample x = 2 and 5, the sudden rise of magnetization of these two samples is associated with the onset of crystallization of *α*-Fe(Si) ferromagnetic phase from the remaining amorphous matrix. The magnetization of this newly involved ferromagnetic phase rises fast as the temperature increases.

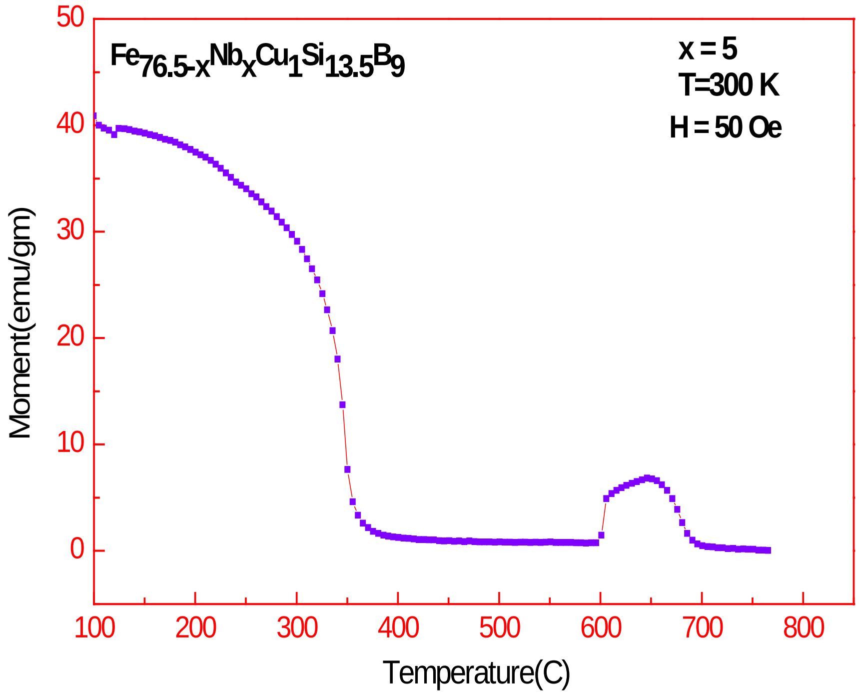

Figure 5.37: Temperature dependent magnetic moment of $Fe_{76.5-x}Nb_xCu_1Si_{13.5}B_9$ for x = 5

This may be attributed to enhanced volume fraction of crystallized *α*-Fe (Si) phase. The magnetization increases and passes through a maximum beyond which it again decreases to a very low value [21]. The decrease of magnetization, *M* after passing through the maximum is connected to the temperature dependence of magnetization of *α*-Fe(Si) nanocrystalline phase that undergoes a FM-PM phase transition of *α*-Fe(Si) phase at *T*= 600 and 660° C for x = 2 and 5 sample respectively. The curie temperature of *α*-Fe(Si) may very dependent on Si content of the phase which ranges from 18 to 25% Si. Niobium, Nb being an refractory metal controls the segregation and diffusion of Si from amorphous matrix to the α-Fe(Si) nanograins. The *α*-Fe(Si) nanocrystalline phase have been confirmed from XRD pattern after annealing at T_a = 600°C (Table 5.11) and at different annealing temperature described in section 5.2.2. This is noticed that onset of crystallization of *α*-Fe (Si) phase shifts to higher temperature as the Nb content increases from x = 2 to x = 5. This clearly indicates the thermal stability of Nb addition against crystallization.

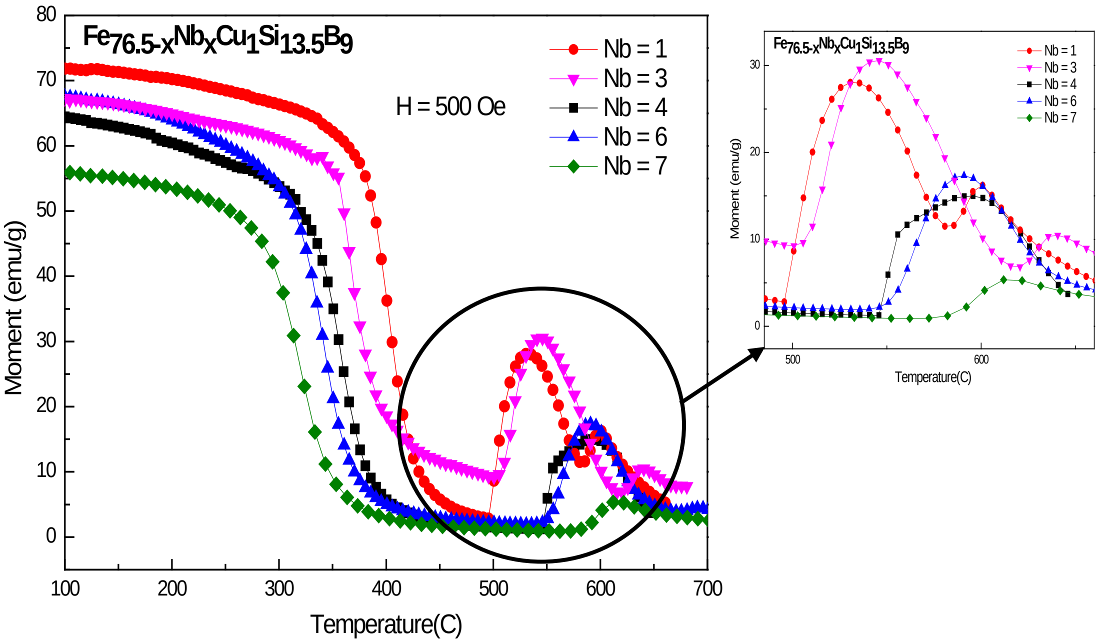

Figure 5.38: Temperature dependent magnetic moment of Fe$_{76.5-x}$Nb$_x$Cu$_1$Si$_{13.5}$B$_9$ for x = 1, 3, 4, 6, and 7.

The magnetization again remains constant beyond temperature 660° C for x = 5 due to the paramagnetic nature of this sample. But sample x = 2 displays different scenario where again an increase of *M* is observed above 625°C attain a maximum value at around *T* = 650°C and thereafter decrease gradually to a very low value above *T* = 700°C corresponding to a new paramagnetic state. The second phase transition above *T* = 650°C may be associated with a magnetic phase of Fe-B which is not suitable for soft magnetic material having high magneto crystalline anisotropy. This is to note that evolution of Fe-B is favorable only at high activation energy which is not found always. But our interest is to be with the α-Fe(Si) phase which is required for soft magnetic properties. For this reason we generally anneal FINEME sample at temperature below the onset of crystallization of Fe-B phase *i.e.* below 650°C. The evolution of Fe-B phase for sample x = 2 is connected to low content of Nb with less thermal stability and less activation energy which gives favorable environment for the nucleation of Fe-B phase.

Figure 5.38 shows the $M(T)$ curves for the sample x = 1, 3, 4, 6 and 7 measured with a constant magnetic field of H = 500 Oe up to temperature of T = 700°C. It is clearly demonstrated in the $M(T)$ curves that M decreases with temperature and a sharp fall of M takes place at a temperature towards zero corresponding to T_c of the corresponding sample with varying Nb contents [136]. It is observed that T_c value of the samples decreases gradually with increasing Nb content due to weakening of exchange interaction concomitant decreasing magnetization of the studied samples. The onset temperature of crystallization of α-Fe(Si) nanocrystalline phase shifts to higher temperature range as the Nb content increases. After passing through a maximum value of magnetization M, the samples undergo a magnetic phase transition from ferromagnetic to paramagnetic (FM - PM) state of α-Fe(Si) at a temperature at or above 600°C which again depends on Nb contents. As the Nb contents exceeds x > 3, the FM-PM phase transition temperature shifts to higher temperature which has already been shown for sample x = 5 (Figure 5.37). This may be due to stoichiometric deviation of α-Fe(Si) composition.

It is also interesting to observe that sample with low Nb content such as x = 1 and 3 has displayed the evolution of Fe-B phase after the nucleation of α-Fe(Si) phase at $T \geq 630$°C which is concomitant with x = 2 as described before. Therefore the effect of Nb content on the crystallization behavior of conventional FINEMET alloy is well understood that Nb retards crystallization event, restricts grain growth, controls the evolution of detrimental iron-boride phase for magnetic softening and enhances the thermal stability of the alloy system against crystallization. Therefore the choice of Nb content as grain growth inhibitor and thermal stability should be critically decided.

5.2.6.2 Temperature Dependent Magnetization Measurements of $Fe_{76.5-x}Nb_x Cu_1Si_{13.5}B_9$ alloy During Heating and Cooling

Figure 5.39 and 5.40 display *M*(*T*) curves measured with *H* = 500 Oe up to temperature *T* = 700°C during heating and cooling cycle of two sample with x = 3 and 7. It is observed for Figure 5.39 there is a distinct difference between *M*(*T*) of heating and cooling cycle. During cooling, magnetization M sharply rises to high value when the temperature decreases from 700°C to lower temperature. At 700°C the sample is a paramagnet. During cooling, the sudden rise of temperature necessarily indicates a magnetic phase transition from paramagnetic state to ferromagnetic (PM - FM) one. This phase transition is obviously connected with α-Fe(Si) with a T_c value comparable with the measurement of during heating above 600°C. Below 600°C during cooling the magnetization *M* becomes saturated and sluggishly increases until lower temperature of 100°C. It is worth noting that the magnetization gets little higher value than during heating cycle. This may be attributed to fully crystallization of α-Fe(Si) nanocrystalline phase from the base matrix of FINEMET composition. It is also seen from the *M*(*T*) curve that it belongs to a state of single magnetic phase, *i.e.* α-Fe(Si). This magnetic state is irreversible, which means that multiple cycling of heating and cooling, *M*(*T*) curve will remain the same since the magnetization of nanocrystalline α-Fe(Si) magnetic phase is completely saturated embedded on otherwise remaining nonmagnetic amorphous matrix.

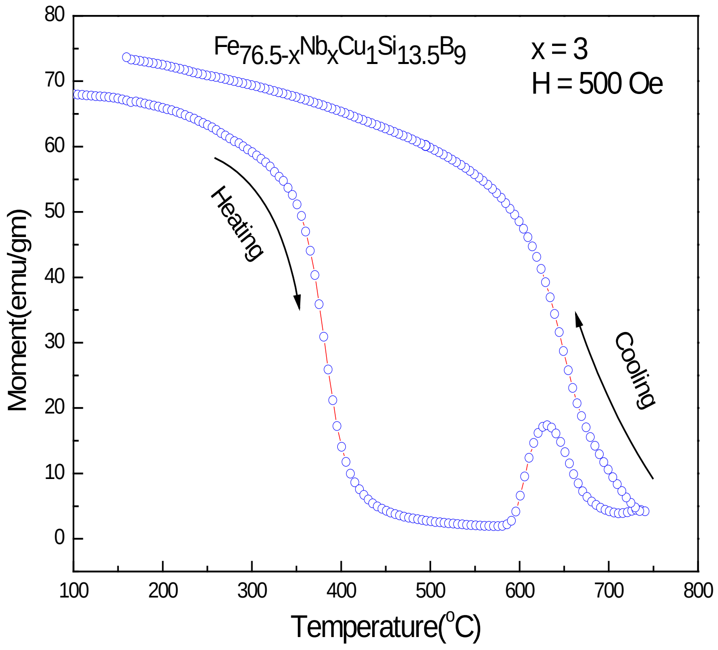

Figure 5.39: Temperature dependent saturation magnetization of amorphous $Fe_{76.5-x}Nb_x$ Cu_1 $Si_{13.5}B_9$ ribbons x = 3 with an applied field *H* = 500 Oe during heating and cooling.

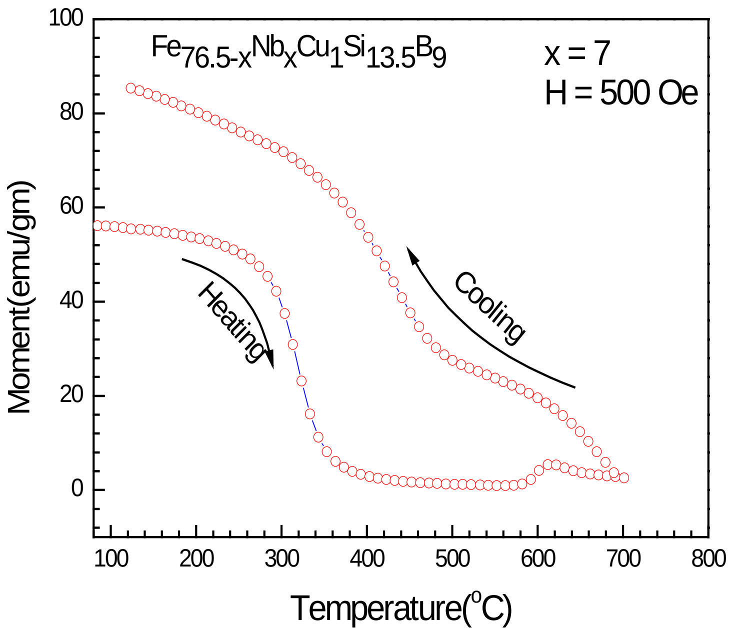

Figure 5.40: Temperature dependent saturation magnetization amorphous $Fe_{76.5-x}Nb_xCu_1$ $Si_{13.5}B_9$ ribbons x = 7 with an applied field *H* = 500 Oe during heating and cooling.

Figure 5.40 demonstrates thermomagnetic curve *M*(*T*) of sample with x = 7 during heating and cooling. During cooling, the magnetization M increases slowly corresponding to a magnetic phase transition of α-Fe(Si) nanocrystalline phase around 650°C.

The phase transition appears to be smeared and diffused due to lacking of matured nanocrystalline α-Fe(Si) phase with no well-defined stoichiometric composition. As temperature decreases, M increases gradually and then become flattened around 500°C. Because of powerful inhibiting nature of high amount of Nb with x = 7, the sample encounters enormous impediments for the growth of α-Fe(Si) ferromagnetic nano phase which results in lower value of magnetization. After T = 500°C again magnetization starts rising sharply until T = 350°C and then gradually levels off. This feature is obviously connected with another magnetic phase transition at temperature around 450°C of the remaining amorphous matrix which still contains substantial amount of magnetic phase. This sample has high niobium content, Nb = 7 which restricted the growth of sufficient amount of α-Fe(Si) even at high temperature during heating up to 700°C. This phase transition around 450°C is also diffused. There is distribution of Curie temperatures T_c of this amorphous phase as well as T_c of α-Fe(Si) phase around 650°C which clearly demonstrated in FINEMET alloy with x = 7. It is learnt from this study that nanocrystalline grain growth inhibitor such as Nb with very high content is not appropriate for development of soft magnetic FINEMET alloys.

The large differences in *M*(*T*) curves between the heating and cooling cycle clearly shows the effect of temperature and crystallization behavior of FINEMET type of alloys [136, 137]. The heating curves of these two samples are not elucidated here in detail because they were well explained in Figure 5.38 earlier.

5.2.8 Measurement of Permeability

5.2.8.1 Real Part of Permeability of $Fe_{76.5-x}Nb_xCu_1Si_{13.5}B_9$

Permeability of a magnetic material is an extrinsic property which can be tailored through appropriate control of material processing parameters and subsequent thermal treatment. Amorphous materials are very sensitive to thermal treatment in particular to annealing treatment since they are in metastable state. Permeability or coercivity which are inversely related are the important parameters for the evalution of any soft magnetic materials. The prime criteria of soft magnetic materials demand either very high permeability or very low coercivity. These demands can only be fulfilled when anisotrophy energy and magnetoelastic energy becomes extremely low tending towards zero. These demands can be satisfied when the FINEMET types of alloys are annealed close to their primary crystallization temperature for sufficient time necessary for the evolution of nanometric size of the α-Fe(Si) grains of ≈10 nm. These magnetic nanograins when they are sufficient in number and very close to each other strong exchange coupling takes place between them through the remaining thin amorphous interface. Annealing temperature should be carefully choosen from DSC experiment or thermomagnetic measurement so that it is always just above the primary crystallization temperature and obviously below the secondary crystallization temperature to avoid any detrimental Fe-B phase formation.

In our studied system $Fe_{76.5-x}Nb_xCu_1Si_{13.5}B_9$ we will observe that high permeability and low magnetic loses have been manifested as a result of annealing at different annealing temperatures from where an optimum composition has been established.

The high initial permeability and extremely low magnetic losses of the optimized nanocrystalline alloys are due to the drastic reduction in the local magnetocrystalline anisotropy which is randomly averaged out by the exchange interactions due to the formation of nanometric grains smaller than the ferromagnetic exchange length and dramatic decrease of magnetostatic energy due thermal annealing.

Figure 5.41, 5.42 and 5.43 show the frequency dependence of the real part of initial permeability of the $Fe_{76.5-x}Nb_xCu_1Si_{13.5}B_9$ alloys in as cast condition and annealed at temperature of T_a = 500 and 550°C. The annealed sample for which there is a strong magnetic coupling between the nanometric grains has high value of permeability. The coupling between the nanograins mediated by the amorphous matrix is of paramount importance for the magnetic softening of the materials, which depends not only on the nanometric grains but more importantly on the composition, thickness and amount of intervening amorphous phase.

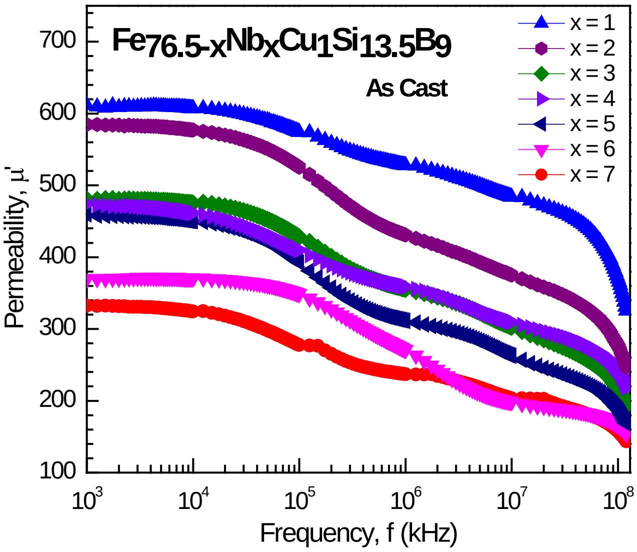

Figure 5.41: Frequency dependent real part of permeability of $Fe_{76.5-x}Nb_xCu_1Si_{13.5}B_9$ for x = 1, 2, 3, 4, 5, 6 and 7.

It is a prerequisite for the ferromagnetic grains to be strongly exchange coupled to maintain good soft magnetic properties. Therefore, optimization of magnetic properties of the nanocrystalline alloys need more detailed study on the effect of heat treatment as a function of annealing temperature and time [138]. The values of permeability at different heat treatment conditions are represented in the following

Figure 5.42 and 5.43. For as cast sample as shown in Figure 5.41 it is observed that the value of permeability of $Fe_{76.5-x}Nb_xCu_1Si_{13.5}B_9$ is dependent on Nb content and maximum value was obtained for x = 1 composition followed by x = 2, 3, 4, 5, 6 and minimum for x = 7, whereas for T_a = 500 and 550^{o}C maximum value of permeability was found for x = 3 followed by x = 4, 2, 1, 5 and minimum value for x = 6 and 7 respectively.

It is observed that the maximum value of real part of permeability, μ′ of the as cast amorphous samples is maximum for x = 1 and then decreasing with increasing Nb content. It is obvious as the samples have not undergone any thermal treatment and no crystallization for the growth of magnetic α-Fe(Si) nanograins has taken place. Therefore the magnetic permeability is completely dependent on iron content only which is strongly magnetic and its concentration decreases at the Nb content increases. The scenario is quite different when annealing of these samples at T_a = 500 and 550°C have been done. In the annealed samples maximum μ' has been found in sample with x = 3 followed by x = 4 and x = 2. It means that concentration of Nb plays an important role in tailoring the real part of permeability as Nb controls the crystallization phenomena and grain growth of α-Fe(Si) nanograins including its volume fraction. These two events together play a vital role in minimizing the average anisotropy energy of the sample brings it towards zero. More over thermal treatment of annealing again reduces substantially the magnetoelastic energy by relieving internal stress developed during extremely rapid cooling of 10^6Ksec^{-1}. As a result of the low anisotropy energy as well as reduced magnetoelastic energy, domain wall motion and spin rotation becomes very easy resulting in very high permeability. But when the Nb content becomes high *i.e.* Nb > 4, again permeability rapidly reduces to very low value. This is because higher obstacles are imparted by refractory metal Nb having higher thermal stability to retard not only the formation of α-Fe(Si) nanograins, but also reduces the volume fraction of α-Fe(Si) nanograins weakening the exchange coupling between magnetic nanograins. This results in low permeability of the higher Nb content samples. Therefore the role of Nb in the crystallization process and soft magnetic properties inparticular the permeability is clearly demonstrated through the experimental work. It is also observed that higher the permeability lower is the frequency range for its stability. It means that μ' falls rapidly to low value at lower frequency due to ferromagnetic resonance for sample having high permeability. But low permeability samples have constant μ' up to very high frequency range *i.e.* their frequency stability is high. According to Snoek's law, $f_r\,\mu'$ = constant where f_r is the resonance frequency and μ' is the real part of permeability. This means that high frequency and high permeability cannot work together. It is also

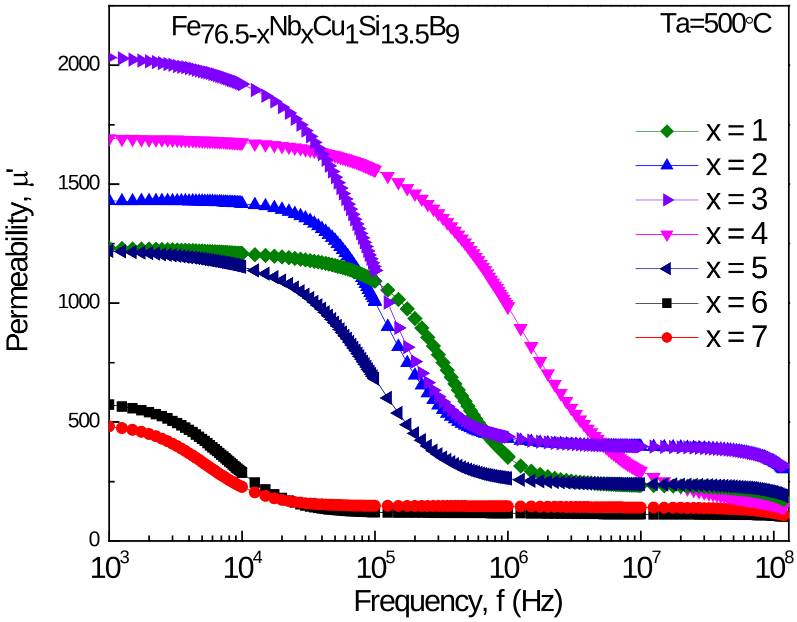

Figure 5.42: Real part of the permeability as a function of frequency of $Fe_{76.5-x}Nb_xCu_1Si_{13.5}B_9$ for various Nb content.

observed from Figure 5.41, 5.42 and 5.43 that permeability has increased from the value of ≈ 500 to 8500 for sample with x = 3 in the amorphous condition to annealed condition at T_a = 550°C. Similar is the situation for other samples which is entirely due to nanocrystallization of the FINEMET type of amorphous ribbons in this study. It is observed from Figure 5.42 and 5.43 that μ' is much higher for samples annealed at T_a = 550°C than annealed at 500°C. At annealing temperature of T_a = 500°C crystallization of the amorphous samples have not been completed since this temperature is little lower than the crystallization peak temperature of the studied samples. Therefore it may be concluded that a temperature around 550°C appears to be closely related to the optimization temperature of annealing of the samples, although it may vary slightly with Nb content. The sample with x = 3 appears to be a good sample for soft magnetic properties. The value of permeability has a good agreement with magnetization value volume fraction of α-Fe(Si) magnetic nanograins decrease of magnetocrystalline anisotropy energy and the grain size of the composition.

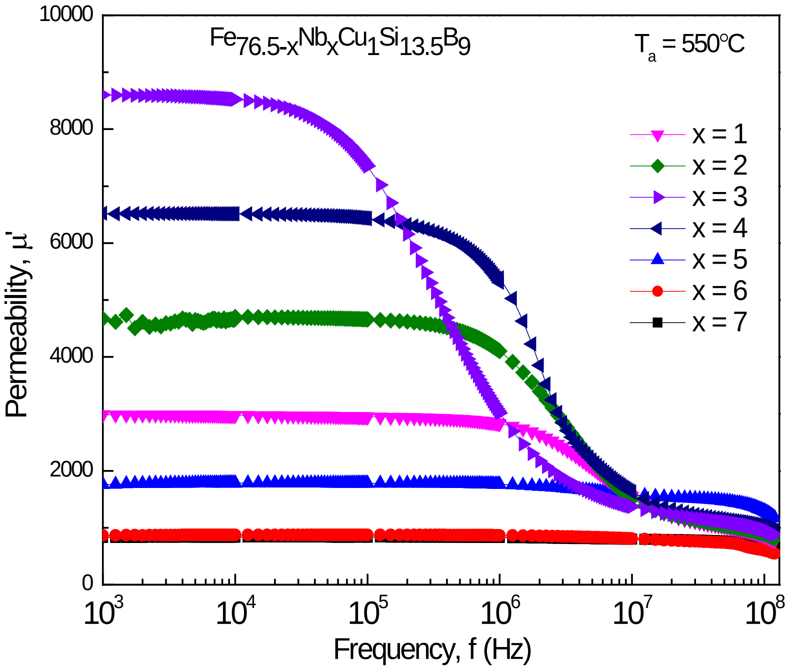

Figure 5.43: Real part of the permeability as a function of frequency of $Fe_{76.5-x}Nb_x$ $Cu_1Si_{13.5}B_9$ for different Nb content.

5.2.8.2 Frequency Dependence of Complex Permeability of $Fe_{76.5-x}Nb_xCu_1Si_{13.5}B_9$

The FINEMET type of alloys, now-a-days plays an important role as soft magnetic materials with very high permeability. In order to correlate the microstructural features with soft magnetic properties of the alloys under study, initial magnetic permeability of the toroidal shaped samples annealed at different temperatures were measured at room temperature with an a.c. field of H = 0.1 Am^{-1} and frequency ranging from 1 KHz to 10000 KHz using an impedance analyzer. Complex permeability, μ can be written as equation (2.32)

$$\mu = \mu' - i\mu''$$

where, μ' and μ'' are real and imaginary part of the permeability respectively.

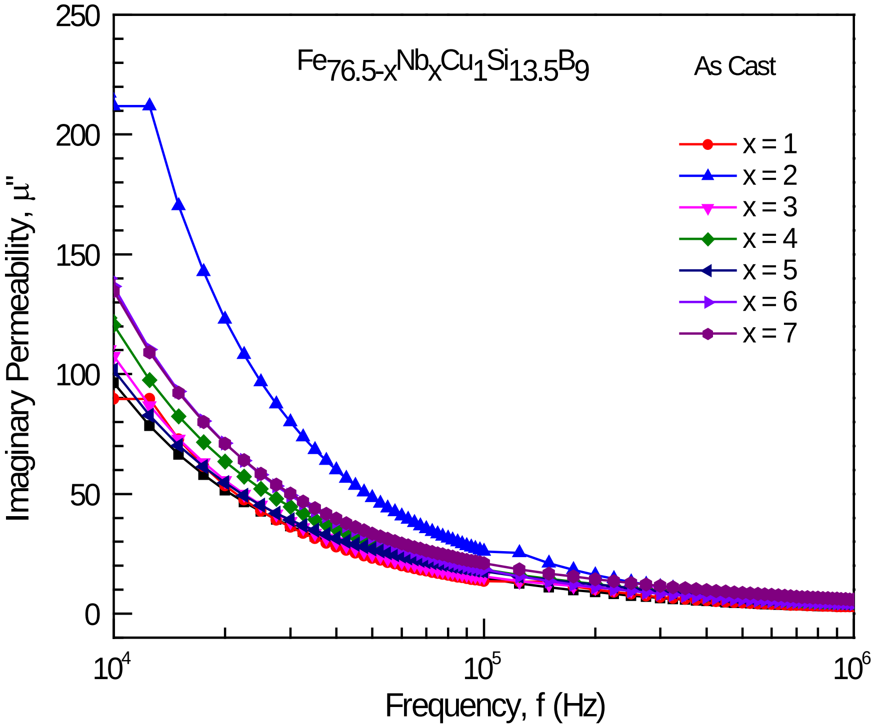

Figure 5.44: Frequency dependent imaginary part of permeability of $Fe_{76.5-x}Nb_xCu_1$ $Si_{13.5}B_9$ alloys at as-cast samples.

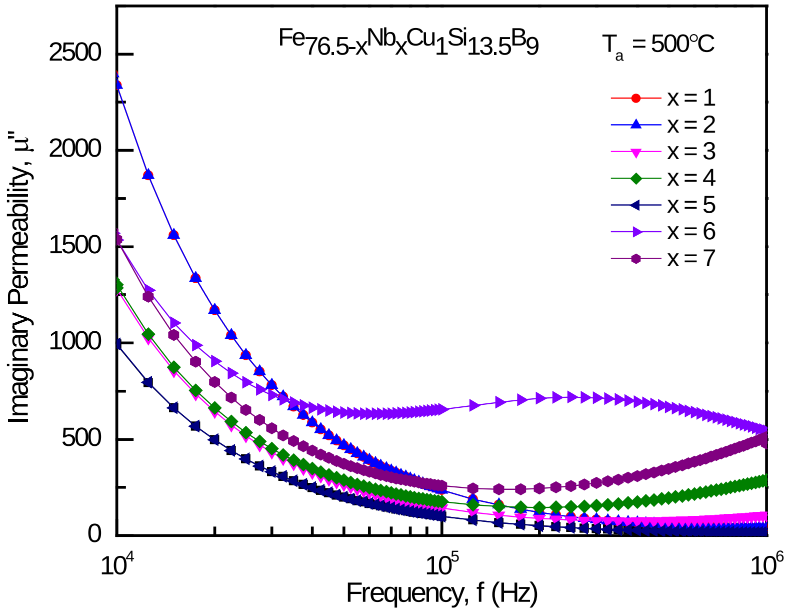

Figure 5.45: Frequency dependent imaginary part of permeability of $Fe_{76.5-x}Nb_xCu_1Si_{13.5}B_9$ alloys annealed at 500^0C.

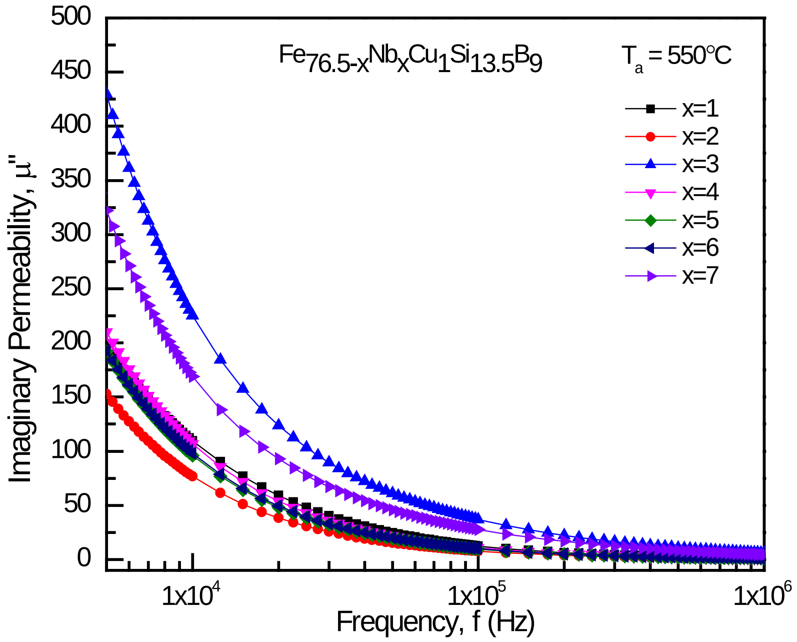

Figure 5.46: Frequency dependent imaginary part of permeability of $Fe_{76.5-x}Nb_xCu_1Si_{13.5}B_9$ alloys annealed at 550^0C.

In Figure 5.44 , 5.45 and 5.46 the frequency dependence of imaginary part of permeability μ'' up to 10000 KHz is presented for the as cast and the samples x = 1, 2, 3, 4, 5, 6 and 7 annealed at annealing temperatures of 500°C and 550°C respectively. The general characteristic of the curves is that μ'' decreases with frequency and attains a minimum value at higher frequency. Imaginary part of permeability represents the loss component of magnetic materials. The materials with lower value of μ'' are suitable for applications for device fabrication. It is observed that annealed sample at T_a = 550°C have low value of μ'' compared with the sample annealed at T_a = 500°C together with high value of real part of permeability as shown in Figure 5.42 and 5.43 and discussed earlier. The magnetic loss tangent, $\tan\delta = \frac{\mu''}{\mu'}$ is reasonably low for samples annealed at T_a = 550°C and therefore suitable from applications point of view.

5.2.8.3 Frequency Dependent Loss tangent measurement

Loss tangent of the composition $Fe_{76.5-x}Nb_xCu_1Si_{13.5}B_9$ has been calculated from the permeability measurement and shown in the Figure 5.47, 5.48 and 5.49 for as cast and annealed at T_a = 500 and 550°C respectively. For the annealing temperature of 500°C, the grain size is smaller but the intergranular distance is large and hence the magnetic coupling between the nanograins is weak which results a lower value of permeability and high loss tangent [139,140]. For the higher annealing temperatures at T_a = 550°C the permeability becomes high which may be attributed to the formation of sufficient amount of α-Fe(Si) nanograins having strong magnetic coupling between the nanometric grains. But annealing at very high temperature for long time has an effect of induced anisotropy which reduces the value of μ'' significantly [141].

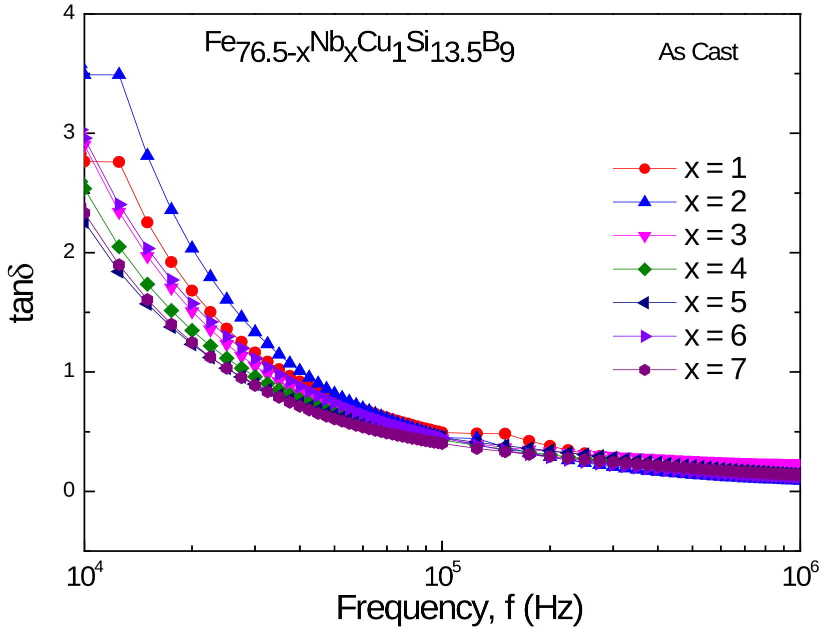

Figure 5.47: Frequency dependent loss tangent of $Fe_{76.5-x}Nb_xCu_1Si_{13.5}B_9$ alloys in as-cast condition.

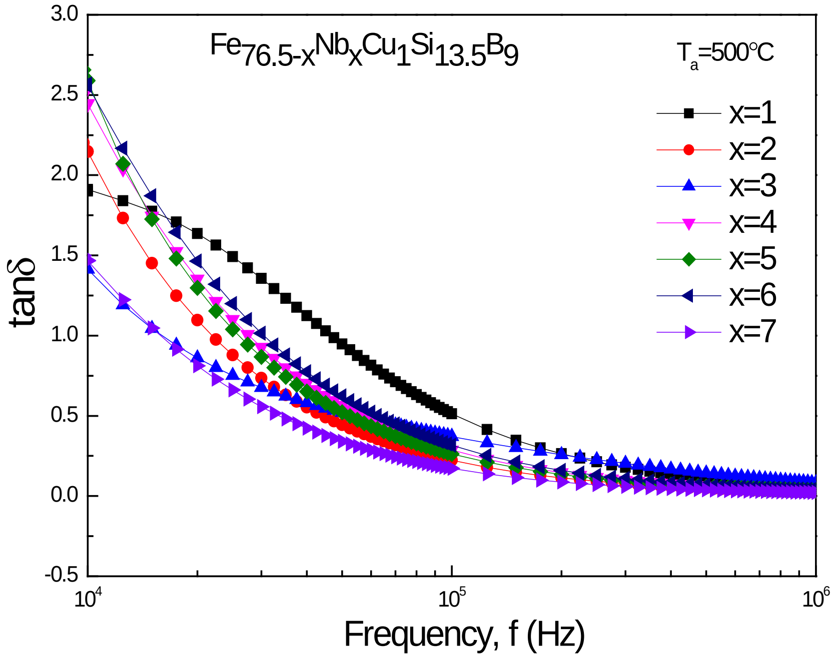

Figure 5.48: Frequency dependent loss tangent of $Fe_{76.5-x}Nb_xCu_1Si_{13.5}B_9$ alloys annealed at 500^0C.

It is observed from Figure 5.48, 5.49 and 5.50 that with increasing annealing temperature, value of red $\tan\delta$ reduces goes down to very small value at higher frequency around 10000 KHz. The loss tangent $\tan\delta$ should be as low as possible from the applications point of view for magnetic materials. The value of $\tan\delta$ is reasonably small for high permeability materials annealed at T_a = 550°C since $\tan\delta = \frac{\mu''}{\mu'}$. It is also evidenced that sample with x = 3, having very high μ' and low μ'' definitely have low value of tanδ which may have found suitable application as soft magnetic material.

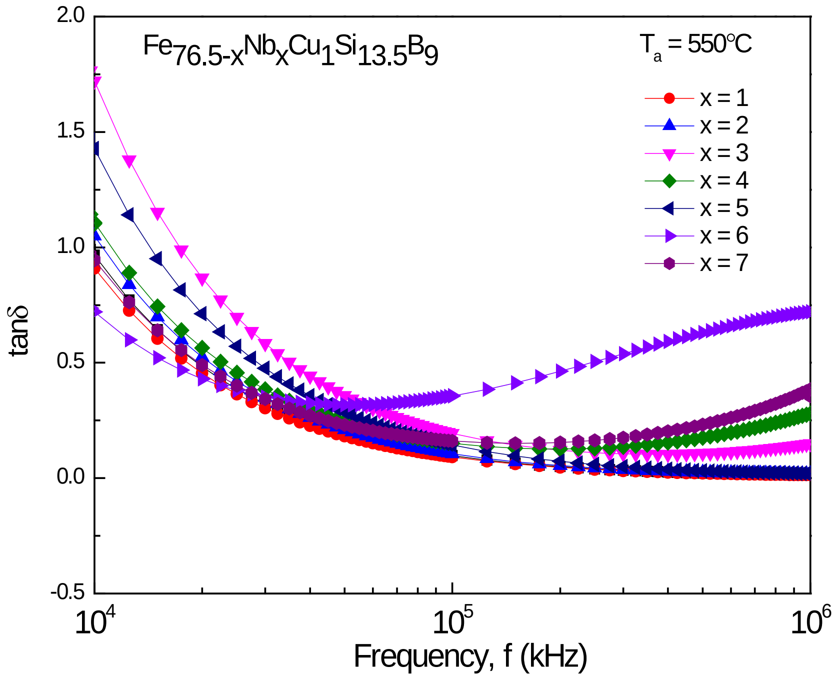

Figure 5.49: Frequency dependent loss tangent of $Fe_{76.5-x}Nb_xCu_1Si_{13.5}B_9$ annealed at 550°C.

The frequency dependence of real and imaginary components of complex permeability reflects the power loss due to the eddy currents and hysteretic response [142].

5.2.9 Analysis of Mössbauer Spectroscopy

The Mössbauer spectra recorded at room temperature on $Fe_{76.5-x}Nb_xCu_1Si_{13.5}B_9$ samples with different Nb contents. One observes the magnetic sextets what-ever the silicon content is, but the hyperfine structures are strongly silicon content dependent Figure 5.50(a) -(d) show the spectra for the $Fe_{76.5-x}Nb_xCu_1Si_{13.5}B_9$ for x = 1. The spectrum clearly decomposed into two, as expected for the stoichiometric Fe-Si alloy.

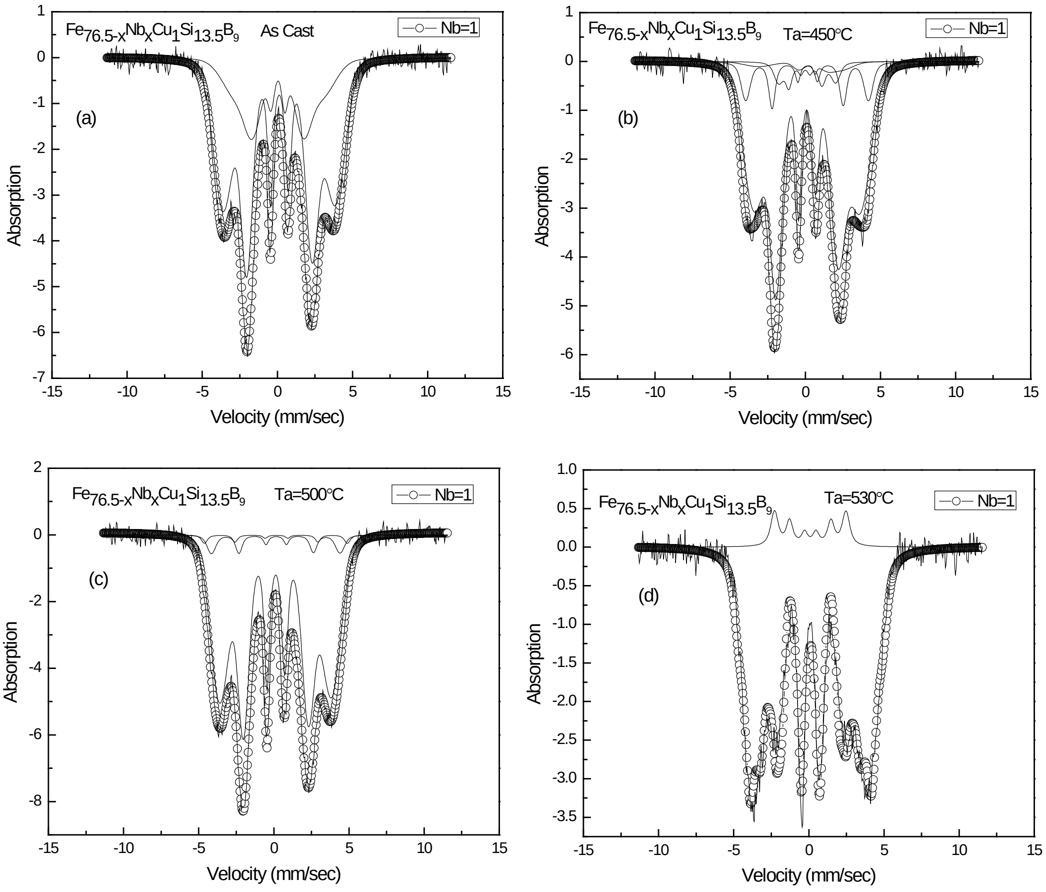

Figure 5.50: Mössbauer spectra of $Fe_{76.5-x}Nb_xCu_1Si_{13.5}B_9$ for x = 1 at (a) as cast, (b) 450°C (c) 500°C and (d) 530°C.

For silicon atoms indiscriminately substituted in iron atoms where nearest Fe neighbors and their relative absorption area are close to those expected by a binomial distribution [107, 143]. The present results, *i.e.* the hyperfine field, the isomer shift, the quadrupole shift and the relative absorption area, are fairly consistent with those previously discussed by Rixecker *et al.* at 300K [144]. Figure 5.50 shows the spectra of the amorphous and nanocrystalline states of the ribbons of Nb = 1. In the amorphous state, two superimposed Gaussian distributions were differentiated representing two forms of iron adjoining to reproduction the distribution asymmetry. In the crystallized state, three main phases were identified in all samples, one broadly distributed component of the intergranular phase and three boride-like iron sites was observed. In the case of FINEMETs, the Mossbauer spectra show a complex hyperfine structure Figure 5.50. The Mössbauer spectra of the $Fe_{76.5-x}Nb_xCu_1Si_{13.5}B_9$ samples for Nb = 1 were recorded at room temperature by using ^{57}Fe Mössbauer spectrometry in transmission geometry with invariable acceleration spectrometer. It is presumed that the Mössbauer spectra for Nb = 1 is accounted with cast, 450, 500 and 530^{o}C annealing temperature. From this Figure we perceive that, a good agreement with theoretical and experimental results has been raised for as cast, 450, 500 and 530^{o}C annealing temperature. According to as cast; Am_1 is completely amorphous. When temperature increases at 450^{o}C, the Am_1 is decreased at 84% amorphous whereas 16.70% of α-Fe-Si phase is developed. For 500^{o}C Am_1 and Am_2 is 60% and α-Fe-Si phase 40% and for 530^{o}C Am_1 30.5% and α-Fe-Si phase is 70%. It is clearly seen that with increasing annealing temperature, Am_1 decreased and α-Fe-Si increased. The amount of amorphous, crystalline α-Fe-Si is and % of Fe are represented in are given in Table 5.13.

It is also significant to draw attention to the magnetic texture of both crystalline grains and amorphous remainder has to be considered and that the presence of asymmetrical sextets or doublets is consistent with the correlation between hyperfine parameters [144]. More consistent knowledge is usually determined from

Table 5.13: Hyperfine parameters of Mössbauer spectra of $Fe_{76.5-x}Cu_1Nb_xSi_{13.5}B_9$ in as-cast and annealed condition for x = 1.

Anneal Condition	**Species**	***H* (T)**	**dH(T)**	**V_0 mm/s**	**Rel. Area (%)**	**% of Fe**	**Wt. fraction of phases (%)**
As-Cast	Am_1	17.70	0.83	0.035	0.469	53.1	Amorphous~100
	Am_1	23.12	0.57	0.00036	0.499	69.36	
450°C	Am_1	15.61	0.88	0.253	0.330	46.83	Amorphous~84.31 *α*-Fe-Si~16.70
	Am_1	21.89	0.63	0.253	0.513	65.67	
	α-Fe-Si	11.76	0.20	0.253	0.058	35.28	
	α-Fe-Si	25.27	0.20	0.253	0.109	75.81	
500°C	Am_1	17.38	0.85	0.004	0.201	52.14	Amorphous~60 *α*-Fe-Si~40
	Am_2	26.46	0.20	0.001	0.410	79.38	
	α-Fe-Si	29.40	0.08	0.033	0.402	88.2	
530°C	Am_1	24.99	2.00	0.025	0.305	74.97	Amorphous~30.50 *α*-Fe-Si~70
	α-Fe-Si	1.47	0.22	0.044	0.167	4.41	
	α-Fe-Si	20.58	0.20	0.025	0.372	61.74	
	α-Fe-Si	29.40	0.19	0.025	0.161	88.2	

zero-field Mössbauer experiments performed at room temperature or temperatures above than 200K, where the hyperfine structure is enhanced determined than that at lower temperatures. However it residue significant to scientifically cataloged 300 K spectra after high temperature experiments to ensure if the structural changes will not happen all through these high temperature measurements [145].

Figure 5.51 represents the Mössbauer spectra of $Fe_{76.5-x}Nb_xCu_1Si_{13.5}B_9$ for x = 3 at as cast, and completely annealed at temperatures 200°C, 300°C, 500°C, 550°C and 580°C. The Mössbauer spectrum of Nb = 3 for as cast, T_a = 200 and 300°C, 100% is Am_1 on the another data Am_1 for 300°C, is 100% Am_1 and α-Fe-Si for 500°C, 31.6% Amorphous and 69.40% *α*-Fe-Si for 550°C, 28% Amorphous and 77% *α*-Fe-Si for 580°C 21.16% Amorphous and 81.2% *α*-Fe-Si respectively. At annealed condition it is seen that, sextet pattern the spectra consist of broad overlapped lines assigned to disorder structural position of amorphous alloys and the sharp narrow lines indicate a

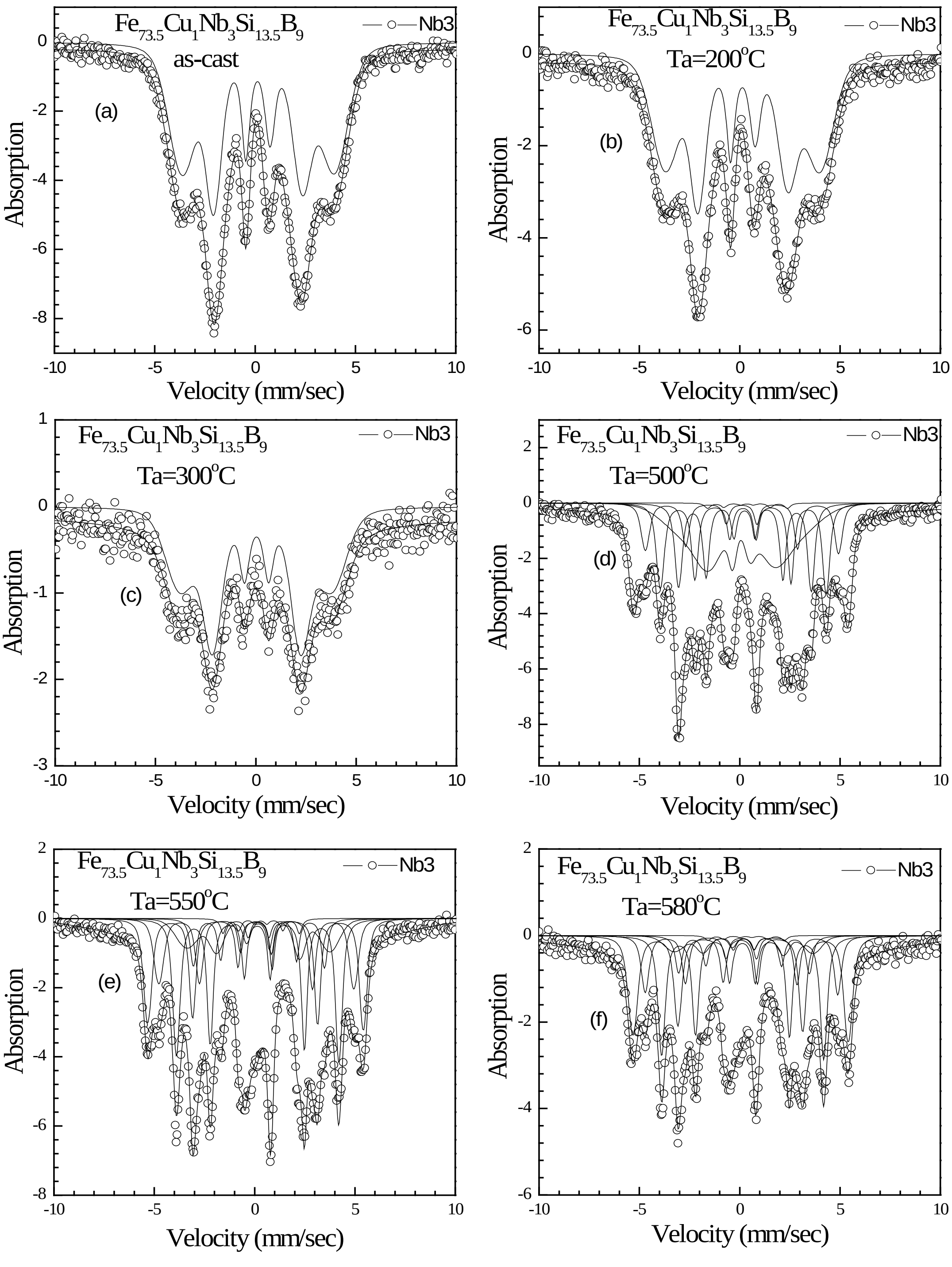

Figure: 5.51: Mössbauer spectra of $Fe_{76.5-x}Nb_xCu_1Si_{13.5}B_9$ for x = 3 at (a) as cast (b) 200°C, (c) 300°C, (d) 500°C, (e) 550°C and (f) 580°C.

percentage of *bcc*-Fe crystalline. The amount of amorphous, crystalline α-Fe-Si phase and % of Fe are presented in Table 5.14. The fitting process enhanced at room temperature and concerning numerous magnetic components according to the silicon

Table 5.14: Hyperfine parameters of Mössbauer spectra of $Fe_{76.5-x}Cu_1Nb_xSi_{13.5}B_9$ in as-cast and annealed condition for x = 3.

Anneal Condition	**Species**	***H* (T)**	***dH* (T)**	**V$_0$ mm/s**	**Rel. Area (%)**	**% of Fe**	**Wt. fraction of phases (%)**
As cast	Am$_1$	20.58	0.264	0.454	0.160	61.74	Amorphous~100
	Am$_1$	26.65	0.395	0.454	0.843	79.95	
200	Am$_1$	19.33	1.158	3.506	0.468	57.99	Amorphous~100
	Am$_1$	23.43	0.575	4.327	0.538	70.29	
300	Am$_1$	20.58	0.623	0.156	0.229	61.74	Amorphous~100
	Am$_1$	23.37	4.00	0.156	0.576	70.11	
	Am$_1$	12.30	8.307	0.569	0.178	36.9	
500	Am$_1$	14.86	19,601	0.569	0.212	44.58	Amorphous~31.6 α-Fe-Si~69.40
	Am$_2$	25.56	9.710	0.569	0.104	76,68	
	α-Fe-Si	16.59	1.081	0.569	0.267	49.77	
	α-Fe-Si	20.43	0.710	0.569	0.145	61.29	
	α-Fe-Si	33.03	0.111	0.569	0.091	99.09	
	α-Fe-Si	33.03	0.141	0.569	0.191	99.09	
550	Am$_1$	11.76	0.010	0.473	0.113	35.28	Amorphous~28 α-Fe-Si~77
	Am$_2$	1.47	10.00	0.104	0.170	4.41	
	α-Fe-Si	20.21	0.952	0.473	0.164	60.63	
	α-Fe-Si	30.04	0.161	0.473	0.206	90.12	
	α-Fe-Si	30.046	0.123	0.473	0.170	90.138	
	α-Fe-Si	38.528	0.123	0.473	0.123	115.58	
	α-Fe-Si	22.050	0.446	0.473	0.107	66.15	
580	Am$_1$	11.760	0.010	0.469	0.100	35.28	Amorphous~21.6 α-Fe-Si~81.2
	Am$_2$	1.484	10.00	0.199	0.116	4.452	
	α-Fe-Si	20.139	5.32	0.469	0.111	60.417	
	α-Fe-Si	29.574	0.847	0.469	0.213	88.722	
	α-Fe-Si	29.679	0.847	0.469	0.105	89.037	
	α-Fe-Si	33.178	1.40	0.469	0.221	99.534	
	α-Fe-Si	21.388	0.384	0.469	0.162	64.164	

content *i.e.* hyperfine parameter depends at the annealing temperature for each spectrum recorded at different annealing temperatures.

Mössbauer spectra of $Fe_{76.5-x}Nb_xCu_1Si_{13.5}B_9$ at room temperature where x = 5 at as cast and 550^{o}C are driven for both of amorphous and nanocrystalline state which reveals good harmony between theoretical and experimental results. For as cast condition sample is fully amorphous but when increase in temperature at 550^{o}C, the Am$_1$ is decrease in 20.8% amorphous and 79.5% α-Fe-Si phase. It is observed that,

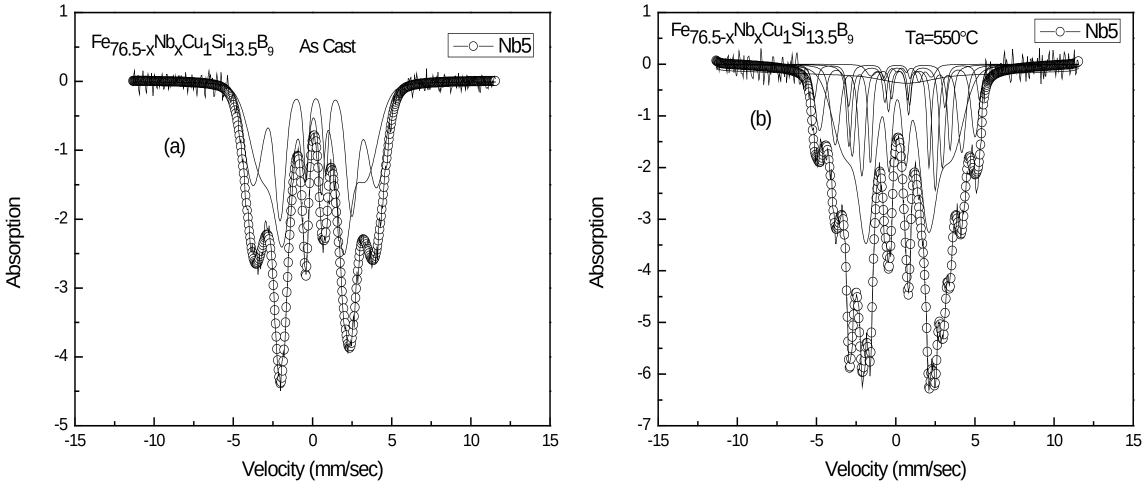

Figure 5.52: Mössbauer spectra of $Fe_{76.5-x}Nb_xCu_1Si_{13.5}B_9$ for x = 5 at (a) as cast and (b) 550^oC.

with increasing annealing temperature, Am_1 declined and α-Fe-Si enlarged. The amount of amorphous, crystalline α-Fe-Si and % of Fe are presented in Table 5.15.

Table 5.15: Hyperfine parameters of Mössbauer spectra of $Fe_{76.5-x}Cu_1Nb_xSi_{13.5}B_9$ in as-cast and annealed condition for x = 5.

Anneal Condition	Species	*H*(*T*)	*dH* (T)	V_0 mm/s	Rel. Area (%)	% of Fe	Wt. fraction of phases (%)
As-Cast	Am_1	20.21	0.692	0.169	0.569	60.63	Amorphous~100
	Am_1	24.12	0.483	0.166	0.440	72.36	
$550^{\circ}C$	Am_1	14.70	20.00	0.523	0.125	44.10	Amorphous~20.8 α-Fe-Si~79.5
	Am_2	11.83	0.200	0.523	0.083	35.49	
	α-Fe-Si	20.58	0.720	0.133	0.188	61.74	
	α-Fe-Si	19.69	0.076	0.523	0.175	59.07	
	α-Fe-Si	24.72	0.200	0.523	0.171	74.16	
	α-Fe-Si	30.28	0.200	0.523	0.212	90.84	
	α-Fe-Si	32.34	0.072	0.523	0.049	97.02	

However, atomic diffusion, which arises in the annealing process, gives ascend to a chemically and structurally heterogeneous intergranular phase; therefore, the amorphous content may not be explained by a distribution of hyperfine. The foremost difficulty is how to disconnect the crystalline and amorphous contents, which are robustly overlapped, and consequently to determine (i) the number of magnetic sextets consigned to the crystalline constituent and their relative intensity, *i.e.*, the silicon content in the Fe–Si phase, (ii) the shape of sextet or doublet, with the upper and lower limits properties of the amorphous phase and (iii) their relative proportions [146]. Three components are accredited to the crystalline grains, residual amorphous matrix and the interfacial region, which is distinct as the transitional zone among the core of nanocrystalline grains and amorphous state [147,148]. Figure 5.53 represents Mössbauer spectra of $Fe_{76.5-x}Nb_xCu_1Si_{13.5}B_9$ at as cast, 500^{o}C, 550^{o}C and 650^{o}C for x = 7. The Mössbauer spectra of Nb = 7 for both of amorphous and α-Fe-Si phases were calculated at room temperature by using ^{57}Fe Mossbauer spectrometry in transmission geometry with constant acceleration spectrometer.

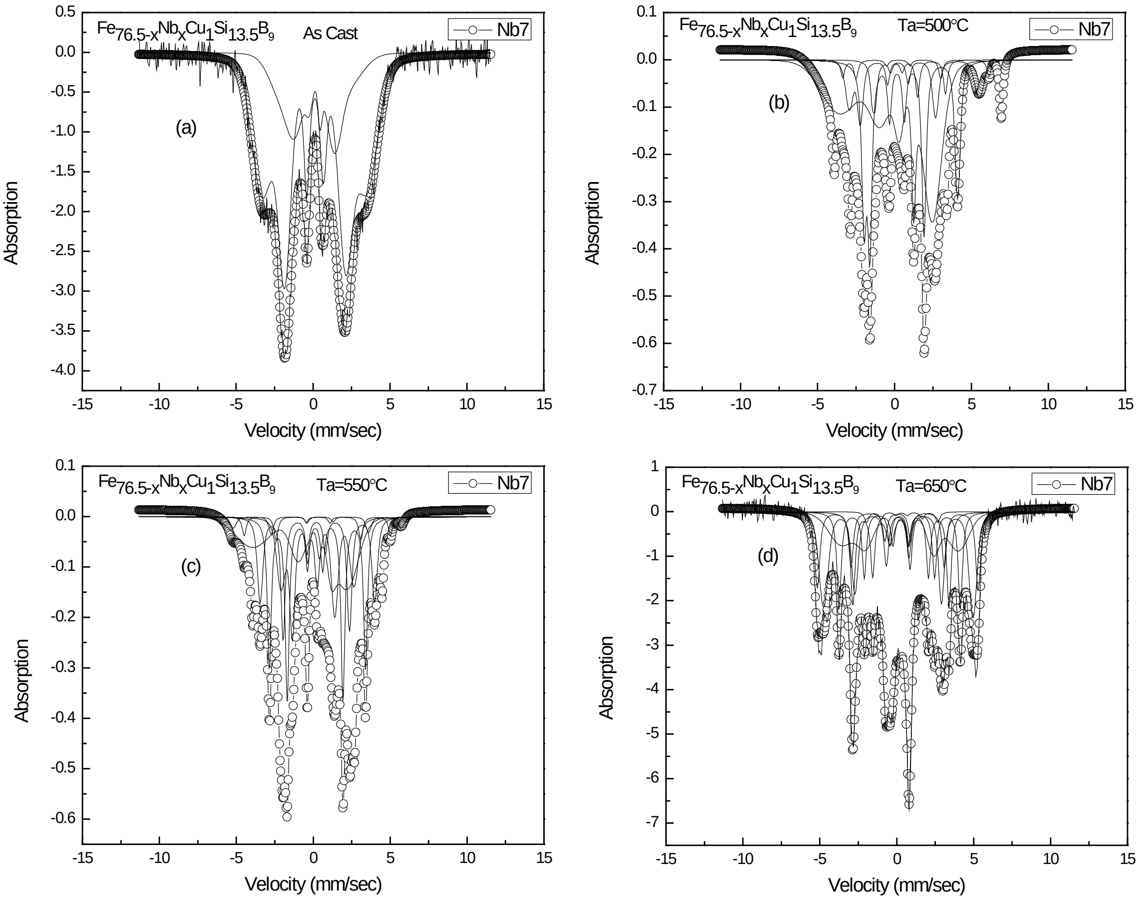

Figure 5.53: Mössbauer spectra of $Fe_{76.5-x}Nb_xCu_1Si_{13.5}B_9$ where x = 7 at (a) as cast (b) 500^{o}C (c) 550^{o}C and (d) 650^{o}C.

The sample for Nb = 7 were annealed at as cast, 500^{o}C, 550^{o}C and 650^{o}C where it can say that the theoretical and experimental study for both annealing temperature at as cast, 500^{o}C, 550^{o}C and 650^{o}C are matched in good consequences. At as cast, the sample is recorded in full amorphous state. For higher annealing temperatures like 500^{o}C, 550^{o}C and 650^{o}C the Am$_1$ are 75%, 37% and 28.5% whereas α-Fe-Si phases are 25.6%, 63% and 71.5% respectively. So, from the above data, it is found that, when

Table 5.16: Hyperfine parameters of Mössbauer spectra of $Fe_{76.5-x}Cu_1Nb_xSi_{13.5}B_9$ in as-cast and annealed condition for x = 7.

Anneal Condition	Species	*H* (*T*)	*dH* (T)	V_0 mm/s	Rel. Area (%)	% of Fe	Wt. fraction of phases (%)
As-Cast	Am$_1$	13.42	0.806	0.011	0.257	40.26	Amorphous~100
	Am$_1$	21.02	0.603	0.00065	0.744	63.06	
500°C for 30 min	Am$_1$	18.32	0.925	0.600	0.273	54.96	Amorphous~75 α-Fe-Si~25.6
	Am$_1$	14.70	0.010	0.243	0.252	44.1	
	Am$_2$	18.67	0.08	0.243	0.230	56.01	
	α-Fe-Si	26.14	0.200	0.243	0.073	78.42	
	α-Fe-Si	29.40	0.010	0.243	0.081	88.2	
	α-Fe-Si	33.52	0.010	0.243	0.102	100.56	
550°C for 30 min	Am$_1$	18.04	0.896	0.00073	0.180	54.12	Amorphous~37 α-Fe-Si~63
	Am$_2$	23.02	0.100	0.00073	0.192	69.06	
	α-Fe-Si	14.70	0.200	0.01	0.214	44.1	
	α-Fe-Si	19.33	0.00	0.00073	0.232	57.99	
	α-Fe-Si	26.01	0.010	0.00073	0.113	78.03	
	α-Fe-Si	29.40	0.024	0.00073	0.034	88.2	
	α-Fe-Si	33.81	0.130	0.00073	0.038	101.43	
650°C for 30 min	Am$_1$	13.55	0.676	0.557	0.100	40.65	Amorphous~28.5 α-Fe-Si~71.5
	Am$_1$	6.54	0.530	0.303	0.087	19.62	
	Am$_2$	4.62	0.033	0.557	0.098	13.86	
	α-Fe-Si	14.29	0.010	0.557	0.134	42.87	
	α-Fe-Si	24.39	0.010	0.557	0.127	73.17	
	α-Fe-Si	30.02	0.200	0.557	0.218	90.06	
	α-Fe-Si	32.34	0.062	0.557	0.236	97.02	

annealing temperature is increase, Am_1 decreased and α-Fe-Si increased. But it is clearly seen that the grain growth inhibiting power of refractory Nb metal or in general the higher Nb content restrict the formation crystallization. The amount of amorphous, crystalline α-Fe-Si is and % of Fe given in Table 5.16. In both categories of nanocrystalline alloys, diverse fitting models are able to reproduce a given spectrum with outstanding harmony. From Figure 5.53 it is seen that the validity has to be first checked either by following the temperature dependencies of the hyperfine parameters [109] or by taking into account of different γ-beam configurations leading to an invariant set of hyperfine parameters [148]. Mössbauer spectroscopy in order to correlate the ultrasoft magnetic properties with the volume fraction of amorphous and α-Fe(Si) soft nanocrystalite. The volume fraction of the relative amount of amorphous and crystalline phase are also determined. The quantitative relative amount of amorphous and crystalline phase for both composition sample relatively show good agreement with theoretical and experimental data.

Chapter 6

Conclusions

This thesis focuses on the study of the crystallization kinetics of amorphous magnetic ribbons of two series of alloy compositions with, (I) $Fe_{73.5-x}Cr_xNb_3Cu_1Si_{13.5}B_9$ (x =1, 5, 10, 12.5 and 17.5) and (II) $Fe_{76.5-x}Nb_xCu_1Si_{13.5}B_9$ (x = 1, 2, 3, 4, 5, 6 and 7) prepared by melt spinning technique. The alloys are initially fabricated in the amorphous state as a result of rapid solidification with a cooling rate of $\approx 10^5$ $Ksec^{-1}$ and subsequently annealed isothermally at various temperatures around and /or above their crystallization temperatures. This treatment enables the samples to acquire varying degree of nanocrystalline structure through controlled crystallization kinetics based on which the ultra-soft magnetic properties finally develop. The optimum soft magnetic properties are manifested when the size of the magnetic nanocrystals of primary crystallization product (Fe-Si) is around 10-15 nm with appropriate volume fraction of ≈ 80%. This unique condition facilitated on strong magnetic coupling via close exchange interactions a result of reduced magnetic anisotropy and magnetostriation due to nanometric size Fe-Si magnetric grains embedded on residual amorphous matrix. The reason for choosing the two series of composition in this thesis based on FINEMET alloy $Fe_{73.5-x}Cr_xNb_3Cu_1Si_{13.5}B_9$, with variation in Cr and Nb substituted for Fe is to study the crystallization behavior and how it affects the magnetic properties. Both the Cr and Nb are refractory metal and inhibit crystallization as well as hinder grain growth while Cu, the promoter of crystallization and grain growth is kept constant. It is well known that Nb is thermally more stable then Cr. A detail study on the crystallization kinetics of the proposed amorphous magnetic system in this research will discern the role of Cr and Nb in the nanocrystallization of the prepared samples.

DSC has been used to investigate the crystallization behavior of the samples. The amorphosity and crystallization product and their crystallite size have been examined by XRD while magnetization has been measured by VSM, permeability by impedance analyzer. Surface morphology and microstructural study, *i.e.* grain size and their distribution function have been observed by FESEM. Mössbauer spectrometry has been fruitfully utilized to find out the volume fraction of various phases including amorphous phase that develops during the crystallization process when annealed at high temperature. Thus from the detailed investigation on crystallization behavior phases that evolved during annealing, their volume fraction grain size and their distribution, structural and magnetic properties of the studied sample, the following conclusions can be outlined.

The crystallization peak temperatures for the $Fe_{73.5-x}Cr_xNb_3Cu_1Si_{13.5}B_9$ and $Fe_{76.5-x}Nb_xCu_1Si_{13.5}B_9$ systems determined by differential scanning calorimetry (DSC), with constant heating rate is found to have strong dependence on Cr content and increase monotonically to higher temperature for both primary as well as secondary crystallization events corresponding to the evolution of bcc-Fe(Si) and Fe-B phase respectively with the appearance of exothermic peaks in the DSC thermogram. Based on the knowledge of primary crystallization peak temperature, different annealing temperatures have been set for each sample for a predetermined holding time for the nanocrystallization of the studied samples. To avoid secondary crystallization product of Fe-B, which is detrimental for soft magnetic properties, samples for both series with Cr and Nb substitution were annealed at temperature much lower than the secondary crystallization peak temperatures. The activation energy of crystallization has been determined for the Nb substituted sample with x = 7 (Nb) from the heating rate dependence of DSC thermogram using Kissinger method, and found to be 4.24 and 7.68 eV for the primary crystallization of Fe(Si) and secondary crystallization Fe-B phase respectively. The shift of both primary and secondary crystallization temperature to higher temperature with substitution of increasing amount of Cr and Nb clearly indicates the enhancement of thermal stability of the amorphous alloy against crystallization.

X- ray diffraction confirmed the amorphous state of all the as prepared samples for both the series with the appearance of broaden diffused peak at [110] plane. The evaluation of primary phases on annealed samples at different temperatures have been confirmed as bcc-Fe(Si) from XRD pattern with the manifestation of sharp peak instead of diffused broadened one which become sharper and narrower with increasing annealing temperature. The temperature corresponding to the onset of crystallization obtained from the XRD pattern is closer to that of DSC data. The grain size of *bcc*-Fe (Si) calculated from the line broadening of XRD peak using Scherrer's formula is found to decrease with increasing Cr and Nb content while it increases with increasing annealing temperature, T_a. The higher Cr and Nb content alloys do not show any sign of crystallization in their XRD Pattern even at annealing temperature of 540^{o}C for 30 min. This is quite reasonable since their crystallization temperature is above 540^{o}C obtained from DSC data. The grain size of Cr substituted samples annealed at T_a = 540^{o}C with x = 1 is 15 nm compared with 11 nm and 4 nm for x = 5 and 10 respectively. When Cr content is higher, *i.e.* $x \geq 12.5$, they are still in the amorphous state with no sign of crystallization even up to annealing temperature of T_a = 540^{o}C.

Again for Nb substituted sample with x = 3, the grain size at T_a = 550^{o}C is found to be 9 nm compared with 6 nm for x = 5 and still in amorphous state of all sample having x ≥ 6. The sample with x = 7 become crystalline only at T_a = 600^{o}C with grain size of 6 nm. From DSC and XRD data it can be concluded that the Nb act as more powerful agent to hinder crystallization and control the nucleation and growth of *bcc*-Fe(Si) nanograins.

Microstructural study done by FESEM revealed that all samples of both the series in the as prepared composition are perfectly amorphous with clear background and do not show any sign of crystallization with increasing T_a > 500^{o}C initiation of crystallization with the appearance of nanometric grains with highly agglomerated condition is clearly observed except for samples with high amount of Cr and Nb. Sample with lower content of Cr and Nb, microstructer is well matured and with abundant volume fraction of bcc-Fe(Si) nanograins especially with Cr = 1 and Nb = 3 annealed at T_a = 550^{o}C. Exact grain size is difficult to determine from FESEM image since they are agglomerated. For higher content of Cr = 12.5 and 17.5 and Nb = 7 microstructure with high volume fraction of Fe(Si) grains are only observed at T_a = 600^{o}C and above. But all the studied samples for both the series display unique microstructure in the initiation of crystallization event with nanometric grains evolved in the amorphous matrix. It is revealed from the FESEM microstrucaral study that optimum microstructure with compact grains having high volume fraction of Fe(Si) nanograins are obtained for samples Cr = 1, 5 and Nb = 3 that are responsible for better magnetic properties. For accurate determination of grain size of Nb substituted sample with Nb = 3, a TEM image has been taken where an uniform distribution of *bcc* α-Fe(Si) nanograins with compact microstructure revealed a grain size of 13 nm. This clearly demonstrates the original grain size of our crystallized sample for which excellent soft magnetic properties are expected based on random anisotropy model proposed by G. Herzer.

Magnetization (emu/gm) of the amorphous alloys decreases with the increase of Cr content due to simple dilution effect. The sample with Cr content 12.5 and 17.5 found to be paramagnetic at room temperature. When these samples are annealed at T_a = 500°C, they showed enhanced magnetization, but $M(H)$ curves still look paramagnetic in nature. Pronounced effect in magnetization enhancement has been observed in sample with Cr = 10 on also upon annealing. This may be attributed to irreversible structural relaxation of the amorphous samples. A sharp increase of magnetization from 12.1 emu/gm for Cr = 12.5 and 3.8 emu/gm for Cr = 17.5 to 48.7 and 27.4 emu/gm respectively annealed at T_a = 600°C may be connected with initiation of crystsllization of Fe(Si) magnetic phase.

All Nb substituted samples shows monotonically decreasing trend of M_s values with increasing Nb content and has been explained due to dilution of Fe magnetic moment. The saturated magnetization value M_s of the samples measured at T = 80K show higher value than measured at room temperature due to thermal effect. The M_s value of Nb = 1 and 7 at RT are 159 emu/gm and 118 emu/gm compared with 165 emu/gm and 146 emu/gm measured at T = 80K. The Curie temperature, T_c for the Nb substituted samples decrease monotonically from T_c = 410°C for Nb = 1 to T_c = 323°C with Nb = 7. Temperature dependence of magnetization $M(T)$ of Nb substituted sample clearly demonstrates the crystallization behavior of the samples where magnetic phase transition temperature, T_c, of amorphous phase, onset and peak crystallization temperature,(T_X, T_P), T_c of *bcc*-Fe(Si) phase. The results are well comparable with XRD, DSC and FESEM data.

The detail study of complex permeability of all the samples in the as cast and annealed condition as a function of frequency clearly demonstrated that a dramatic increase of real part of permeability, μ' and a substantial reduction of imaginary part of permeability, μ'' and/or significant reduction of magnetic loss $\tan\delta = \mu''/\mu'$ have been observed for sample with Cr = 1, 5 and Nb = 3, 4 annealed at T_a = 550°C compared with their amorphous counterpart. This unique behavior of sharp enhancement of magnetic permeability is related to the nanostructured microstructer of Fe(Si) nanograins with grain sizes within 10-15 nm having abundant volume fraction of ≈ 80% that are strongly coupled via exchange interaction as result of optimum crystallization of the samples.

The Mössbauer spectroscopy done on amorphous and annealed samples revealed quantitatively relative amount of amorphous and crystalline phase along with hyperfine field distribution, peak width (d*H*) and magnetic state of the samples.

Bibliography

[1] I. Matko, E. Illekova, P. Svec and P. Duhaj, *Mater. Sci. Eng.*: A, **225**:145, 1997.

[2] R. Singhal and A. K. Majumdar, *J. Magn. Magn. Mat*. **115:**245,1992.

[3] H. Chiriac and C. S. Marinescu, *Sens. Actuators A: Physical* **81:**174, 2000.

[4] M. A. Gibson and G.W. Delamore, *J. Mater. Sci*. **27:**3533, 1992.

[5] M. S. Leu, J. S. C. Jang, C. C. Lin and W. K. Wang, *Mater. Chem. Phys.* **45:** 275, 1996.

[6] K. Chrissafis, M. I. Maragakis, K. G. Efthimiadis and E. K. Polychroniadis, *J. Alloys Compd*. 386**: 165**, 2005.

[7] K. G. Efthimiadis, E. K. Polychroniadis, S. C. Chadjivasiliou and I. A. Tsoukalas, *Mater. Res. Bull.* **35:** 937, 2000.

[8] A. Lovas, L. F. Kiss, B. Varga, P. Kamasa, I. Balogh and I. Bakonyi, J. Phys. IV *France* **08:** Pr-291, 1998.

[9] K. Hono, Y. Zhang, A. Inoue and T. Sakurai, *Material Transaction, JIM* **36:** 909, 1995.

[10] K. Hono, K. Hiraga, Q. Wang, A. Inoue and T. Sakurai, *Acta. Metall. Mat.* **40**: 2137, 1992.

[11] G. Herzer, *Scripta Metall. Mater.* **33**: 1741, 1995.

[12] D. Holzer, I. Pérez de Albéniz, R. Grössinger and H.Sassik, *J. Magn. Magn. Mat*. **203**: 82, 1999.

[13] N. Chau, N. H. Luong, N. X. Chien, P. Q. Thanh and L. Van Vu, *Physica B: Cond Mat.* **327:** 241, 2003.

[14] N. Chau, N. Q. Hoa and N. H. Luong, *J. Magn. Magn. Mat*. **290-291**: 1547, 2005.

[15] N. Chau, N. Q. Hoa, N.D. The and L.V. Vu, *J. Magn. Magn. Mat*. **303:** e415, 2006.

[16] J. S. Blazquez, J. M. Borrego, C. F. Conde, A. Conde and J. M. Grenche, *J. Phys.: Condens. Matter* **15**: 3957, 2003.

[17] C. Gomez-Polo, J. I. Perez-Landazabal and V. Recarte, *IEEE Trans. Magn*. **39**: 3019, 2003.

[18] N. Q. Hoa, N. Chau, S. C. Yu, T.M. Thang, N. D. The and N. D. Tho, *Mater. Sci. Eng.* A: **449–451**: 364, 2007.

[19] W. A. Johnson and R. F. Mehl, *Trans. Am. Inst. Min. Eng*. **135**: 416, 1939.

[20] T. Ozawa, *Bull. Chem. Soc. Jpn.* **38**:1881, 1965.

[21] J. A. Augis and J. E. Bennett, *J. Therm. Anal.* **13**: 283, 1978.

[22] H. Gleiter, *Progress in Materials Science*, **33**: 223, 1989.

[23] M. E. McHenry, S. A. Majetich, De Graef, M. Artman, J. O. and S. W. Staley, *Phys. Rev. B*, **49**:11358,1994.

[24] M. E. McHenry, M. A. Willard, H. Iwanabe, R. A. Sutton, Z. Turgut, A. Hsiao and D. E. Laughlin, *Bull. Mater. Sci.,* **22**: 495, 1999.

[25] D. Appell, *Nature*, **419:** 553, 2002.

[26] Judit Kopniczky, *Nanostructures studied by atomic force microscopy,* Ph. D. Thesis, Uppsala University, Sweden, 2003.

[27] R. C. O'Handley, *Modern Magnetic Materials: Principles and Applications,* John Wiley & Sons, Inc. New York, 1999.

[28] L. K. Varga, É. Bakos, L. F. Kiss and I. Bakonyi, *Mat. Sci. and Eng.*: A **179-180**: 567, 1994.

[29] Z. Turgut, M. Q. Huang, K. Gallagher, S. A. Mayelich and M. E. McHenry, *J. Appl. Phys.,* **81**: 4039, 1997.

[30] Z. Turgut, N. T. Nuhfer, H. R. Piehler and M. E. McHenry, *J. Appl. Phys*., **85:** 4406, 1999.

[31] F. W. A. Dirne and M. Brouha, *IEEE Trans. Magn.* **24**: 1862, 1988.

[32] H. J. de Wit, *J. Magn. Magn. Mat*., **79:** 167, 1989.

[33] Y. Yoshizawa, S. Oguma and K. Yamauchi, *J. Appl. Phys.,* **64**: 6044, 1988.

[34] Y. Yoshizawa, and K. Yamanchi, *Materials Transaction, JIM* **31:** 307, 1990.

[35] A. Z. Ziauddin Ahmed**,** Md. Saiful Alam, G. M. Bhuiyan, Md. Masud Rana and R. I. M. A. Rashid, Electrical Resistivity of Amorphous Fe and Ni, *I. J. Mod. Phys. B* **24**, 5417, 2010.

[36] G. Herzer, *IEEE Trans. Magn.* **25**: 3327, 1989.

[37] G. Herzer, *IEEE Trans. Magn.***26**:1397, 1990.

[38] G. Herzer, *Proc. Int. Symp. on 3d Transition-Semi Metal Thin Films, Sendai* **130:** 1991.

[39] J. M. Borrego, C. F. Conde, and A. Conde, *Phil. Mag. Lett*. **80**: 359, 2000.

[40] R. S. Turtelli, V. H. Duong, R. Grossinger, M. Schwetz, E. Ferrara, and N. Pillmayr, *IEEE Trans. Magn*. **36**: 508, 2000.

[41] M. Baricco, C. Antonine, P. Ailia, P. Tiberto, and F. Vinai, *Mater. Sci. Eng.*: A **179-180:** 572, 1994.

[42] P. Gorria, J. S. Garitaonandia, and J.M. Barandiaraan, *J. Phys.*: *Condens. Matter* **8**: 5925, 1996.

[43] K. Hono, A. Inoue and T. Sakurai, *Appl. Phys. Lett.* **58**: 2180, 1991.

[44] A. Pundt, G. Hampel and J. Hesse, Z. Phys. *B* **87**: 65, 1992.

[45] B. Varga, Takács, A. Lovas and P. Kamasa, Fei ZHOU and J. Vandlik, *J. Mat. Sci. Technol.* **14:** 323, 1998.

[46] A Lovas, L. F. Kiss and I. Balogh. *J. Magn. Magn. Mat.* **215:** 463, 2000.

[47] H. Shokrollahi, *Materials & Design* **30:** 3374, 2009.

[48] K. Suzuki, N. Kataoka, A. Inoue, A. Makino and T. Masumoto, *Materials Transactions, JIM* **31**: 743, 1990.

[49] M. A. Willard, D. E. Laughlin, M. E. McHenry, D. Thoma, K. Sickafus, J.O. Crossand and V. G. Harris, *J. Appl. Phys.* **84**: 6773, 1998.

[50] G. Herzer, *Digest Intermag Conf.* (28-31. March 1989), paper AQ 3, Washington, USA.

[51] Giselher Herzer, *Handbook of Magnetic Materials* **10:** 415, 1997.

[52] A. Zorkovská, J. Kováč, P. Sovák, P. Petrovič and M. Konč, *J. Magn. Magn. Mat.* **215-216:** 492, 2000.

[53] Y. R. Zhang and R. V. Ramanujan, *J. Mater Sci* **41**: 5292, 2006.

[54] O. Životský, L. Klimša, A. Hendrych, Y. Jirásková and J. Buršík, *J. Supercond Nov Magn* **26**: 1349, 2013.

[55] N. Bayri, T. Izgi, H. Gencer, P. Sovak , M. Gunes and S. Atalay, *J. Non-Cryst. Solids* **355**: 12, 2009.

[56] K. Biswas, S. Ram, L. Schultz and J. Eckert, *J. Alloys. Compd.* **397:** 104, 2005.

[57] C. Miguel, A. Zhukov, J. J. del Val and J. González, *J. Magn. Magn. Mat.* **294:** 245, 2005.

[58] M. A. Hakim, S. Manjura Hoque, M. Khalilur Rahman and Jamal Uddin Ahamed, Journal of Nuclear Science of Applications **29:** 117, 2005.

[59] Md. Khalid Hossain, Jannatul Ferdous, Md. Manjurul Haque and A. K. M. Abdul Hakim, *Materials Sciences and Applications*, **6:** 1089, 2015.

[60] K. Suzuki and J. M. Cadogan, *Physical Review B* **58:** 2730, 1998.

[61] L. Wang, J. Ding, H. Z. Kong, Y. Li and Y. P. Feng, *Physical Review B* **64:** 214410, 2001.

[62] K. Suzuki and G. Herzer, *Scripta Materialia*: **67:** 548, 2012.

[63] Jörg F. Löffler, Jürg P. Meier, Bernard Doudin, Jean-Philippe Ansermet and Werner Wagner, *Phys. Rev. B* **57**: 2915, 1998.

[64] C. Kuhrt and L. Schultz, *J. Appl. Phys*. **73**: 6588, 1993.

[65] C. Suryanarayana, *Int. Mater Rev*. **40**: 41, 1995.

[66] N. Kataoka, T. Matsunaga, A. Inoue and T. Masumoto, *Materials Transactions, JIM*: **30**: 947, 1989.

[67] Y. Yoshizawa and K. Yamauchi, *Mater. Sci. Eng.: A* **133:** 176, 1991.

[68] M. Muller and N. Mattern, *J. Magn. Magn. Mat*. **136:** 79, 1994.

[69] G. Herzer, *Mat. Sci. Eng.:A* **133:** 1, 1991.

[70] G. Herzer, *J. Magn. Magn. Mat*. **157-158:** 133, 1996.

[71] A. Ślawska-Waniewska, M. Gutowski, H. K. Lachowicz, T. Kulik and H. Matyja, *Phys. Rev. B.* **46:** 14594, 1992.

[72] Golam Mohammed Bhuiyan, *Solid State Physics-I* (in Bengali), pp. 72, Quantum Publisher, Dhaka, Bangladesh, 2012.

[73] V. Franco, C. F. Conde, A. Conde and L. F. Kiss, *J. Magn. Magn. Mat*. **215-216:** 400, 2000.

[74] S. Tanuma, S. Ichimura and K. Yoshihara, *Appl. Surf. Sci.* **100-101:** 47, 1996.

[75] D. A. Porter and K. E. Easterling, *Phase Transformations in Metals and Alloys,* CRC Press, Taylor & Francis Group, London, UK, 3rd Edition, 1992.

[76] Kiyohiko Nohara and Ken-ichi Hirano, *J. Jpn. Inst. Metals* **40:** 1053, 1976.

[77] A. Michelsa, C. E. Krilla, H. Ehrhardta, R. Birringera and D. T. Wub, *Acta* M*ater.* **47:** 2143, 1999.

[78] J. H. Perepezko, R. J. Hebert, R. I. Wu and G. Wilde, *J. Non-Cryst. Solids* **317:** 52, 2003.

[79] Akihisa Inoue, *Bulk Amorphous Alloys - Preparation and Fundamental Characteristics,* Materials science foundations Volume 4, *pp*. 1422, Uetikon-Zuerich, Switzerland; Enfield, N.H.: Trans Tech Publications, 1998.

[80] T. R. Anantharaman, *Metallic Glasses, Production, Properties and Applications,* Trans. Tech. Publications, Switzerland, 1984.

[81] W. Klement Jun, R. H. Willens and Pol Duwez, *Nature*, **187:** 869, 1960.

[82] A. Inoue, *Acta Mater.,* **48:** 279, 2000.

[83] C. Kuhrt, and L. Schultz, *J. Appl. Phys*. **73:** 6588, 1993.

[84] J. F. Löffler, *Intermetallics,* **11:** 529, 2003.

[85] William L. Johnson, Akihisa Inoue and C. T. Liu (Editors), *Bulk Metallic Glasses*: Volume 554, (MRS Proceedings), Cambridge University Press, Cambridge, 1st Edition, 1999.

[86] Kenji Amiya and Akihisa Inoue, *Materials Transactions*, *JIM*, **43:** 81, 2002.

[87] Renate M.R. Wellen and Eduardo L. Canedo, *Polymer Testing* **40:** 33, 2014.

[88] J. D. Ayers, V. G. Harris, J. A. Spague and W. T. Elan, *Appl. Phys. Lett*. **64:** 974, 1994.

[89] U. Köster, U. Schönemann, M. Blank-Bewerdorff, S. Brauer, M. Sutton, and G. B. Stephenson, *Mater. Sci. Eng*.: A **133:** 611, 1991.

[90] Michael E. McHenry, Matthew A. Willard and David E. Laughlin, *Progress in Materials Science* **44:** 291, 1999

[91] L. del Riego, M. El Ghannami, M. Dominguez and C. F. Conde, *J. Magn. Magn. Mat.***196-197:** 201, 1999.

[92] T. Kulik and A. Hernando, *J. Magn. Magn. Mat.* **138:** 270, 1994.

[93] B. S. Murty, M. K. Datta and S. K. Pabi, *Sadhana* **28:** 23, 2003.

[94] C. Suryanarayana and C. C. Koch, Nanocrystalline materials–*Current research and future directions, Hyperfine Interactions* **130:** 5, 2000.

[95] Y. Yoshizawa, S. Oguma and K.Yamauchi, *J. Appl. Phys*. **64:** 6044 , 1988.

[96] S. P. Mondal, Kazi Hanium Maria, S. S. Sikder, Shamima Choudhury, D. K. Saha and M. A. Hakim, *J. Mater. Sci. Technol.*, **28:** 21, 2012.

[97] K. Suzuki and G. Herzer, (In: Advanced Magnetic Nanostructures, D. Sellmyer, R. Skomski (editors)), pp. 365-401, Springer, Boston, MA, USA, 2006.

[98] T. Ozawa, *Polymer* **12:** 150, 1971.

[99] V. Cremaschi, G. Sánchez and H Sirkin, *Physica B: Condensed Matter* **354:** 213, 2004.

[100] J. Zbroszczyk, H. Fukunaga, J. Olszewski, W. H. Ciurzynska and M. Hassiak, *J. Magn. Magn. Mat.*, **160:** 277, 1996.

[101] N. A. Mariano, C. A. C. Souza, J. E. May and S. E. Kuri, *Mater. Sci. Eng.:A* **354:** 1, 2003.

[102] Casey Smith, Shravana Katakam, Soumya Nag, Y. R. Zhang, J. Y. Law, Raju V. Ramanujan, Narendra B. Dahotre, Rajarshi Banerjee, *Metallurgical and Materials Transactions A* **45:** 2998, 2014.

[103] H. Okumura, D. E. Laughlin, M. E. McHenry, *J. Magn. Magn. Mat.***267**: 347, 2003.

[104] M. A. Hakim, *Nuclear Science and Applications* **13:** 35, 2004.

[105] I. Turek, J. Hafner, *Phys. Rev. B***46**: 247, 1992.

[106] A. Hernando and T. Kulik, *Phys. Rev. B.* **49:** 7064(R), 1994.

[107] R. Mössbauer, *Nobel lecture*, 1961.

[108] Golam Mohammed Bhuiyan, Quantum Mechanics (in Bengali), Quantum Publishers, Dhaka, Bangladesh, 2005.

[109] Dominic P. E. Dickson and Frank J. Berry, Mössbauer spectroscopy, *pp*. 1, Cambridge University Press, New York, 1986.

[110] Dennis V. Perepelista, *Mössbauer Spectroscopy of* ^{57}Fe, MIT, Department of Physics, April 6, 2007.

[111] R. Preston, S. Hanna and J. Heberle, *Phys. Rev.* **128:** 2207**,** 1962.

[112] D. J. Griffiths, *Introduction to Quantum Mechanics*, Pearson, USA, 2nd edition, 2004.

[113] O. C. Kistner and A. W. Sunyar, *Phys. Rev. Lett.* **4:** 412**,** 1960.

[114] K. S. Bindra, Nikhil Suri, M. S. Kamboj and R. Thangaraj, *Journal of Ovonic Research* **3**: 1, 2007.

[115] H. E. Kissinger, *J. Res. Natl. Bur. Stand.* **57:** 217, 1956.

[116] MD. Sultan Mahmud, *Study of Structural and Magnetic Characteristics of Cr Substituted Fe-based Nanocrystalline Alloys.* PhD thesis, KUET, Khulna, Bangladesh, 2007.

[117] Joseph Goldstein *et. al.*, *Scanning Electron Microscopy and X-ray microanalysis*, Kluwer Academic/Plenum Publishers, New York, 2003.

[118] K. G. Efthimiadis, G. Stergioudis, S. C. Chadjivasiliou and I. A. Tsoukalas, *Cryst. Res. Technol.* **37:** 827, 2002.

[119] T. Kulik, *J. Non-Cryst. Solids* **287:** 145, 2001.

[120] K. G. Efthimiadis, C. A. Achilleos, S. C. Chadjivasiliou and I. A. Tsoukalas, *J. Magn. Magn. Mat.* **171:** 141, 1997.

[121] M. Matsmira, M. Sakurai, S. H. Kim, A. P. Tsai, A. Inoue and K. Suzuki, *Mater. Sci. Eng.: A* **217-218:** 397, 1996.

[122] T. Kulik, *Mater. Sci. Eng.: A* **159:** 95, 1992.

[123] T. H. Noh, M. B. Lee, H. J. Kim and I. K. Kang, *J. Appl. Phys.* **67:** 5568, 1990.

[124] W. T. Kim. P. W. Jang, S. C. Yu and B. S. Chun, *Mater. Sci. Eng.*: *A* **179-180:** 309, 1994.

[125] N. Pryds, M. Eldrup and A. Schrøder Pedersen, *Science of Metastable and Nanocrystalline Alloys: Structure, Properties and Modelling*, Proceedings of the 22nd Risø International Symposium on Materials Science, (3-7) September, 2001.

[126] A. R. Bhatti and B. Cantor, *J. Mater. Sci.* **29:** 816, 1994.

[127] F. E. Lubrosky, Editor, *Amorphous Metallic Alloys, Series:* Butterworths monographs in materials, London, UK, 1983.

[128] E. J. D. Garba and R. L. Jacobs, *J. Phys. F: Met. Phys.* **16:** 1485, 1986.

[129] M. A. Hakim and S. M. Hoque, *J. Magn. Magn. Mat.* **284:** 395, 2004.

[130] P. Goodhew, John Humphreys and Richard Beanland, *Electron Microscopy and Analysis*, Taylor & Francis, New York, 3rd Edition, 1988.

[131] A. E. Berkowitz, J. L. Walter and K. F. Wall, *Phys. Rev. Lett.* **46:** 1484, 1981.

[132] J. S. Blázquez, J. M. Borrego, C. F. Conde, A. Conde and J. M. Greneche, *J. Phys.: Condens. Matter* **15:** 3957, 2003.

[133] C. Gomez-Polo, J. I. Perez-Landazabal and V. Recarte , *IEEE Trans. Magn.* **39:** 3019, 2003.

[134] N. Q. Hoa, N. Chau, S. -C. Yu, T.M. Thang, N. D. The and N. D. Tho, *Mater. Sci. Eng.: A* **449–451:** 364, 2007.

[135] M. A. Hakim, S. Manjura Hoque, S. S. Sikder, Md. Sultan Mahmud and P. Nordblad, *J. Korean Phy. Soc.* **53:** 766, 2008.

[136] Md. Sultan Mahmud *Asian Trans. Sci. Technol.* **10:** 2221, 2011.

[137] H. Wei, Q. Bao, C. Wang, W. Zhang, Z. Yuan and X. Chen, *J. Non-Cryst. Solids* **354:** 1876, 2008.

[138] X. Y. Zhang, J. W. Zhang, F. R. Xiao, J. H. Liu, R. P. Liu, J. H. Zhao and Y. Z. Zheng, *Mater. Lett.* **34:** 85, 1998.

[139] S. J. Pickart and *R. Nathans, Phys. Rev.* **123:** 1163, 1961.

[140] E. Kisdi-Koszó and A. Lovas, *Key Eng. Mater.* **81-83:** 209, 1993.

[141] Philippe Toneguzzo, Guillaume Viau, Olivier Acher, Françoise Fiévet-Vincent and Fernand Fiévet, *Adv. Mater.* **10:** 1032, 1998.

[142] L. W. Deng, J. J. Jiang, S. C. Fan, Z. K. Feng, W. Y. Xie, X. C. Zhang and H. H. He, *J. Magn. Magn. Mat.* **264:** 50, 2003.

[143] S. Manjura Hoque, S. I. Liba, A. Anirban, Shamima Chowdhury and Shireen Akhter *AIP Advances* **6:** 25304, 2016.

[144] G. Rixecker, R. Birringer, A. Hartenberger, A. Himbert, A. Ries and H. Gleiter, *Nanostructured Materials* **6:** 629, 1995.

[145] M. Vázquez, C. Luna, M. P . Morales, R. Sanz, C. J. Serna and C. Mijangos, *Physica B: Condensed Matter* **354:** 71, 2004.

[146] C. Suryanarayana: *Prog. Mater. Sci*. **46:** 1, 2001.

[147] T. Yanai, M. Yamasaki, K. Takahashi, M. Nakano, Y. Yoshizawa and H. Fukunaga, *IEEE Trans.Magn.* **40:** 2721, 2004.

[148] X. Y. Zhang, J. W. Zhang, F. R. Xiao, J. H. Liu, K. Q. Zhang and Y. Z. Zheng, *J. Mater. Res.* **13:** 3241, 1998.